

PROCESS-CHAIN SIMULATION OF MANUFACTURING OF AEROSPACE  
BEARINGS

A THESIS SUBMITTED TO  
THE GRADUATE SCHOOL OF NATURAL AND APPLIED SCIENCES  
OF  
MIDDLE EAST TECHNICAL UNIVERSITY

BY  
ZEREN ÖZGENECİ

IN PARTIAL FULFILLMENT OF THE REQUIREMENTS  
FOR  
THE DEGREE OF DOCTOR OF PHILOSOPHY  
IN  
METALLURGICAL AND MATERIALS ENGINEERING

FEBRUARY 2025



Approval of the thesis:

**PROCESS-CHAIN SIMULATION OF MANUFACTURING OF  
AEROSPACE BEARINGS**

submitted by **ZEREN ÖZGENECİ** in partial fulfillment of the requirements for the degree of **Doctor of Philosophy in Metallurgical and Materials Engineering, Middle East Technical University** by,

Prof. Dr. Naci Emre Altun  
Dean, **Graduate School of Natural and Applied Sciences** \_\_\_\_\_

Prof. Dr. Ali Kalkanlı  
Head of Department, **Metallurgical and Materials Engineering** \_\_\_\_\_

Prof. Dr. C. Hakan Gür  
Supervisor, **Metallurgical and Materials Engineering, METU** \_\_\_\_\_

Assist. Prof. Dr. Ömer Music  
Co-Supervisor, **Engineering Dept., Cambridge University** \_\_\_\_\_

**Examining Committee Members:**

Prof. Dr. Arcan F. Dericioğlu  
Metallurgical and Materials Engineering, METU \_\_\_\_\_

Prof. Dr. C. Hakan Gür  
Metallurgical and Materials Engineering, METU \_\_\_\_\_

Prof. Dr. Cevdet Kaynak  
Metallurgical and Materials Engineering, METU \_\_\_\_\_

Prof. Dr. Nuri Durlu  
Mechanical Engineering, TOBB ETU \_\_\_\_\_

Assist. Prof. Dr. Şehram Dizeci  
Mechanical Engineering, TED University \_\_\_\_\_

Date: 04.02.2025

**I hereby declare that all information in this document has been obtained and presented in accordance with academic rules and ethical conduct. I also declare that, as required by these rules and conduct, I have fully cited and referenced all material and results that are not original to this work.**

Name Last name : Zeren Özgeneci

Signature :



## ABSTRACT

### PROCESS-CHAIN SIMULATION OF MANUFACTURING OF AEROSPACE BEARINGS

Özgeneci, Zeren

Doctor of Philosophy, Metallurgical and Materials Engineering

Supervisor: Prof. Dr. C. Hakan Gür

Co-Supervisor: Assist.Prof.Dr. Ömer Music

February 2025, 165 pages

The hot forging process is crucial in the manufacturing chain of aerospace bearings. Materials used in bearing production typically experience significant deformation during hot forging, which leads to damage evolution. This evolution can impact both the material and the process, ultimately affecting the final product's properties.

In this study, hot compression tests were performed on the Gleeble 3800 to accurately obtain the material behaviour of M50 steel. Afterward, hot tensile tests were performed through experiments and simulations using Forge NxT 3.2® software to determine the triggering value for the normalized Latham-Cockcroft ( $LC_n$ ) damage criterion. Subsequently, the metallurgical basis for the determined  $LC_n$  damage criterion was elucidated through detailed microstructural examinations, using optical microscopy and, primarily, scanning electron microscopy.

Finally, based on the calculated  $LC_n$  criterion value, a simulation of the multi-stage hot forging process, which includes upsetting, closed-die forging, and the shearing stage to separate the rings, was executed using Forge NxT 3.2®. This present study specifically focused on the third stage of the hot forging process: shearing, where

achieving a precise and smooth cut surface is essential. Initial simulations of the multi-stage hot forging process were conducted using various die clearances and forging start temperatures, followed by evaluations with different tool speeds. To assess the impact of die geometry on the shearing stage, radii and conical shapes at various angles were incorporated into the tool edges in contact with the die corners. Additionally, hot forging was performed experimentally in the field to corroborate the simulation results.

Keywords: M50 Steel, Hot Forging, Damage, Finite Element Method, Normalized Latham-Cockroft Criterion

## ÖZ

### HAVACILIK RULMANLARININ İMALAT ZİNCİRİNİN MODELLENMESİ

Özgeneci, Zeren  
Doktora, Metalurji ve Malzeme Mühendisliği  
Tez Yöneticisi: Prof. Dr. C. Hakan Gür  
Ortak Tez Yöneticisi: Dr. Öğr. Üyesi Ömer Music

Şubat 2025, 165 sayfa

Havacılık rulmanlarının imalat zincirinde, sıcak dövme prosesi son derece kritik bir rol oynamaktadır. Rulman imalatında kullanılan malzemeler, sıcak dövme prosesi sırasında hasar oluşumuna sebep olabilecek son derece yüksek deformasyonlara maruz kalırlar. Bu hasar oluşumu hem malzemeyi hem de prosesleri etkileyebileceği gibi nihai olarak da ürünün özelliklerini etkiler.

Bu çalışmada, M50 çeliğinin malzeme davranışını yüksek hassasiyette elde etmek için Gleeble 3800 kullanılarak sıcak basma testleri yapılmıştır. Takiben, normalize Latham-Cockcroft ( $LC_n$ ) hasar kriteri için tetikleme değerini belirlemek amacıyla, deneysel ve Forge NxT 3.2® yazılımı kullanılarak simülasyon yoluyla sıcak çekme testleri gerçekleştirilmiştir. Ardından, belirlenen  $LC_n$  hasar kriterinin metalurjik temeli, M50 çeliği mikroyapılarının taramalı elektron mikroskobu ve optik mikroskop ile detaylı inceleme çalışmaları ile açıklanmıştır.

Nihai olarak, hesaplanan  $LC_n$  hasar kriteri değerine dayanarak, çok istasyonlu sıcak dövme sürecinin (ezme, kapalı kalıp dövme, iç-dış bilezikleri ayırma olmak üzere kesme prosesi) simülasyonu Forge NxT 3.2® yazılımında gerçekleştirilmiştir. Bu çalışma, özellikle sıcak dövme sürecinin üçüncü aşamasına, hassas ve düzgün bir

kesim yüzeyi elde etmek esas olan bilezikleri ayıran kesme prosesine odaklanmıştır. Çok istasyonlu sıcak dövme sürecinin ilk simülasyon çalışmaları, çeşitli kalıp boşlukları ve dövme başlangıç sıcaklıkları kullanılarak yapılmış, ardından farklı pres hızları seçilerek, bu parametrelerin simülasyon sonucuna etkileri değerlendirilmiştir. Takım geometrisinin kesme prosesine etkisini değerlendirmek için, kalıp köşeleriyle temas eden takım kenarlarına çeşitli açılarda radyal ve konik şekiller eklenmiştir. Ayrıca, simülasyon sonuçlarını doğrulamak amacıyla sıcak dövme simülasyonları saha denemeleri ile gerçekleştirilmiştir.

Anahtar Kelimeler: M50 Çelik, Sıcak Dövme, Hasar, Sonlu Elemanlar Metodu, Normalize Latham-Cockroft Hasar Kriteri

To my driving forces; my precious family, husband and Minju

## ACKNOWLEDGMENTS

First and foremost, I would like to express my deepest respect and professional admiration to my first thesis advisor, Assoc. Prof. Dr. Caner Şimşir. I would have greatly valued the opportunity to present you with the printed version of this thesis.

I extend heartfelt thanks to my co-advisor, Assist. Prof. Dr. Ömer Music. Your guidance and support throughout this journey have been invaluable. I could not have reached this point without your help.

Additional important gratitude is owed to my most recent thesis advisor, Prof. Dr. C. Hakan Gür, whose guidance and motivation were pivotal in my decision to embark on my doctoral journey. I will always be grateful for your role in the whole process.

I am deeply grateful to my parents, Nurten and Cumhuriyet Taşkaya, Selma Özgeneci, as well as my sister, Zeynep Taşkaya, for their constant care, inspiration, understanding, love and guidance throughout my life. I also extend my gratitude to my beloved husband Erçin Özgeneci for his immense love and encouragement. My life would not have been possible without your unwavering support and patience.

I am grateful to my cherished friends, Burcu Şengül, Hande Adıgüzel, and Cansu Kahraman, for their continual support. Their joyful friendship and affection have been a true blessing throughout my life.

I offer my sincere thanks to my former managers, Dr.-Ing. Feridun Özhan, Dr.-Ing. Hamdullah Merdane, and current managers M. Turhan Savaş, Ozan Müştak, and Faik Karaaslan at ORS Bearings Inc. for their interest. I also extend my deepest thanks to my colleagues, Nazmi Saydemir and Ahmet Toros, as well as to all members of ORS Bearings Inc.

Additionally, I would like to acknowledge ORS Bearings Inc. for providing materials and conducting forging trials. This research was partially funded by the Scientific and Technological Research Council of Turkey under grant number 3190997.

## TABLE OF CONTENTS

ABSTRACT.....	v
ÖZ .....	vii
ACKNOWLEDGMENTS .....	x
TABLE OF CONTENTS.....	xi
LIST OF TABLES .....	xiii
LIST OF FIGURES .....	xv
LIST OF ABBREVIATIONS.....	xxi
LIST OF SYMBOLS .....	xxii
CHAPTERS	
1 INTRODUCTION .....	1
2 LITERATURE REVIEW .....	5
2.1 The Application of M50 Steel in Aerospace Bearings.....	5
2.1.1 M50 as Aerospace Bearing Steel .....	5
2.1.2 Utilization of M50 Steel in Bearing Manufacturing Processes .....	7
2.2 Process-Chain Simulation of Manufacturing .....	10
2.2.1 Material Data for Simulation .....	13
2.3 Summary and Conclusions.....	32
3 MATERIAL CHARACTERIZATION AND MODELLING MATERIAL BEHAVIOUR.....	33
3.1 Material Characterization w/ Computational Methods .....	34

3.2	Material Characterization w/ Experimental Methods .....	35
3.3	Modelling Material Behaviour.....	47
3.4	Parameter Identification for the Damage Criterion .....	50
3.4.1	Experimental Hot Tensile Tests .....	52
3.4.2	Numerical Hot Tensile Tests .....	58
3.5	Summary and Conclusions .....	64
4	MICROSTRUCTURE OBSERVATIONS OF M50 STEEL.....	67
4.1	Microstructure of As-Received M50 Steel .....	68
4.2	Microstructure After Hot Tensile Test Conditions .....	82
4.2.1	Fracture Morphology After Hot Tensile Testing.....	83
4.2.2	Subsurface Examination of Fractured Surfaces .....	103
4.3	Summary and Conclusion .....	122
5	FINITE ELEMENT ANALYSIS OF DAMAGE CHARACTERISTICS IN HOT FORGING PROCESS OF M50 BEARING RINGS .....	125
5.1	Simulation of Hot Forging of Bearing Rings.....	125
5.1.1	Modelling and Simulation of Upsetting, Forming and Shearing Processes.....	126
5.1.2	Shearing Length Determination .....	129
5.2	Summary and Conclusion .....	145
6	CONCLUSIONS .....	147
	REFERENCES .....	151
	CURRICULUM VITAE .....	165



## LIST OF TABLES

### TABLES

Table 2.1 Chemical Compositions of Bearing Steels (Wt%) [5].....	6
Table 2.2 Critical Damage Function at Different Thermomechanical Conditions [62].....	24
Table 3.1 Chemical Analysis (Wt%) [Carpenter Technology, USAS, M50 VIMVAR, Diameter: 45.00 mm].....	33
Table 3.2 R <sup>2</sup> values from the curve-fitting procedures .....	47
Table 3.3 Parameters of the Hänsel-Spittel Equation .....	48
Table 3.4 Measurements of Hot Tensile Test Samples' Diameters.....	56
Table 4.1 Chemical Composition of the Spectrums Analyzed in Figure 4.5.....	72
Table 4.2 Chemical Composition of the Spectrums Analyzed in Figure 4.8.....	75
Table 4.3 Chemical Composition of the Spectrums Analyzed in Figure 4.10.....	76
Table 4.4 Chemical Composition of the Spectrums Analyzed in Figure 4.12.....	78
Table 4.5 Chemical Composition of the Spectrums Analyzed in Figure 4.14.....	80
Table 4.6 Chemical Composition of the Spectrums Analyzed in Figure 4.16.....	81
Table 4.7 Chemical Composition of the Spectrums Analyzed in Figure 4.34.....	96
Table 4.8 Chemical Composition of the Spectrums Analyzed in Figure 4.29.....	97
Table 4.9 Chemical Composition of the Spectrums Analyzed in Figure 4.30.....	98
Table 4.10 Chemical Composition of the Spectrums Analyzed in Figure 4.31 .....	99
Table 4.11 Chemical Composition of the Spectrums Analyzed in Figure 4.32 ...	100
Table 4.12 Microhardness Measurements from Hot Tensile Tests Samples.....	116
Table 4.13 XRD Measurement Parameters .....	118
Table 4.14 Retained Austenite (%) vs Hot Tensile Test Temperatures (°C).....	119
Table 4.15 Phase Fractions (%) of the Sub-surfaces from Hot Tensile Tests .....	121
Table 5.1 Calculated Shearing Length at Various Forging Temperatures and Clearances .....	137
Table 5.2 Shearing Length Comparison: Simulation vs. Experimental Results...	142
Table 5.3 Effect of Press Speed on Shearing Length (Upper Die) .....	143

Table 5.4 Effect of Die Radius Changes on Shearing Length.....	143
Table 5.5 Effect of Conically Shaped Upper Die on Shearing Length .....	144

## LIST OF FIGURES

### FIGURES

Figure 1.1. Assembly of bearing rings with auxiliary components .....	2
Figure 2.1. Key segments of a turbine (jet) engine [4] .....	6
Figure 2.2. Bearing outer ring forging process (a) with straight punching pin (b) with V-shaped punching pin [11].....	8
Figure 2.3. Flow line development of forging process with straight punching pin a) initial flow lines, b) after upsetting, c) after punching d) after punching the recess [11].....	8
Figure 2.4. Flow line development of forging process with V-shaped punching pin a) initial flow lines, b) after upsetting, c) after punching, d) after punching the recess e) after expansion [11] .....	9
Figure 2.5. Flow line distribution within the bearing's outer ring. (a) Outcome of FEM simulation and (b) Forging result [11].....	10
Figure 2.6. Process-chain of manufacturing of an aero-engine disc [12] .....	12
Figure 2.7. Flow curves at strain rate of (a) $0.25\text{s}^{-1}$ and (b) $2\text{s}^{-1}$ [45].....	17
Figure 2.8. The temperature distribution chart at (a) $0.25\text{s}^{-1}$ (b) $2\text{s}^{-1}$ [45] .....	17
Figure 2.9. Comparing experimental flow stress with predicted values using the Hänsel–Spittel model at $\epsilon=0.01\text{ s}^{-1}$ , $0.1\text{ s}^{-1}$ , $1\text{ s}^{-1}$ , $10\text{ s}^{-1}$ [53] .....	19
Figure 2.10. Folding defects at the intersection of the convex key and the side wall [53].....	20
Figure 2.11. Folding defects at the inner flash [53].....	20
Figure 2.12. Development of failure (macro-crack) [57].....	22
Figure 2.13. Connection between the reference stress and deformation energy [64] .....	25
Figure 2.14. Fracture lines prediction with the Latham-Cockcroft criterion and experimentally (Shaded Region) [66].....	27
Figure 2.15. Latham-Cockcroft criterion predictions for internal damage and central burst in DEFORM [68] .....	28

Figure 2.16. Distribution of the Latham-Cockroft damage criterion: cross-sectional analysis with notable measurement points [69].....	29
Figure 2.17. Workpiece damage occurs in third operation [71].....	30
Figure 2.18. Fracture initiation sites: (a) predicted by FEA (b) experimentally observed in the forging experiment [72] .....	31
Figure 3.1. Compression test specimens of M50 for the Gleeble 3800 .....	36
Figure 3.2. (a) Initial cylinder size before compression (b) Final cylinder size after compression; (c) Impact of barreling on stress-strain curve [78].....	38
Figure 3.3. Correlation between the square root of the barreling coefficient ( $B^{1/2}$ ) and the friction coefficient ( $\mu$ ) for various specimen diameter/height ratios [80] ..	40
Figure 3.4. Uncorrected and corrected flow curves at 1000°C, 1050°C, 1100°C, and 1150°C with a 0.1 s <sup>-1</sup> strain rate .....	41
Figure 3.5. Uncorrected and corrected flow curves at 1000°C, 1050°C, 1100°C, and 1150°C with a 1 s <sup>-1</sup> strain rate .....	42
Figure 3.6. Uncorrected and corrected flow curves at 1000°C, 1050°C, 1100°C, and 1150°C with a 10 s <sup>-1</sup> strain rate .....	42
Figure 3.7. T= 1000°C, 1050°C, 1100°C, 1150°C ( $\dot{\epsilon}=0.1$ s <sup>-1</sup> ) .....	44
Figure 3.8. T= 1000°C, 1050°C, 1100°C, 1150°C ( $\dot{\epsilon}=1$ s <sup>-1</sup> ) .....	45
Figure 3.9. T= 1000°C, 1050°C, 1100°C, 1150°C ( $\dot{\epsilon}=10$ s <sup>-1</sup> ) .....	46
Figure 3.10. Corrected and HS calculated flow curves at 0.1 s <sup>-1</sup> .....	49
Figure 3.11. Corrected and HS calculated flow curves at 1 s <sup>-1</sup> .....	49
Figure 3.12. Corrected and HS calculated flow curves at 10 s <sup>-1</sup> .....	50
Figure 3.13. Tensile test specimens of M50 for the Gleeble 3800.....	52
Figure 3.14. Hot tensile tests in Gleeble system .....	54
Figure 3.15. The experimental engineering stress-strain curve at 1050°C.....	55
Figure 3.16. The experimental engineering stress-strain curve at 1100°C.....	55
Figure 3.17. The experimental engineering stress-strain curve at 1150°C.....	56
Figure 3.18. Reduction of area (%) vs temperature (°C).....	57
Figure 3.19. Fracture strain (%) vs temperature (°C).....	57
Figure 3.20. Velocity-time curves (a-b-c) of tensile tests .....	59

Figure 3.21. Gauge length modeling for the 2D test simulations in Forge NxT 3.2®	60
.....	
Figure 3.22. FEM results of the tensile tests at 1050°C with $LC_n=2, 5$ and 10.....	62
Figure 3.23. Comparison of experimental and calculated flow stresses at 1050°C	63
Figure 3.24. Comparison of experimental and calculated flow stresses at 1100°C	63
Figure 3.25. Comparison of experimental and calculated flow stresses at 1150°C	64
Figure 4.1. Microstructural analysis of the examined sections.....	68
Figure 4.2. OM images of M50 from (a) the surface and (b) cross-section .....	69
Figure 4.3. Regions analyzed by SEM in the cross-section.....	70
Figure 4.4. Center mapping with SEM at 200X magnification .....	70
Figure 4.5. Center mapping with SEM at 500X magnification .....	71
Figure 4.6. EDS analysis results of center mapping with SEM at 500X .....	72
Figure 4.7. Mapping of the cross-section with SEM at 500X magnification .....	73
Figure 4.8. SEM images of the M50 steel matrix and primary carbides at 10.000X magnification from the center of the cross-section (a) Back Scattered Electron (BSE) (b) Secondary Electron (SE) imaging modes of SEM .....	74
Figure 4.9. EDS analysis results of center with SEM at 10.000X .....	74
Figure 4.10. SEM images of the M50 steel matrix and primary carbides at 10.000X magnification from the mid-radius of the cross-section (a) Back Scattered Electron (BSE) (b) Secondary Electron (SE) imaging modes of SEM .....	75
Figure 4.11. EDS analysis results of mid-radius with SEM at 10.000X .....	76
Figure 4.12. SEM images of the M50 steel matrix and primary carbides at 10.000X magnification from the surface of the cross-section (a) Back Scattered Electron (BSE) (b) Secondary Electron (SE) imaging modes of SEM .....	77
Figure 4.13. EDS analysis results of surface with SEM at 10.000X .....	77
Figure 4.14. Surface mapping with SEM at 500X magnification.....	79
Figure 4.15. EDS analysis results of the surface mapping with SEM at 500X .....	79
Figure 4.16. SEM images of the M50 steel matrix and primary carbides at 10.000X magnification from the surface (a) Back Scattered Electron (BSE) (b) Secondary Electron (SE) imaging modes of SEM.....	80

Figure 4.17. EDS analysis results of surface with SEM at 10.000X.....	81
Figure 4.18. Specimens after hot tensile tests at various temperatures .....	84
Figure 4.19. Fracture surfaces under SM after hot tensile tests .....	85
Figure 4.20. Fracture morphology under SEM after hot tensile test at 1050°C .....	86
Figure 4.21. Fracture morphology under SEM after hot tensile test at 1100°C .....	87
Figure 4.22. Fracture morphology under SEM after hot tensile test at 1125°C .....	88
Figure 4.23. Fracture morphology under SEM after hot tensile test at 1138°C .....	89
Figure 4.24. Fracture morphology under SEM after hot tensile test at 1150°C .....	90
Figure 4.25. Fracture morphology under SEM after hot tensile test at 1163°C .....	91
Figure 4.26. Fracture morphology under SEM after hot tensile test at 1175°C .....	92
Figure 4.27. SEM examination of Figure 4.26 at higher magnification.....	95
Figure 4.28. EDS spectra for subsurface (region 1) of the 1175°C sample (a) Back Scattered Electron (BSE) (b) Secondary Electron (SE) imaging modes of SEM ...	96
Figure 4.29. EDS spectra for subsurface (region 2) of the 1175°C sample (a) Back Scattered Electron (BSE) (b) Secondary Electron (SE) imaging modes of SEM ...	97
Figure 4.30. EDS spectra for subsurface (region 3) of the 1175°C sample (a) Back Scattered Electron (BSE) (b) Secondary Electron (SE) imaging modes of SEM ...	98
Figure 4.31. EDS spectra for subsurface (region 4) of the 1175°C sample (a) Back Scattered Electron (BSE) (b) Secondary Electron (SE) imaging modes of SEM ...	99
Figure 4.32. EDS spectra for subsurface (region 5) of the 1175°C sample (a) Back Scattered Electron (BSE) (b) Secondary Electron (SE) imaging modes of SEM .	100
Figure 4.33. Dimple on the fracture surface after tensile test at 1125°C .....	101
Figure 4.34. Dimple on the fracture surface after tensile test at 1150°C .....	102
Figure 4.35. Subsurface of the fracture surface after hot tensile test at 1050°C ...	104
Figure 4.36. Subsurface of the fracture surface after hot tensile test at 1100°C ...	104
Figure 4.37. Subsurface of the fracture surface after hot tensile test at 1125°C ...	105
Figure 4.38. Subsurface of the fracture surface after hot tensile test at 1138°C ...	105
Figure 4.39. Subsurface of the fracture surface after hot tensile test at 1150°C ...	106
Figure 4.40. Subsurface of the fracture surface after hot tensile test at 1163°C ...	106
Figure 4.41. Subsurface of the fracture surface after hot tensile test at 1175°C ...	107

Figure 4.42. EBSD images (a) Layered, b) Band Contrast (BC), c) Recrystallized Fraction and d) Grain Boundary (GB) of the map data) for specimen under deformed at 1125°C / 10s <sup>-1</sup> .....	108
Figure 4.43. EBSD images (a) Layered, b) Band Contrast (BC), c) Recrystallized Fraction and d) Grain Boundary (GB) of the map data) for specimen under deformed at 1150°C / 10s <sup>-1</sup> .....	109
Figure 4.44. EBSD images (a) Layered, b) Band Contrast (BC), c) Recrystallized Fraction and d) Grain Boundary (GB) of the map data) for specimen under deformed at 1163°C / 10s <sup>-1</sup> .....	110
Figure 4.45. EBSD images (a) Layered, b) Band Contrast (BC), c) Recrystallized Fraction and d) Grain Boundary (GB) of the map data) for specimen under deformed at 1175°C / 10s <sup>-1</sup> .....	111
Figure 4.46. LAGB (%) vs hot tensile test temperatures (°C).....	112
Figure 4.47. HAGB (%) vs hot tensile test temperatures (°C).....	112
Figure 4.48. SB (%) vs hot tensile test temperatures (°C).....	113
Figure 4.49. Average grain size (µm) vs hot tensile test temperatures (°C).....	115
Figure 4.50. Hardness measurement (HV1) from subsurfaces .....	116
Figure 4.51. X-Ray Diffractometer (XRD) (1) goniometer, (2) x-ray generator tube and (3) position sensitive detector .....	117
Figure 4.52. EBSD analyses of microstructures after hot tensile tests (left) BC image (right) phase map.....	120
Figure 4.53. Retained austenite (%) amounts measured by XRD and EBSD .....	121
Figure 4.54. Illustration of the equi-cohesive temperature (T <sub>E</sub> ) [95].....	123
Figure 5.1. (a) Initial M50 billet at the end of (b) upsetting (c) forming processes .....	127
Figure 5.2. The considered thermal contact between billet with upper/lower dies .....	128
Figure 5.3. The considered thermal contact with ambient medium.....	128
Figure 5.4. Creation of shearing area using remeshing box with 0.1 mm elements .....	130

Figure 5.5. Primary billet shape for shearing process in hot forging simulation ..	130
Figure 5.6. Tracking $LC_n$ and temperature for shearing length determination.....	131
Figure 5.7. Shear Length Evaluation at $T_{\text{ForgingStart}} = 1100^\circ\text{C}$ with $LC_n$ .....	133
Figure 5.8. Shear Length Evaluation at $T_{\text{ForgingStart}} = 1150^\circ\text{C}$ with $LC_n$ .....	134
Figure 5.9. Shear Length Evaluation at $T_{\text{ForgingStart}} = 1175^\circ\text{C}$ with $LC_n$ .....	135
Figure 5.10. Shear Length Evaluation at $T_{\text{ForgingStart}} = 1200^\circ\text{C}$ with $LC_n$ .....	136
Figure 5.11. Hot forging press at ORS with 4 stations.....	138
Figure 5.12. Inner and outer rings after hot forging experiments at ORS with 0.4 mm die clearance .....	139
Figure 5.13. SM analysis of separation surface (1) and the shearing length (2) under SM (at $1100^\circ\text{C}$ ).....	140
Figure 5.14. SM analysis of separation surface and the shearing length (at $1150^\circ\text{C}$ ) .....	140
Figure 5.15. SM analysis of separation surface and the shearing length (at $1200^\circ\text{C}$ ) .....	141
Figure 5.16. Examination of separation surfaces on 100Cr6 and M50 rings: (a)separation surface on ring, (b)shearing length .....	141
Figure 5.17. The upper die designed with an $8^\circ$ conical angle.....	144



## LIST OF ABBREVIATIONS

### ABBREVIATIONS

BCC	Body-Centered Cubic
BSE	Back Scattered Electron
CPS	Count per seconds
DRV	Dynamic Recovery
DRX	Dynamic Recrystallization
EBS	Electron Backscatter Diffraction
EDS	Energy Dispersive Spectroscopy
FCC	Face-Centered Cubic
FE	Finite Element
FEA	Finite Element Analysis
FEM	Finite Element Method
FM	Fracture Mechanics
HRC	Hardness of Rockwell C
HS	Hänsel–Spittel
LC <sub>n</sub>	Normalized Latham-Cockroft
MDM	Micro-Scale Damage Mechanics
mm	milimeter
OM	Optical Microscope
rpm	Revolutions per minute
SE	Secondary Electron
SEM	Scanning Electron Microscope
SM	Stereo Microscope
wt (%)	weight (%)
XRD	X-Ray Diffractometer

## LIST OF SYMBOLS

### SYMBOLS

C	Critical Threshold of Damage Criterion
$\bar{\epsilon}_f$	Fracture Limit of Equivalent Strain
$\dot{\epsilon}$	Strain Rate
$\bar{\epsilon}$	Equivalent Strain
$\sigma_{\max}$	Maximum Principal Stress
$\bar{\sigma}$	Equivalent Stress
$\sigma_a$	Stress Measured from Axial Extensometer
$\sigma_{fc}$	Stress After Friction Correction
$\mu$	Friction Coefficient
t	Time
d	Diameter
h	Height
c	Friction Constant
B	Barrelling Coefficient
W	Plastic Deformation Energy
T	Temperature
$T_E$	Equi-Cohesive Temperature
$\Delta T$	Temperature Gradient
$R^2$	Coefficient of Determination
e	Natural Constant
A	Material Constant
$m_1- m_9$	Material Constants (sensitivity to temperature, strain and strain rate)

## **CHAPTER 1**

### **INTRODUCTION**

One of the initial alloys engineered for commercial bearing applications was 52100 (100Cr6) steel, which primarily consists of 1% carbon and 1.5% chromium. Although minor enhancements in the performance of 52100 were made through additional alloying elements, these incremental improvements were insufficient to meet the demands of higher operating temperatures in advanced applications. Consequently, M50 steel, which contains chromium, vanadium, and molybdenum, has been selected for bearing applications operating at moderately higher temperatures in the aerospace industry since the 1950s.

Generally, bearing steel is supplied as bars in a raw material form. The conventional method for using steel bars in the manufacturing of bearings involves initially shaping the inner and outer bearing rings through a hot forging process. Following this, the typical process flow for bearing production includes spheroidization heat treatment and machining processes such as cold ring rolling and turning. Subsequently, the through-hardening heat treatment is carried out, where hardness and final microstructure are accurately determined. After the heat treatment, the final form of the inner and outer rings with precise tolerances is achieved through grinding. Finally, the ground rings are assembled with auxiliary bearing components such as balls, cages, and covers. Figure 1.1 illustrates a schematic representation of the ball bearing assembly process.



Figure 1.1. Assembly of bearing rings with auxiliary components

Since the hot forging process is the starting point of this manufacturing chain, it plays a critical role in bearing production. During hot forging process, the materials used in bearing production typically undergo substantial deformation, which can lead to damage progress. Consequently, this damage evolution can impact both the material and the process, ultimately affecting the characteristics of the finished product.

The outstanding characteristics of M50 arise from its alloying elements and carbides. However, this composition restricts its hot working conditions, permitting hot forging only within a defined range. Consequently, it is crucial to accurately represent and incorporate damage in finite element simulations when designing and implementing the process for M50 steel. This study focuses on investigating the progression of damage during the multi-stage hot forging of M50 steel bearing rings.

The thesis starts with an extensive review of literature on research studies that provide valuable insights into the finite element analysis of damage characteristics during the hot forging process of M50 steel. In Chapter 3, a comprehensive dataset was developed to accurately capture the behaviour of M50 material, and corresponding flow curves were established. Subsequently, experiments and

simulations using Forge NxT 3.2® software were conducted to determine the triggering value for the normalized Latham-Cockcroft ( $LC_n$ ) damage criterion. Chapter 4 investigates the metallurgical factors influencing the thermal deformation behaviour of M50 steel. Finally, Chapter 5 explores the evolution of damage during the multi-stage hot forging of M50 steel bearing rings through a combination of experimental, physical, and numerical approaches.

This study examines the progression of damage during the multi-stage hot forging of M50 steel bearing rings and addresses a notable gap in the literature. It offers new insights into the finite element analysis of damage characteristics specific to M50 steel during hot forging. Although recent decades have seen an increase in both mechanical and numerical studies, there is still a substantial lack of research on simulating the complete manufacturing chain for aerospace bearings, especially regarding the hot forging process. The specific issue of damage evolution during multi-stage hot forging of M50 steel remains unexplored in existing studies. This research aims to bridge this gap, which is crucial for improving the understanding of M50 bearing production and ensuring their reliability and performance in various applications.



## **CHAPTER 2**

### **LITERATURE REVIEW**

#### **2.1 The Application of M50 Steel in Aerospace Bearings**

Steel employed in aerospace or challenging environments exhibit a distinctive characteristic: they retain their hardness even when subjected to temperatures ranging from 120°C to 320°C. Additionally, their strength at elevated temperatures can prove beneficial in situations where lubrication fails or becomes inadequate, temporarily preserving the integrity of bearings. Hardness levels lower than 58 HRC are unfavorable since typical steels experience the formation of grooves on the raceways. The most favorable performance at elevated temperatures was achieved by modifying highly-alloyed tool steels like M50 [1].

##### **2.1.1 M50 as Aerospace Bearing Steel**

Advanced gas turbine engines demand high-performance mechanical systems (such as bearings and gears) that must function at continuously rising operational speeds, temperatures, and loads [2]. For turbine engine main shafts, the material of the bearings must exhibit attributes like long life, dimensional stability, high strength, and exceptional wear resistance, particularly under high-temperature conditions. Therefore, the alloys used in bearings include elements like molybdenum, vanadium and tungsten, which help them retain their hardness even at elevated temperatures for applications above 177°C [3]. Figure 2.1 shows a diagram of a turbine (jet) engine.

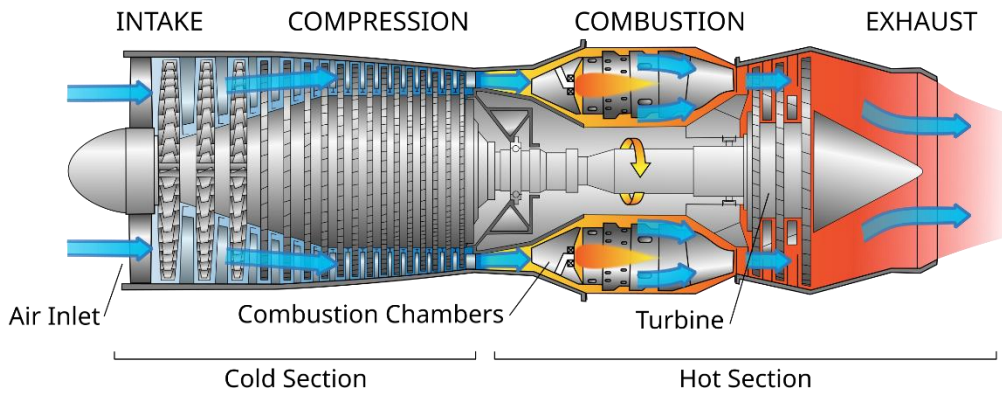


Figure 2.1. Key segments of a turbine (jet) engine [4]

AISI 52100 steel is widely used for bearings because its high carbon content enhances hardness. However, it is deficient in certain alloying elements that are crucial for corrosion resistance, carburization enhancement, and carbide formation control. In contrast, M50 is a commonly used through-hardened steel that includes additional alloying elements, leading to improved mechanical properties compared to 52100, such as the formation of precipitated carbides for bearings [4]. For this reason, M50 is utilized by the major jet engine manufacturers for rolling-element bearings [3]. Approximate chemical composition in wt% of bearing steels is presented in Table 2.1.

Table 2.1 Chemical Compositions of Bearing Steels (Wt%) [5]

	<b>C</b>	<b>Si</b>	<b>Cr</b>	<b>Mo</b>	<b>V</b>	<b>Mn</b>
<b>M50</b>	0.83	0.25	4.1	4.25	1.00	0.2
<b>AISI 52100</b>	1.0	0.2	1.45			0.35



### **2.1.2 Utilization of M50 Steel in Bearing Manufacturing Processes**

M50 is a type of secondary-hardening steel. It undergoes a quenching process to form martensite, followed by tempering at 540–550°C. This tempering phase causes an alloy carbide mixture abundant in molybdenum, chromium and vanadium to precipitate [5]. The material consists of a martensite matrix with grain sizes ranging from 10 to 15 microns. M50 contains both significant primary carbides (5-10 microns) and smaller carbides (<5 microns), which are evenly dispersed throughout the material, comprising about 12 vol% overall [6-7]. The formation of the larger carbides occurs during the casting stage, facilitated by the high initial carbon content. As the rolling/forging processes take place, these large carbides tend to align and arrange themselves in bands. The smaller, secondary carbides are generated through tempering and exhibit random orientations [4].

M50 steel's exceptional properties come from the alloying elements and carbides in it, which cause secondary hardening but limit its ability for hot-working [8]. Therefore, M50 bearing steel usually shows reduced ability to deform, but this is primarily observed within a limited range during hot working processes [9].

Bearing rings are commonly produced by the forging process since it can rectify specific defects that arise from the raw materials. In this concept, the formation of flow lines that occurs in the forging of bearing rings was studied by Jiang et al [11]. The process of flowline development was simulated using DEFORM 3D-11.0 Finite Element Method (FEM) software, employing models that represent rigid-plastic material behavior. In this study, two distinct hot forging methods were used. As shown in Figure 2.2, Figure 2.3 and Figure 2.4, simulation was conducted on the shaping procedure of the outer bearing ring. This analysis aimed to understand the shaping mechanism and the progression of flow lines.

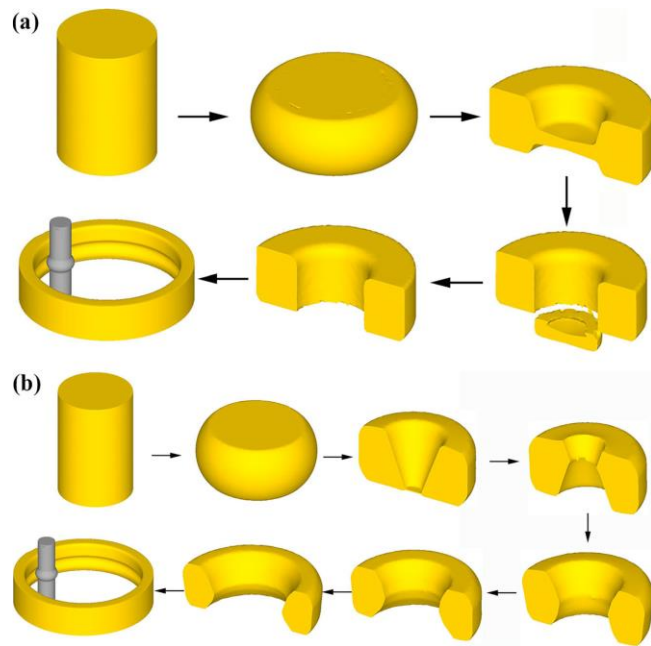


Figure 2.2. Bearing outer ring forging process (a) with straight punching pin (b) with V-shaped punching pin [11]

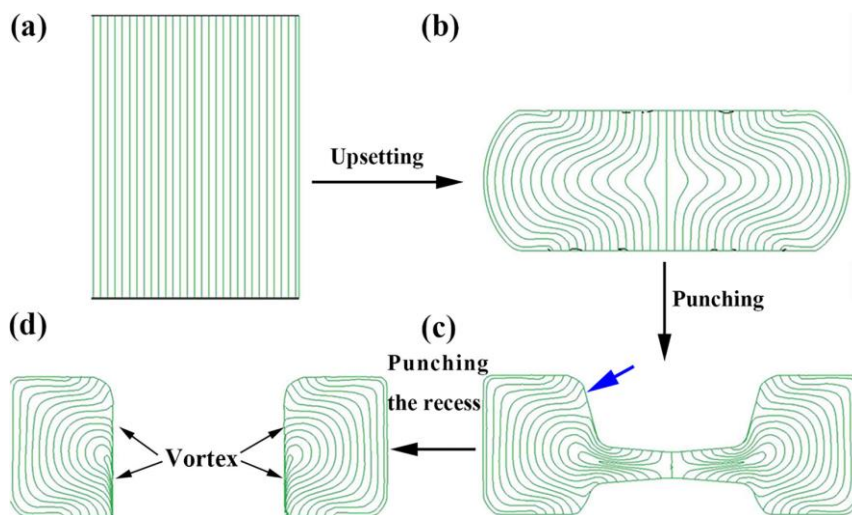


Figure 2.3. Flow line development of forging process with straight punching pin a) initial flow lines, b) after upsetting, c) after punching d) after punching the recess [11]

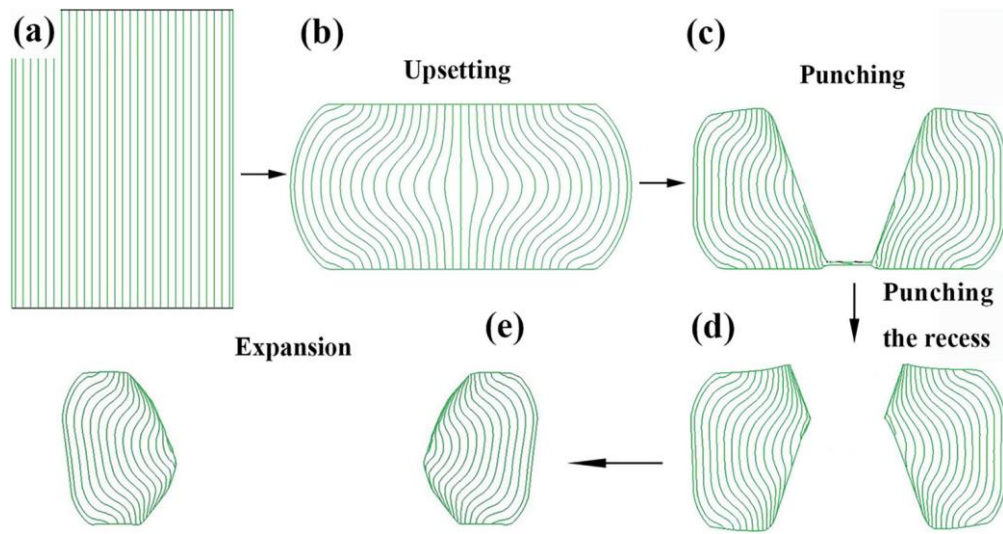


Figure 2.4. Flow line development of forging process with V-shaped punching pin  
 a) initial flow lines, b) after upsetting, c) after punching, d) after punching the  
 recess e) after expansion [11]

Analysis of both simulations and experimental results highlighted the significant influence of the punch die and its placement on flow-line formation. Introducing a V-shaped punching pin and situating the punch recess at the billet's base effectively reduced flow-line inconsistencies arising from the punching process. Consequently, a bearing outer ring exhibiting a favorable flow-line distribution was successfully achieved [11]. The arrangement of flow lines in the outer ring of the bearing is depicted in Figure 2.5, following both FEM simulation and the forging process.

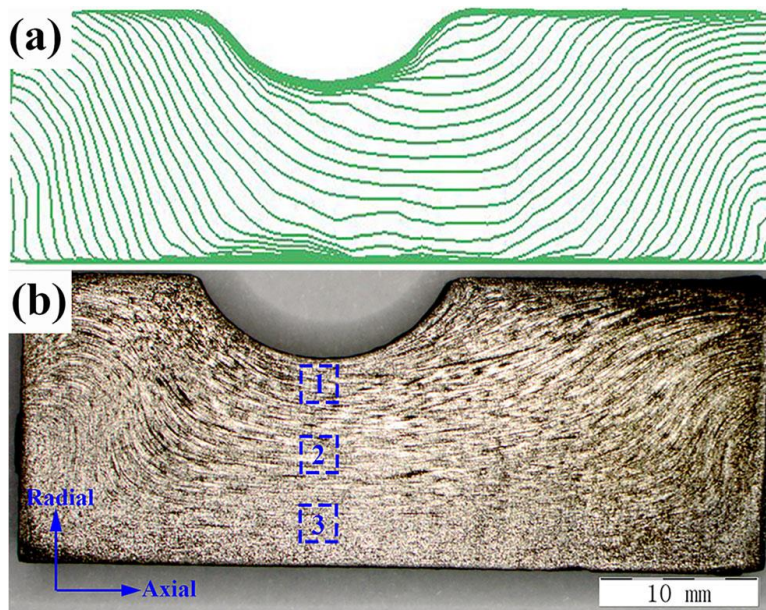


Figure 2.5. Flow line distribution within the bearing's outer ring. (a) Outcome of FEM simulation and (b) Forging result [11]

## 2.2 Process-Chain Simulation of Manufacturing

Tracking the metal composition and the evolution of microstructure throughout the entire manufacturing process-chain is now essential in the metal forming industry. This is essential for gaining a deeper insight into the processes and meeting the rising quality demands for parts. For these reasons, creating a simulation tool capable of modeling the entire chain becomes crucial. While we now have an improved understanding of the physical processes occurring during the manufacturing, there are still significant numerical challenges to overcome in running accurate simulations [10].

The production of final parts according to specific criteria typically involves a variety of technologies and interconnected processes within manufacturing chains. In industries like aerospace, automotive, energy, and medicine, among others, most components are created through a sequence of manufacturing steps. Each part has predefined specifications that need to be met. These specifications can involve

factors like complex shapes, size, precise measurements, surface quality, durability, cost, production time. The manufacturing process chains need to be developed and optimized to ensure the final parts fulfill these requirements. Reducing defects during manufacturing and extending the lifespan of components are crucial goals, particularly in the aerospace sector. Defects introduced during the manufacturing processes can lead to decreased longevity of the components throughout their lifespan [12].

So, this section provides an overview of contemporary trends and achievements in modeling, simulations, and the implementation of manufacturing process chains by discussing various approaches and practices.

Afazov [12] effectively completed the simulation of three manufacturing process chains. These chains encompassed a parallelepiped structural aero-engine disc (Figure 2.6) and an aero-engine vane. This was achieved through the application of FE Data and FE Data Exchange System, which was utilized to showcase the feasibility of simulating manufacturing process chains.

Heusinger and colleagues [13] employed STEP-NC programme for the comprehensive integration of CAx chains, spanning from design to machining. Monostori et al. [14] presented an alternative method involving machine learning and search techniques for the optimization of cutting processes.

Hyun and Lindgren [15] engaged in the simulation of a manufacturing process sequence using FEA, encompassing stainless steel SS316L's forging, heat treatment, and cutting. Additionally, Pietrzyk et al. [16] employed the Finite Element (FE) method to model and enhance the process chains for multi-stage forging of carbon steel.

Klein and Eifler [17] examined how different steps in manufacturing chains, along with variations in microstructure, affect the final mechanical properties. They created test samples using five process chains that involved heat treatment, turning, and grinding. Their findings revealed that the machining procedures and their associated

parameters have a direct impact on the condition of the near surface region, subsequently influencing fatigue life. The nature of the process and its specific parameters contribute to diverse transformations in microstructure, along with varying magnitudes and type of residual stresses.

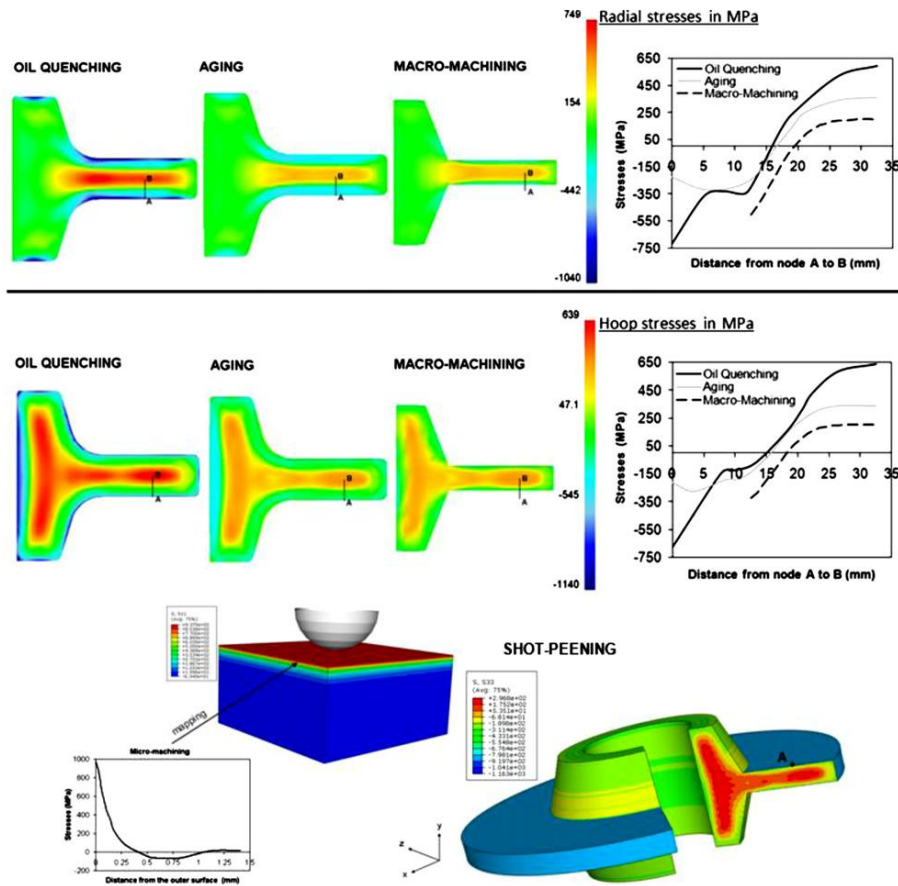


Figure 2.6. Process-chain of manufacturing of an aero-engine disc [12]

When simulations are frequently employed to ascertain process parameters for achieving desired properties in the resulting product, it becomes crucial to incorporate the complete manufacturing process flow in these simulations. To facilitate the simulation of a manufacturing process sequence, it is necessary to

transfer engineering data between the simulations of each individual process. Using an integrated simulation method that models all the manufacturing steps within a production sequence allows us to optimize process parameters for all operations, not just a single one. Modifying a parameter in an early-stage process can have ripple effects on later stages. To effectively optimize the impact of this parameter on the final product, it's crucial to simulate the complete manufacturing process flow [18].

Choosing process parameters is a challenging task that relies on prior knowledge and experience with the specific process. While simulations can assist in evaluating these parameters, they provide valuable support in the process parameter decision-making [19].

The system's required information was identified through collaboration with simulation software users in various processes. This information included components like nodes, elements, stress, strain, temperature, plastic strain, boundary conditions, along with material data and process parameters. During the initial system development phase, material data and process parameters were intentionally omitted, and only the essential information for simulating the cutting process was integrated. Nevertheless, it is evident that material data and process parameters are vital components of any simulation and must be incorporated into the finalized system. The data required for modeling the welding process of the spool design includes process parameters, boundary conditions, result sets, material data, and geometric information. After completing this simulation, the results are archived, and the necessary data for subsequent simulations is retrieved from the system along with an appropriate subroutine file tailored for each specific simulation [20].

### **2.2.1 Material Data for Simulation**

In most cases, bearing steel is typically supplied in the form of bars or tubes as its raw material. When it comes to using as-spheroidized seamless steel tubes, the initial step in production involves a turning operation. Conversely, steel bars are employed

in two different manners. In the first approach to using steel bars, the process begins with drilling operations on the steel bars, followed by a turning operation to create the initial shape of the bearing rings. In the second and more traditional method of using steel bars, inner and outer bearing rings are initially shaped through a hot forging operation [21].

As it is mentioned in the previous paragraph, since the most conventional starting point is the hot forging process, this thesis will focus on simulating the hot forging process. Within this scope, a literature review was also conducted regarding hot deformation behaviour of alloys.

### **2.2.1.1 Hot Workability of Alloys**

Evaluating a material's capacity for plastic deformation, known as hot workability, is a crucial factor in determining its ability to withstand deformation without developing cracks and achieving the desired mechanical properties and microstructure under specific conditions of temperature and strain rate. This assessment typically involves the analysis of several parameters, including strain rate, strain, and temperature. Hot forging is typically carried out at extremely elevated temperatures, around 75% of the melting point. This step aims to eliminate both the macrosegregation and the microstructural inconsistencies [22].

The flow behavior observed in a hot forging process is defined by a combination of strain hardening and softening resulting from dynamic phenomena such as recrystallization and recovery. These processes are pivotal in shaping the ultimate quality of the forged product. To understand and represent the plastic deformation characteristics of metals and alloys during forging, researchers frequently employ constitutive relations. Numerous research teams have made efforts to construct these constitutive equations, employing a range of models to capture the flow characteristics of different alloys through the analysis of experimental data [23-26].



To investigate the workability of specific metals/alloys and identify the optimal parameters for hot forming, various research groups have conducted thermo-mechanical studies. These studies involve compressive, tensile and torsion experiments which were conducted over a wide range of forming temperatures and strain rates. As a result, researchers developed several mathematical equations, known as constitutive equations, to describe how these materials behave when subjected to hot deformation. Constitutive equations are frequently employed to characterize the plastic deformation characteristics of metals and alloys in a manner suitable for incorporation into computer programs, enabling the modeling of how mechanical components respond to forging processes under specific loading conditions. The precision of numerical simulations relies on the establishment of a suitable constitutive model. Numerous constitutive equations have been introduced to forecast the flow stress of metals and alloys under high-temperature conditions. These equations can be broadly categorized into three groups: empirical, phenomenological, and physical [27].

Phenomenological models provide a flow stress definition derived from empirical observations and incorporates mathematical functions. Furthermore, phenomenological constitutive models involve fewer material constants and can be conveniently adjusted through calibration. So, phenomenological plastic constitutive models are extensively employed in metals and alloys' forming simulations at elevated strain rates and temperatures [27].

Phenomenological constitutive models share a common characteristic: they are formulated in terms of the forming temperature ( $T$ ), strain rate ( $\dot{\epsilon}$ ) and strain. This allows them to account for how these parameters influence the flow behaviour of metals and alloys [27].

Concerning warm and hot forming processes, the precise constitutive equation can be employed within FE numerical simulations to enhance the forming procedure, resulting in increased efficiency and the production of superior quality items [28].

Up to now, numerous phenomenological models exist, such as the Johnson–Cook (JC) model [29], Khan–Huang (KH) model [30], Khan–Huang–Liang (KHL) model [31-33], Khan–Liang–Farrokh (KLF) model [34], Fields–Backofen (FB) model [35], Molinari–Ravichandran (MR) model [36], Voce–Kocks (VK) model [37,38], Arrhenius equation [39-42], and some other phenomenological models [43]. Furthermore, Hänsel and Spittel introduced a constitutive equation, known as Hänsel–Spittel equation which characterizes flow stress of rigid-plastic materials [44].

Several research groups have strived to formulate constitutive equations that describe the hot deformation behaviors of metals and alloys based on experimentally measured data. Chadha et al [45] aimed to explore how variations in strain rate and temperature affect the compressive deformation behavior of 42CrMo through hot compressive tests. In order to provide the flow stress curves, the hot compressive tests were conducted in Gleeble 3800 at varying temperatures (1050°C, 1100°C, 1150°C, and 1200°C) and different strain rates (0.25, 1, 0.5, 1, 2 s<sup>-1</sup>). They developed a model that describes the interaction between flow stress, strain rate, strain, and temperature. This model is then applied to perform real-time analyses of the process using simulation software. For simulating the process of bulk metal shaping, the Forge NxT 1.0® software is employed, typically relying on thermo-viscoplastic constitutive models designed for high-temperature environments [45]. Figure 2.7 illustrates the contrast between experimental data and flow stress curves calculated using constitutive equations. It can be seen in Figure 2.7 that the model exhibits reasonably accurate predictions for the peak stress at both strain rates. The variation between the calculated peak stress and the experimental peak stress is at its highest, approximately around 7%, for both higher and lower strain rates.

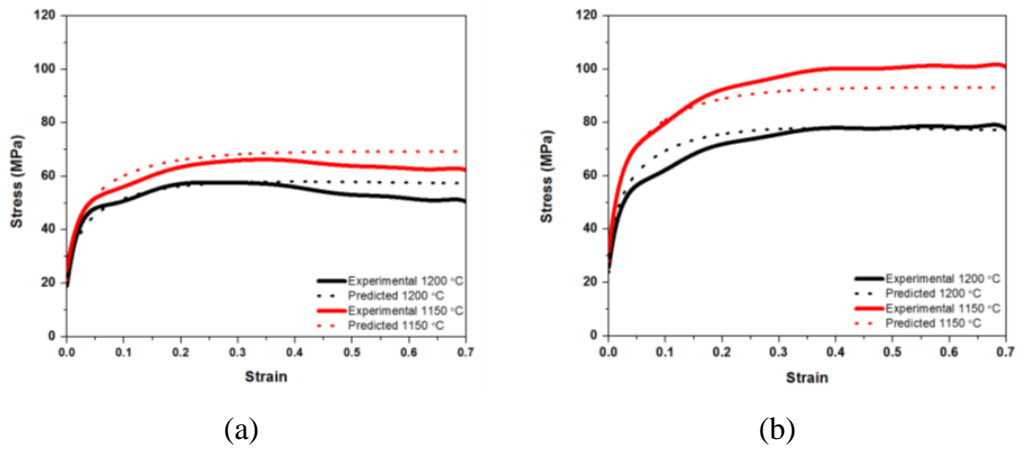


Figure 2.7. Flow curves at strain rate of (a) 0.25s<sup>-1</sup> and (b) 2s<sup>-1</sup> [45]

The temperature distribution chart depicts the final deformation stage for two distinct strain rates, 0.25s<sup>-1</sup> and 2s<sup>-1</sup>, both conducted at a deformation temperature of 1200°C, as illustrated in Figure 2.8. Notably, Figure 2.8 reveals that, when comparing the two, the temperature distribution appears to be more uniform at the higher strain rate compared to the lower one. The temperature pattern depicted in Figure 2.8 indicates that the Hänsel-Spittel equation effectively anticipates the adiabatic heat generation during deformation for both low and high strain rates, particularly in the context of the as-cast 42CrMo alloy [45].

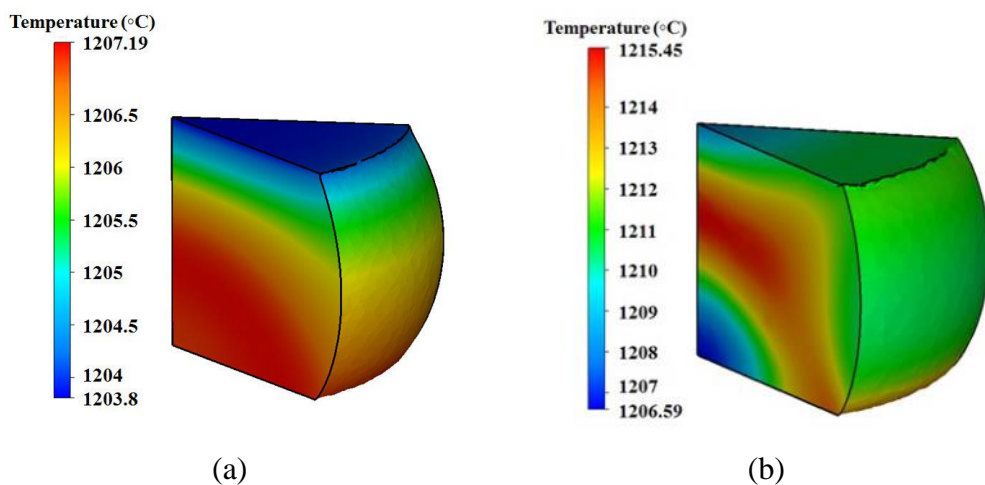


Figure 2.8. The temperature distribution chart at (a) 0.25s<sup>-1</sup> (b) 2s<sup>-1</sup> [45]

El Mehtedi and colleagues [46] employed the Hänsel–Spittel equation for the estimation of flow stress in processed aluminum alloys. Furthermore, the Hänsel–Spittel equation helps to depict how strain, strain rates, temperature, and stress are interrelated in materials like the 6061 aluminum alloy, the Mg–9Li–3Al–2Sr–2Y alloy, the TiAl–Mo alloys, and high-strength steels like HSLA350/440 and DP350/600 [47-50]. Additionally, when considering the hot tensile deformation of the Ti–6Al–4V alloy, the Hänsel–Spittel equation exhibits greater forecasting precision than the strain-compensated Arrhenius-type equation [51].

Wang et al [52] carried out hot compression tests of 20Cr2Ni4A alloy steel on the Gleeble-3500 simulator under isothermal conditions, at temperatures ranging from 973 to 1273 K and strain rates from 0.001 to 1 s<sup>-1</sup>. They employed four distinct constitutive equations for the prediction of flow stress in given alloy. These equations encompassed the original strain-compensated Arrhenius-type equation, the newly adapted modified strain-compensated Arrhenius-type equation, the original Hänsel–Spittel equation, and the modified Hänsel–Spittel equation. To assess the performance of the four constitutive equations, they conducted a comparison based on relative error, average absolute relative error, and the coefficient of determination (R<sup>2</sup>). The modified strain-compensated Arrhenius-type and the modified Hänsel–Spittel equations were derived by refining the deformation temperatures, resulting in enhanced predictive accuracy. These findings indicate that these equations outperform the others in accurately and efficiently estimating the flow stress of 20Cr2Ni4A steel under high-temperature conditions [52].

The majority of research in the field of phenomenological constitutive models, as described in existing literature, predominantly relies on the Arrhenius and Johnson–Cook models and their adapted approaches. However, there are relatively fewer studies that make use of the Hänsel–Spittel model and its variants. It's worth noting that in most cases, the unmodified versions of the Arrhenius and Johnson–Cook models tend to exhibit reduced accuracy [53]. Additionally, FORGE 2011 software has adopted Hänsel–Spittel constitutive equation successfully [45,46,53], whereas every variation of the modified Arrhenius and modified Johnson–Cook models faced

challenges when attempting integration with certain FE modeling software commonly used in the forging industry.

Qiang Liang and colleagues [53] conducted the study on HNi55-7-4-2 alloy, where they developed a high-temperature constitutive model using data from an experimental stress-strain curve acquired during a hot-compression test. They employed the Hänsel–Spittel method and compared the precalculated flow stress values from their model with those obtained through a hot-compression experiment. As shown in Figure 2.9, the flow stress predicted by the constitutive model closely matches the experimental results.

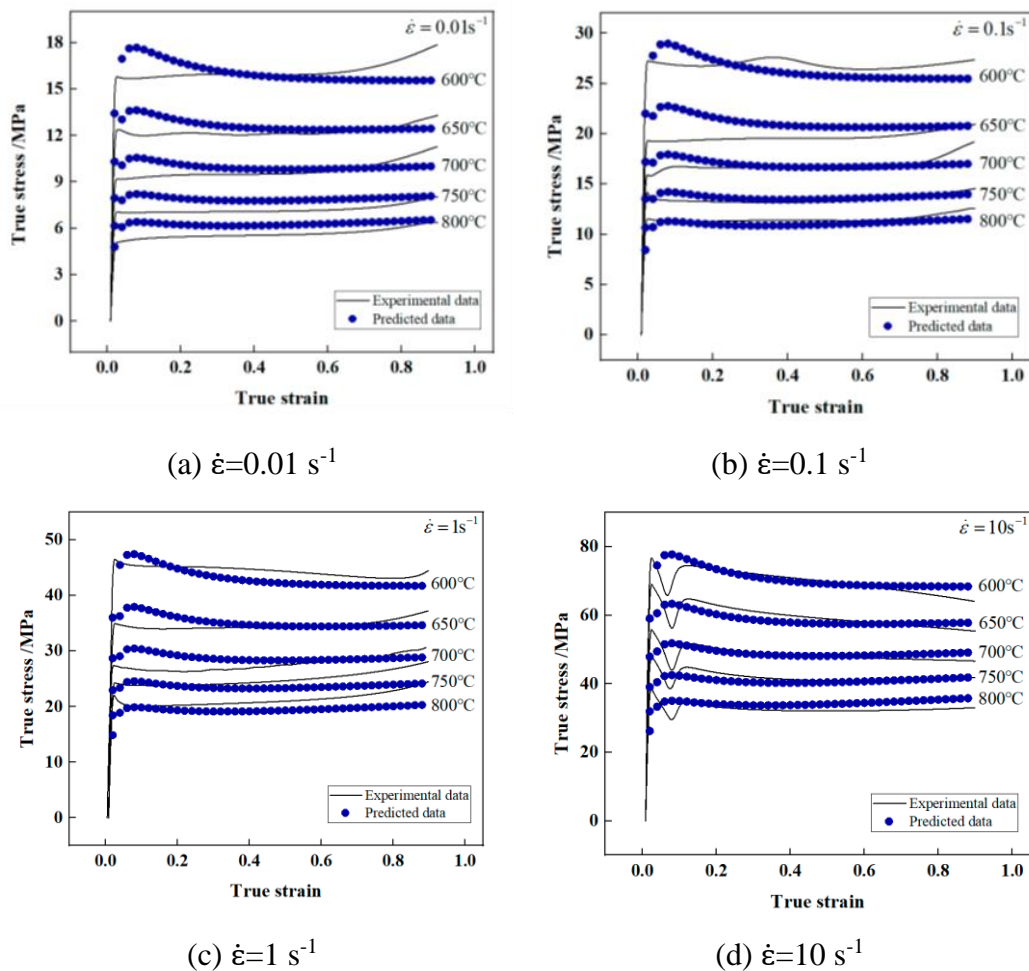


Figure 2.9. Comparing experimental flow stress with predicted values using the Hänsel–Spittel model at  $\dot{\epsilon} = 0.01 \text{ s}^{-1}$ ,  $0.1 \text{ s}^{-1}$ ,  $1 \text{ s}^{-1}$ ,  $10 \text{ s}^{-1}$  [53]

Following theoretical and numerical validation [53], this developed constitutive model was applied in a FEM numerical simulation for the hot precision forging of a synchronizer ring. Through a numerical simulation, an analysis and comparison of metal flow and forging filling were conducted for two different forming strategies. The numerical simulation outcome for plan 1 revealed a clear folding defect at the intersection of the convex key and the side wall, as depicted in Figure 2.10. During the numerical simulation of plan 2, a folding defect (see Figure 2.11) was observed exclusively within the inner flash.

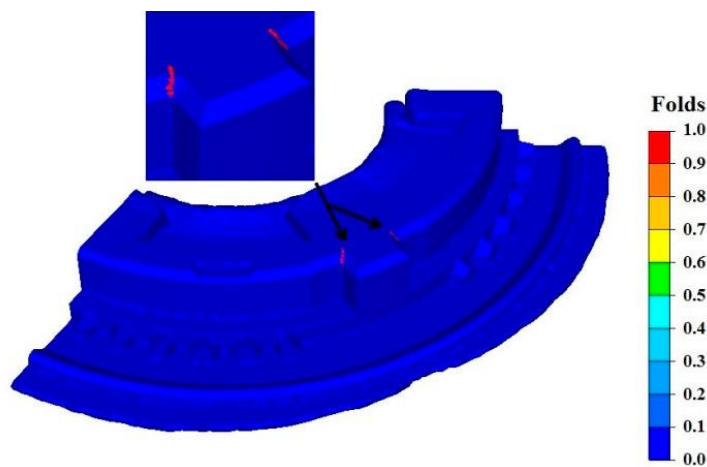


Figure 2.10. Folding defects at the intersection of the convex key and the side wall [53]

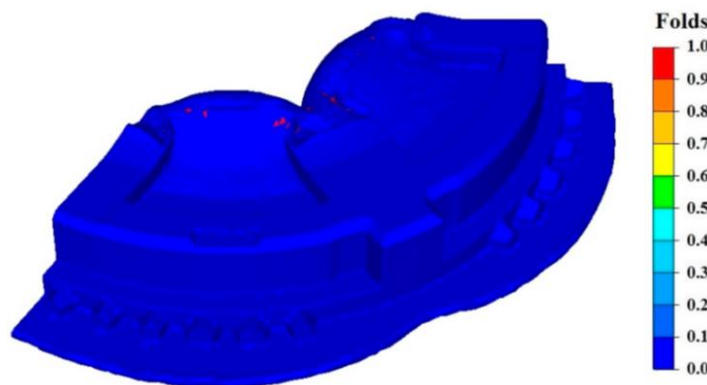


Figure 2.11. Folding defects at the inner flash [53]

As seen in Figure 2.10 and Figure 2.11, workability measures how much a material can be shaped through plastic deformation before it starts to fracture. In other words, workability restricts how much a material can be plastically deformed and strengthened without creating defects in the deforming body [54]. Therefore, in the next subtitle, literature studies related to the ductile damage criterion are presented.

#### **2.2.1.2 Damage Prediction with Ductile Damage Criteria**

In metals, damage refers to the reduction in load-bearing capacity resulting from the development and growth of voids [55]. In other words, the goal in metal forming processes is to avoid depleting the material's formability reserve. When this reserve is fully utilized, it leads to a deterioration in the material's physical properties and the potential for cracks to form, ultimately resulting in a defective product. The design of the forming process strives to establish suitable motion patterns while predicting forces and stresses that do not lead to excessive damage accumulation. Achieving this objective necessitates a deep understanding of the micro-mechanisms responsible for weakening the material [56].

When considering materials susceptible to ductile damage, the accumulation of damage leading to the development of macro-cracks involves a gradual degradation process (Figure 2.12) characterized by three distinct stages: nucleation, growth, and coalescence of micro-voids. Micro-void nucleation takes place in the presence of secondary phase particles or impurities during plastic deformation conditions. Meanwhile, the presence of positive hydrostatic stresses promotes the growth of both newly nucleated and pre-existing micro-voids, resulting in a reduction in the material's homogenized stiffness and strength. When subjected to increased loads, these enlarged micro-voids have a tendency to merge and form a single macro-crack, leading to material failure [56].

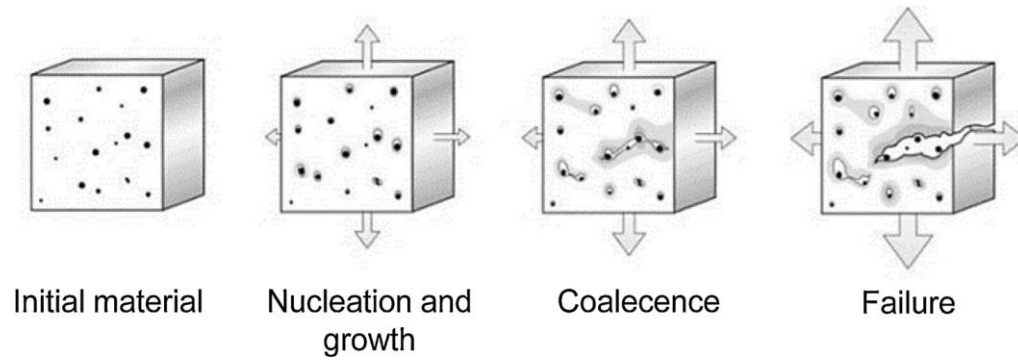


Figure 2.12. Development of failure (macro-crack) [57]

In the realm of published studies, the comprehensive analysis of the ductile failure process leading up to rupture has been explored through three different methodologies: fracture mechanics (FM), micro-scale damage mechanics (MDM), and meso-scale damage mechanics (CDM). FM considers a cumulative threshold of plastic work as a criterion for material failure [56]. Several models have been proposed in the literature, including the Oyane criterion [58], the Freudenthal criterion [59], the Cockcroft Latham criterion [60], and the Brozzo criterion [61].

In the context of metal shaping under elevated temperatures, ductile fracture holds great importance because it represents one of the prevalent failure modes in practical manufacturing processes. The presence of ductile fracture sets the limit on how much strain a particular material can withstand along a specific thermomechanical path. This limit is linked to the conversion of energy within the material due to the accumulation of plastic strains that ultimately lead to fractures. This limit is often quantified using a damage criterion, denoted as (C) in Equation (1). Here,  $\varepsilon_f$  signifies the strain at which fractures occur, and  $\phi$  is a mathematical function that characterizes how stress influences the creation and merging rate of defects such as cracks and voids [62].

$$C = \int_0^{\varepsilon_f} \phi \, d\varepsilon \quad (1)$$



When the total plastic deformation reaches a predetermined critical damage criterion, fracture takes place. This particular aspect of the material's behavior has uncoupled nature and it can be added to existing computer Finite Element (FE) software without requiring additional equations to be incrementally or iteratively satisfied. This simplifies the process, as the only extra task is the straightforward integration of the plastic deformation, enhancing the efficiency of the algorithm. Moreover, the material maintains its non-softening behavior, ensuring the numerical configuration remains well-posed. This means that the simulation maintains its stability and accuracy throughout the process [56].

To effectively quantify ductile failure during the hot formability of the Sn-5Sb alloy, Vafaenezhad et al. [62] conducted a study in which they applied critical damage criteria models. Specifically, Cockcroft and Latham (CL), Zhan (Z), Freudenthal (F), Ayada (A), Oyane (O), Rice and Tracey (RT) and Brozzo (B) models were employed in FEM calculations, incorporating geometric factors from tensile test specimens using the DEFORM 3D simulation software. It's worth noting that identifying necking zone with the highest stress and strain values is crucial for determining critical damage thresholds. Consequently, the damage function also reaches its peak values in this specific location. Citing their research findings, it becomes apparent that there is strong consensus among all fracture criteria and their alignment with instability criteria. This alignment indicates nearly identical zones of unstable flow during hot deformation. Moreover, one can conclude that damage values are influenced by both the testing temperature and the strain rate. The data presented in Table 2.2 show that increased temperatures and decreased strain rates lead to a reduction in the critical damage value. However, the extent of this decrease varied across the different testing conditions [62].

Table 2.2 Critical Damage Function at Different Thermomechanical Conditions

[62]

Damage Criteria	$\dot{\epsilon} = 0.0005$			$\dot{\epsilon} = 0.001$			$\dot{\epsilon} = 0.005$			$\dot{\epsilon} = 0.01$		
	300K	350K	400K	300K	350K	400K	300K	350K	400K	300K	350K	400K
<b>F</b>	12.3	13.5	16.8	22.65	43.2	44	39.2	21.12	19.2	40.25	39.2	30.88
<b>CL</b>	0.26	0.278	0.336	0.49	0.82	0.85	0.81	0.41	0.38	0.75	0.8	0.61
<b>RT</b>	0.4	0.42	0.456	0.58	0.954	0.932	0.91	0.623	0.54	0.954	0.94	0.79
<b>B</b>	0.31	0.29	0.36	0.45	0.52	0.98	0.88	0.23	0.32	0.82	0.88	0.59
<b>O</b>	0.33	0.36	0.45	0.55	0.98	0.89	0.81	0.45	0.38	0.77	0.86	0.42
<b>A</b>	0.39	0.13	0.15	0.28	0.76	0.65	0.6	0.65	0.21	0.22	0.61	0.58
<b>Z</b>	6	7.15	10.45	16.3	36.85	37.36	32.85	14.77	12.58	33.7	32.85	24.63

In the manufacturing processes, the materials used for producing components typically undergo significant deformations. In the case of metals, this involves substantial plastic strains and damage, which profoundly influence the material itself and, consequently, the properties of the end product. Therefore, accurately representing and incorporating this damage in finite element simulations is essential [63].

Yoshino and Shirakashi [64] aimed to explore the influence of prior deformation histories on the alteration of flow-stress, from the perspective of mathematical plasticity theory. They introduced a convenient method for predicting reference stress. This is particularly valuable because measuring dislocation density during an active forming process is impractical, making it an unsuitable tool for the application of the flow-stress equation. Theoretically, work-hardening is intrinsically linked to the plastic deformation energy expended during forming and is commonly referred as the work-hardening hypothesis [65]. Hence, the description of the reference stress ( $\sigma_{st}$ ) should take the form of a function of plastic deformation energy ( $W$ ), presented as follows:

$$\sigma_{st} = f(W) \quad (2)$$

$$W = \int \sigma d\varepsilon \quad (3)$$

The results of Yoshino and Shirakashi's experiment [64] validated this equation. Initially, they subjected SUS430F specimens to compression tests at various strain rates at a temperature of 300 K. Subsequently, they determined their reference stresses. To assess the plastic deformation energies expended during these forming processes, they employed the integration of Equation (3) over the stress-strain curves they measured. In Figure 2.13, the relationship between the measured reference stress ( $\sigma_{st}$ ) and deformation energy ( $W$ ) is presented. The use of the same symbols indicates that these specimens were subjected to the same conditions. The solid curve in the graph illustrates how the reference stress and deformation energy are related, as measured exclusively under the reference condition. Remarkably, the symbols align closely with the solid curve, suggesting that the reference stress is, to a significant degree, influenced by the deformation energy, regardless of the strain-rate history. Therefore, the work-hardening hypothesis outlined in Equation (2) stands as valid for the reference stress. The  $\sigma_{st}$  - $W$  relationship illustrated in Figure 2.13 is unique to each material.

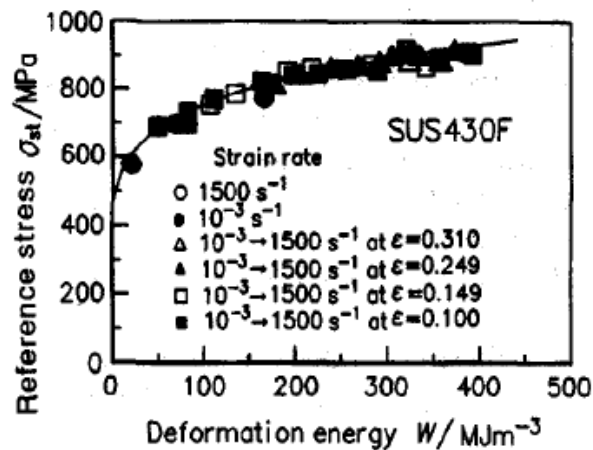


Figure 2.13. Connection between the reference stress and deformation energy [64]

The Latham-Cockcroft fracture criterion [60] doesn't rely on a micromechanical fracture model. Instead, it acknowledges that fracture primarily involves tensile stress and plastic deformation at a macroscopic level. According to the Latham-Cockcroft criterion (Equation (4)), fracture takes place when the total accumulated tensile strain energy surpasses a critical threshold [66].

$$\int_0^{\bar{\epsilon}_f} \sigma_{max} d\bar{\epsilon} = C \quad (4)$$

In this context, " $\sigma_{max}$ " represents the maximum principal stress, " $\bar{\epsilon}$ " stands for the equivalent strain, " $\bar{\epsilon}_f$ " denotes the equivalent strain where fracture takes place and "C" is a constant that is determined through experimental analysis specific to the material, temperature, and strain rate under consideration. This principle derives from the broader idea put forward by Freudenthal [59] that fracture takes place when the plastic work per unit volume exceeds a critical threshold. Gouveia and colleagues [67] demonstrated through both experiments and finite-element analysis that the Latham-Cockcroft criterion yielded the most accurate predictive performance. The Latham-Cockcroft criterion, through the integration of tensile plastic work across the entirety of the metalworking process, quantifies the cumulative effects on the microstructure, including occurrences such as microvoid formation, void growth, and coalescence, all resulting from tensile stresses and plastic deformation. Fracture is initiated when this cumulative measure reaches the critical value denoted as "C" [66].

In Figure 2.14, the fracture strain line, as predicted by the Latham-Cockcroft criterion, Equation (4), displays a reasonable alignment with experimental results obtained through a simple compression test involving the upsetting of a cylinder. Furthermore, among the available options, implementing the Latham-Cockcroft criterion in a finite-element analysis code is the most straightforward [66].

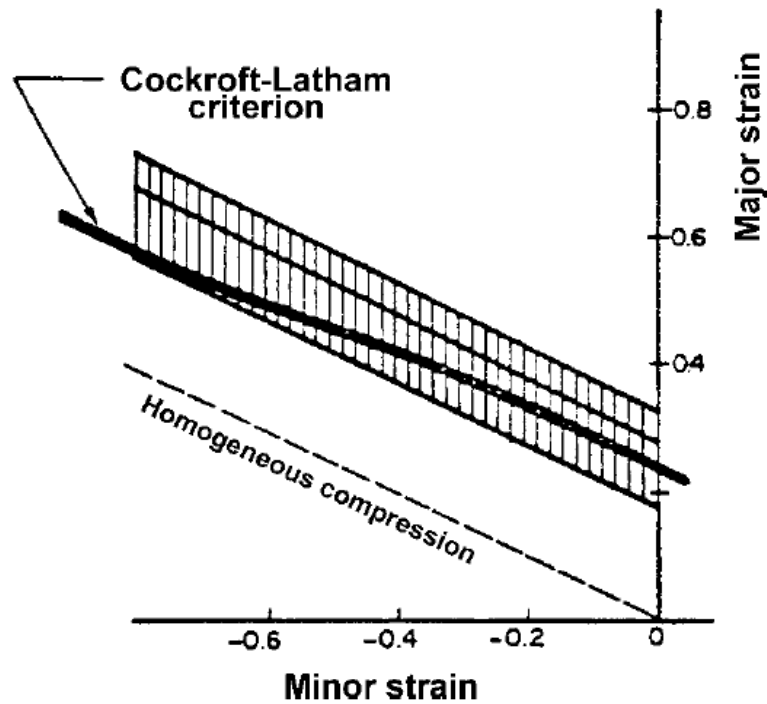


Figure 2.14. Fracture lines prediction with the Latham-Cockcroft criterion and experimentally (Shaded Region) [66]

Another instance [68] of utilizing the Cockcroft-Latham criterion is demonstrated through the application of the DEFORM code to simulate plastic deformation processes. This simulation focused on axisymmetric extrusion, as illustrated in Figure 2.15. The Latham-Cockcroft criterion was integrated into the process, allowing for a thorough assessment of stresses and strains during extrusion. This analysis helped identify areas with substantial microstructural damage. It became evident that as damage accumulated, the simulation predicted the occurrence of central burst after the third reduction, a phenomenon commonly observed in such processes [68].

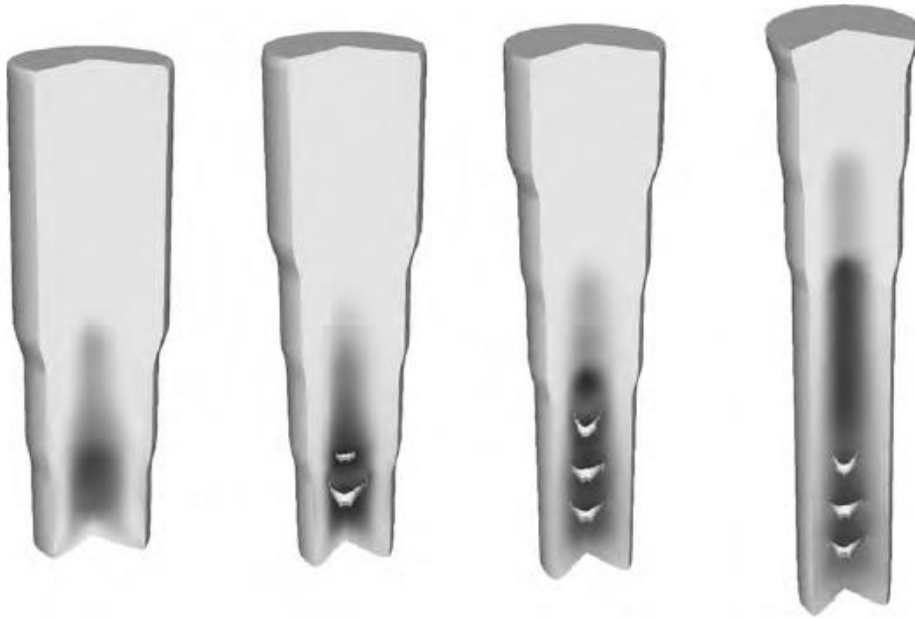


Figure 2.15. Latham-Cockcroft criterion predictions for internal damage and central burst in DEFORM [68]

In the study by Gontarz and Piesiak [69], the paper outlines an approach for establishing the threshold value of the normalized Latham-Cockcroft damage criterion specifically tailored for the titanium alloy Ti6Al4V. This criterion plays a pivotal role in forecasting material fractures during metal forming processes. The methodology involves subjecting necking specimens to tensile tests until they reach failure, which are carried out at room temperature with a velocity of 100 mm/min. Subsequently, numerical simulations of the experiments are created using the DEFORM 3D program based on the Finite Element Method (FEM). The integral was computed at key points within the specimen cross sections, as illustrated in Figure 2.16. These points experienced displacement during the tensile testing of the specimens.

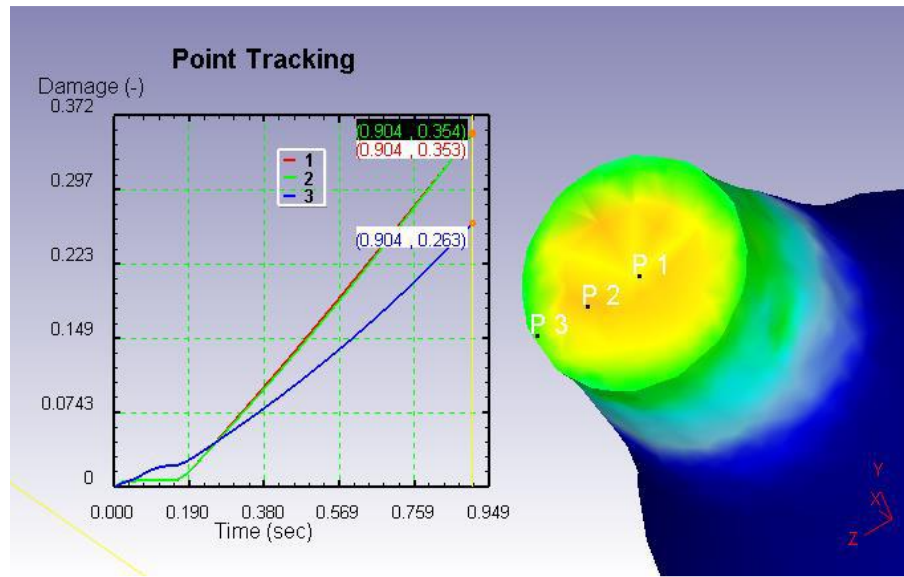


Figure 2.16. Distribution of the Latham-Cockroft damage criterion: cross-sectional analysis with notable measurement points [69]

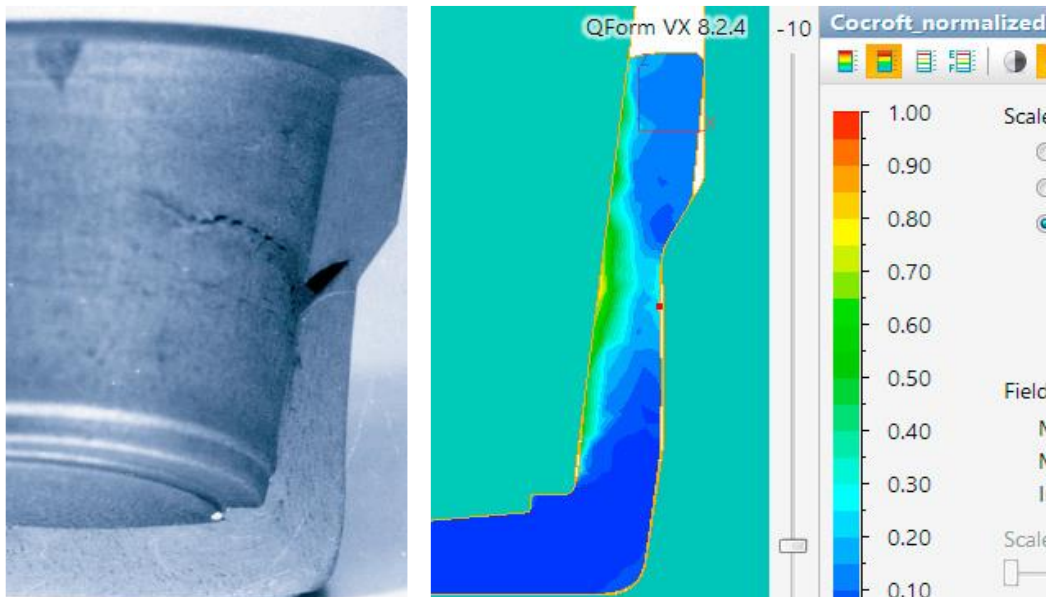
Based on the normalized Latham-Cockroft integral values at the point of fracture for all specimens, it was observed that the maximum integral value at the moment of fracture was consistently found in the central area of the cross section (specifically, at points P1 and P2 in Figure 2.16). By comparing the results from both the physical tests and the numerical simulations, the critical boundary value for the normalized Latham-Cockroft criterion is determined. This highest value at the point of fracture, which equated to 0.354, was selected as the critical threshold for fracture under the experimental conditions [69].

Chen et al. [70] utilized Latham-Cockroft's ductile failure criteria to highlight the connection between material fracture and the equivalent stress of deformation. They stated that the forming limit of the material in terms of fracture energy, calculated by multiplying the effective deformation with a normalized ratio obtained by dividing the maximum principal stress by the equivalent stress. The normalized version of the Latham-Cockroft ( $LC_n$ ) criterion simplifies the equation to a dimensionless form, as presented in Equation (5) below, where " $\sigma_{max}$ " represents the maximum principal stress, " $\bar{\sigma}$ " is the equivalent stress (Von Mises stress), " $\bar{\epsilon}$ " represents the equivalent

strain, and " $\bar{\epsilon}_f$ " indicates the equivalent strain that marks the fracture limit. The  $LC_n$  damage triggering value is denoted by the symbol C.

$$\int_0^{\bar{\epsilon}_f} \frac{\sigma_{max}}{\bar{\sigma}} d\bar{\epsilon} = C \quad (5)$$

Stebunov et al. [71] aimed to figure out when the standard Cockcroft-Latham criterion works and how it's similar to other criteria in cold forging process. Their goal was to adjust the criterion to consider the stress conditions and how they affect the critical plastic strain. The process of cold forging a cap from C40 steel (DIN standard) involves three distinct operations and workpiece damage as depicted in Figure 2.17(a) occurs during the third operation. Figure 2.17(b) displays the distribution of the normalized Latham-Cockcroft criterion [70] (Cockcroft-Latham-Oh criterion), with a maximum value of 0.84 also located in the region of actual fracture [71].



(a) Photo of Cold-Forged Part Manufactured from C40      (b) Normalized Cockcroft-Latham-Oh Damage Criterion Distribution

Figure 2.17. Workpiece damage occurs in third operation [71]



In their research, they demonstrated that the critical value  $C_1$  in the normalized Cockcroft-Latham-Oh criterion is not a fixed material property; instead, it is influenced, at the very least, by the stress state [71].

In reference [72], utilizing the normalized Latham-Cockroft criterion, Lin et al. formulated a ductile damage model aimed at forecasting the ductile damage characteristics of 42CrMo under high-temperature deformation. The critical damage variable of the normalized Cockcroft and Latham failure criterion is adjusted to include the impact of deformation temperature and strain rate. This modification allows for the evaluation of fracture occurrence in the context of a hot forging process. Thus, its effectiveness in predicting failures at the points where the workpiece interfaces with the die's corners is demonstrated (Figure 2.18). The hot forging trials were subjected to FE simulations using DEFORM-3D. Prior to simulation, the user subroutine incorporated the validated ductile damage model within DEFORM-3D commercial software which enables the prediction of fracture displacements. The comparison between the projected and observed fracture displacements reveals a substantial agreement.

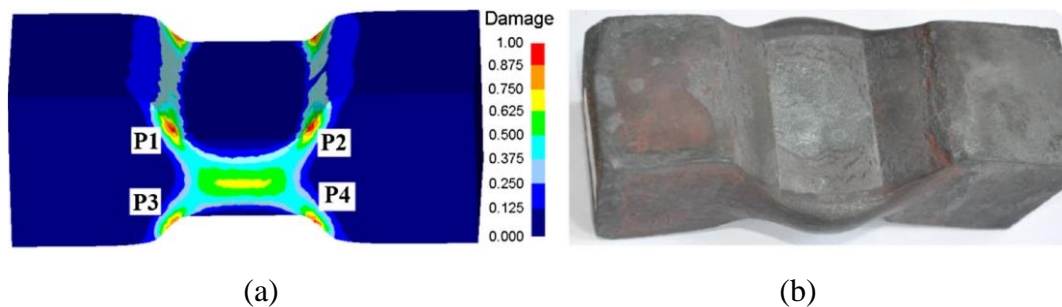


Figure 2.18. Fracture initiation sites: (a) predicted by FEA (b) experimentally observed in the forging experiment [72]

They also explored the correlation between the threshold value  $LC_n$  and the conditions of deformation. At relatively high strain rates ( $0.01$  and  $0.1 \text{ s}^{-1}$ ), the  $LC_n$  value initially rises and then declines with increasing deformation temperature.

Conversely, under relatively low strain rates (0.0001 and 0.001 s<sup>-1</sup>), the LC<sub>n</sub> value decreases as the deformation temperature increases. A comparable pattern is observed in the relationship between fracture strain and deformation conditions. This phenomenon arises from the interplay of dynamic recrystallization and grain coarsening during the hot deformation process [72].

### **2.3 Summary and Conclusions**

This literature review has been conducted to examine studies that would provide valuable insights into the simulation of process chains for aerospace bearings. Given the paramount importance of achieving the desired deformation in plastic forming processes without causing material fractures, this review explores the research necessary for conducting precise simulations of industrial processes. While there has been a notable increase in both mechanical and numerical studies in recent decades, a significant gap exists in the literature when it comes to the simulation of the manufacturing chain of aerospace bearings.

The simulation of this specific manufacturing chain is a critical aspect within the aviation industry, and its absence in existing research highlights the need for further investigation. Addressing this gap in the literature is essential for enhancing the understanding of aviation bearing production processes and ensuring their reliability and performance in aerospace applications.

## CHAPTER 3

### MATERIAL CHARACTERIZATION AND MODELLING MATERIAL BEHAVIOUR

The initial step in achieving product requirements involves the construction and subsequent optimization of manufacturing process chains. Within the aerospace sector, the primary focus of industry lies in minimizing defects during component manufacturing and enhancing their service life. Considering the longevity of these components, it is important to recognize that the manufacturing processes within these chains may introduce defects, thus diminishing their overall lifespan.

The realism of computer simulations relies on the suitability of the underlying numerical algorithms and the quality of the data used to describe the properties of the metal. Therefore, advanced material models are indispensable in order to obtain precise outcomes from simulations of the forming processes. In order to accurately represent the material behavior, Finite Element (FE) modeling of large deformation manufacturing processes like forging necessitates the generation of a comprehensive set of material properties.

The thesis work on “Process-Chain Simulation of Manufacturing of Aerospace Bearings” began with the primary focus on material characterization. The chemical composition of M50 steel is provided below.

Table 3.1 Chemical Analysis (Wt%) [Carpenter Technology, USAS, M50 VIMVAR, Diameter: 45.00 mm]

<b>C</b>	<b>Si</b>	<b>Mn</b>	<b>S</b>	<b>P</b>	<b>W</b>	<b>Cr</b>	<b>V</b>	<b>Ni</b>	<b>Mo</b>	<b>Co</b>	<b>Cu</b>
0.83	0.20	0.25	0.001	0.006	0.01	4.12	1.00	0.12	4.25	0.03	0.06

The superior characteristics of M50 steel are associated with its alloying elements and carbides, leading to both secondary hardening and reduced plasticity during hot-working procedures for M50 steel. As a consequence, M50 bearing steel generally demonstrates reduced deformability within a relatively narrow scope of hot working processing conditions [11]. Accordingly, obtaining a precise material dataset and determining the yield curves are essential steps for this thesis study in order to incorporate the mechanical properties of the M50 material into the Finite Element (FE) analysis.

### **3.1 Material Characterization w/ Computational Methods**

First part of material characterization involves extracting the computational material dataset and correlating it with experimental compression test results. Initial research focused on determining the suitable temperature range for hot forging process by inputting the chemical composition data of the as-received M50 steel into the JmatPro program.

By utilizing the data from the "Step Temperature" and "Processing Map" files of the JmatPro program, the forging temperature range of the as-received M50 steel was approximately determined to be 1000°C-1200°C. This decision was made due to the fact that M50 steel starts melting at around 1250°C, and therefore, it was concluded that temperatures should not exceed 1200°C to prevent any local melting caused by segregation.

Subsequently, at temperatures below 1000°C, flow instability was observed at high velocities. At forging temperatures below 1000°C, vanadium carbides remain incompletely dissolved. This can hinder grain growth, which is beneficial, but it may also lead to rapid tool wear. For this reason, it was decided to start the experimental studies for material characterization at 1000°C, and to avoid local melting, the characterization tests were planned to be completed at a maximum temperature of 1150°C. This outlined the roadmap for these studies.

### **3.2 Material Characterization w/ Experimental Methods**

Finite element (FE) modeling of manufacturing processes often demands a substantial flow stress dataset at high plastic strains to accurately represent the material's behavior under a wide range of temperatures and strain rates. The relevant plastic flow stress data is typically derived from axisymmetric compression testing, covering a wide range of temperatures and strain rates. Although isothermal compression tests are commonly used, it is important to acknowledge that the material's microstructure can be significantly influenced by the soak time. The soak time can noticeably affect the material's microstructure, potentially leading to differences in how it behaves during the actual processing. Therefore, conventional material testing techniques offer accurate determination of fundamental material properties, exemplified by measurements of Young's modulus.

Another methodology involves conducting a compression test immediately after rapid heating, similar to the approach utilized in the Gleeble (thermo-mechanical simulator). Gleeble utilizes the resistance heating technique to attain elevated heating rates. After reaching the target test temperature at the specified heating rate, the compression test is conducted, as obtaining a precise material dataset and developing the flow curves are essential steps for this study. In this context, as the first phase of the thesis, compression tests of the M50 material were conducted using the Gleeble thermo-mechanical testing system to incorporate the mechanical properties of the material into the finite element simulation studies. The compression test results provided precise yield curves for the M50 material.

The Gleeble® 3800 (a thermo-mechanical simulator, Dynamic Systems, Inc.) was employed for the uniaxial hot compression testing. These steps are essential to incorporate the thermo-mechanical properties of the M50 material into the finite element analysis of the complete process chain, including the hot forging process. The Gleeble system is equipped with closed-loop thermal control and hydraulic servo systems, both regulated by a synchronized digital controller. This setup ensures accurate testing and physical simulations.

The heating system uses a direct current method and features jaws with a heating rate of 10000°C/s and a cooling rate of 10000°C/s, due to their high thermal conductivity. The direct resistance heating method and closed-loop thermal control provide significantly higher temperature uniformity compared to conventional furnaces. So, all tests were conducted under isothermal conditions [73]. To obtain reliable data from compression testing, there are many factors to consider throughout the entire process, from sample preparation to data analysis. A significant portion of these criteria is ensured by the ASTM E209 standard [74].

While there are no specific restrictions on sample dimensions, it is noted that height/diameter (H/D) ratios between 1 and 2 are acceptable, with a recommendation for a value of 1.5 [73-76]. So, based on the recommendations from ASTM E209 [74] and reference sources in the field, it was decided to use samples with a height of 15 mm and a diameter of 10 mm (H/D = 1.5). Within this context, M50 test specimens were initially prepared for the Gleeble 3800 according to the technical drawings provided in Figure 3.1.

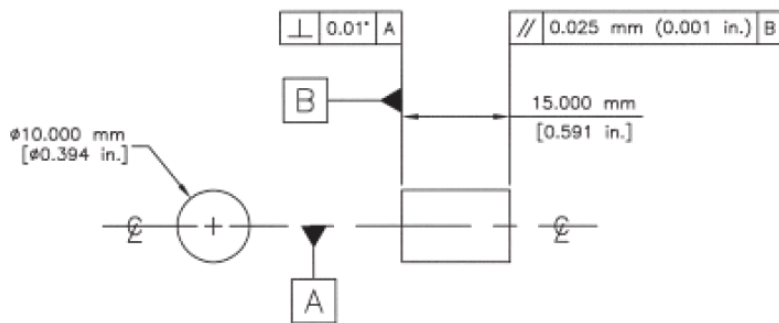


Figure 3.1. Compression test specimens of M50 for the Gleeble 3800

As it seen in Figure 3.1, the compression tests were carried out on cylindrical specimens machined with a diameter of 10 mm and a height of 15 mm (H/D=1.5). Additionally, the specimen's ends were maintained in parallel to ensure uniform deformation throughout the testing process.

The input data for the FE analysis needs to meet two requirements: (1) encompassing the non-linear relationship between flow stress, temperature, and strain rate, as well as how this connection changes with strain; (2) covering the complete range of deformation conditions that the workpieces go through. In an ideal and uniform compression scenario, the sample retains its cylindrical shape, experiencing uniform temperature, strain rate, and strain. However, in real-world situations, it is unavoidable to encounter some level of non-uniform deformation and barrel-like distortion in the sample. These happen as a result of an inhomogeneous temperature distribution and friction while testing. The temperature gradient arises from two primary factors: heat conduction towards the colder platens and localized plastic dissipation in the center of the workpiece [77].

Figure 3.2 shows the barreling effect on stress-strain curve. As it can be seen in Figure 3.2 (c), the stress-strain data acquired from a barrel-shaped sample in experiments varies from the stress-strain curve obtained in an ideal, frictionless condition without any barreling. Barreling arises from the friction between the platens and the specimen, leading to a triaxial stress state, which contrasts with the ideal uniaxial stress condition. The stress-strain curve obtained through experiments on a barreling specimen diverges from the actual stress-strain curve, which assumes ideal uniaxial stress conditions. Hence, it's not possible to completely eliminate the friction between the platens and the specimen in hot compression testing when seeking to acquire the actual material properties [78].

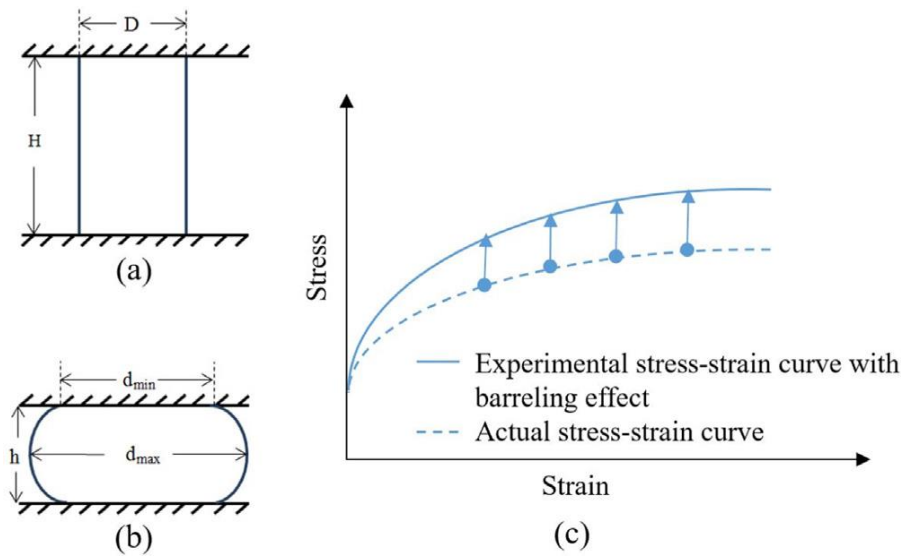


Figure 3.2. (a) Initial cylinder size before compression (b) Final cylinder size after compression; (c) Impact of barreling on stress-strain curve [78]

Using the Gleeble 3800, a series of hot compression tests were performed at four distinct temperatures ( $1000^{\circ}\text{C}$ ,  $1050^{\circ}\text{C}$ ,  $1100^{\circ}\text{C}$ , and  $1150^{\circ}\text{C}$ ) and three varying strain rates ( $0.1\text{ s}^{-1}$ ,  $1\text{ s}^{-1}$ ,  $10\text{ s}^{-1}$ ). Following hot compression tests on the Gleeble 3800, the M50 test specimens showed barreling. As mentioned before, in this thesis, the initial constitutive data were acquired from the uncorrected experimental data and they provided to the Finite Element (FE) model must be sufficiently accurate to represent the actual behaviour of the tested M50 steel. For this reason, corrections based on friction and heating factors were made to the uncorrected experimental data obtained from compression tests conducted on Gleeble 3800.

The temperature can be below the nominal temperature near the platens which are initially cold surfaces and above the nominal temperature at the center of the sample due to adiabatic heating, especially at higher strain rates. Besides, effects like deformation irregularities and localized distortion contribute to achieving maximum strains and strain rates that surpass the nominal values. As a result, derived from the



experiments, uncorrected  $\sigma(T, \dot{\epsilon}) - \epsilon$  graphs were obtained and subsequently reliably corrected by considering factors such as friction and heating.

During the uniaxial compression test, the barrelling of the sample gradually results in a biaxial stress state. Initially, (Coulomb) friction correction is implemented utilizing Equation (6).

$$\sigma_a(t) = \sigma_{fc}(t) \left[ 1 + \frac{1}{3} \mu \left( \frac{d(t)}{h(t)} \right) \right] \quad (6)$$

Here,  $\sigma_a$  indicates the stress measured from the axial extensometer prior to correction, whereas  $\sigma_{fc}$  signifies the stress after friction correction under uniaxial conditions. Additionally, in this equation,  $d(t)$  and  $h(t)$  are the time-dependent diameter and height data, respectively, and  $\mu$  is the coefficient of friction [79].

Although the correction is theoretically straightforward, it necessitates understanding of the friction coefficient ( $\mu$ ). Determination of the friction coefficient involved utilizing the connection between the friction constant ( $c$ ) and the barrelling coefficient ( $B$ ), as outlined in Equation (7) and detailed in [80].

$$\mu = c * \left( 1 + B^{1/2} \right) \quad (7)$$

The barrelling coefficient ( $B$ ), described in Equation (7), quantifies the extent of barrelling observed in compression tests. It is determined using the initial height ( $h_0$ ), final height ( $h_f$ ), initial diameter ( $r_0$ ), and maximum diameter ( $r_m$ ) of the specimens. The formula for calculating the  $B$  value is presented in Equation (8).

$$B = \frac{h_f(r_m)^2}{h_0(r_0)^2} \quad (8)$$

In the Gleeble 3800 compression tests, graphite plates and nickel paste are applied between the jaws and the specimen to minimize friction. To calculate the barrelling coefficient ( $B$ ), the height and diameter of the M50 compression specimens were measured both before and after the test, as described in Equation (8). Using these measurements, the barrelling coefficient ( $B$ ) was calculated. Subsequently, the

friction coefficient ( $\mu$ ) was calculated based on the relationship between the friction constant ( $c$ ) and the barrelling coefficient ( $B$ ), as outlined in Equation (7) [80]. In this study, the friction constant ( $c$ ) was derived from the finite element analysis results shown in Figure 3.3 [80], which were then used to calculate the friction coefficient ( $\mu$ ).

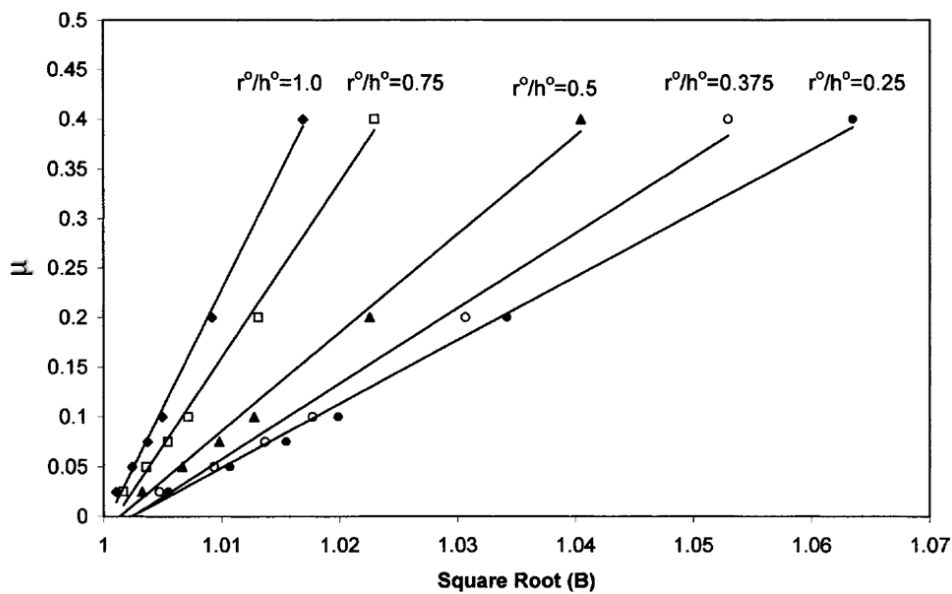


Figure 3.3. Correlation between the square root of the barrelling coefficient ( $B^{1/2}$ ) and the friction coefficient ( $\mu$ ) for various specimen diameter/height ratios [80]

After applying the friction correction, the heating correction was carried out using the formulation described in Equation (9). Here,  $\sigma(t)$  signifies the corrected yield stress over time, and  $\Delta T(t)$  represents the temperature increase at any moment during the experiment. The term  $d\sigma/dT$  indicates the variation in the material's yield strength with temperature at a given strain rate. This accuracy ensures that the model can capture the primary effects of non-uniform deformation conditions.

$$\sigma(t) = \sigma_{fc}(t) - \Delta T(t) \frac{d\sigma}{dT} \quad (9)$$

Figure 3.4 to Figure 3.6 show both the uncorrected and corrected stress-strain curves from hot compression tests which were conducted at temperatures of 1000°C, 1050°C, 1100°C and 1150°C with varying strain rates (0.1 s<sup>-1</sup>, 1 s<sup>-1</sup>, and 10 s<sup>-1</sup>).

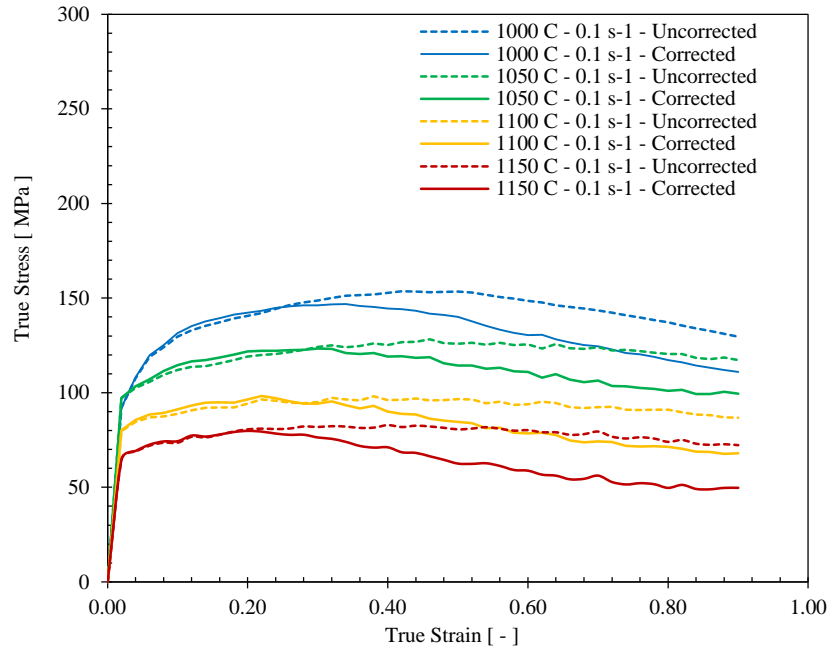


Figure 3.4. Uncorrected and corrected flow curves at 1000°C, 1050°C, 1100°C, and 1150°C with a 0.1 s<sup>-1</sup> strain rate

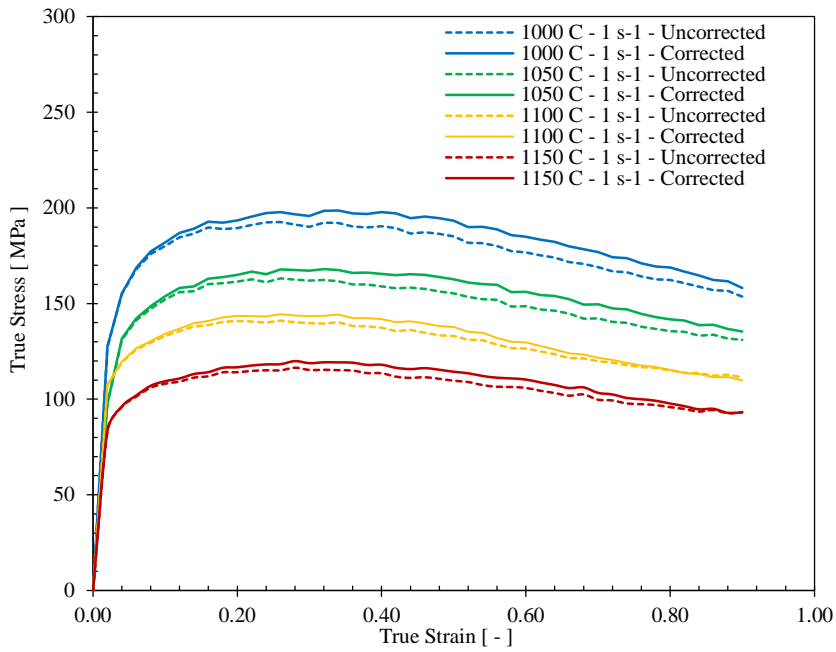


Figure 3.5. Uncorrected and corrected flow curves at 1000°C, 1050°C, 1100°C, and 1150°C with a 1 s<sup>-1</sup> strain rate

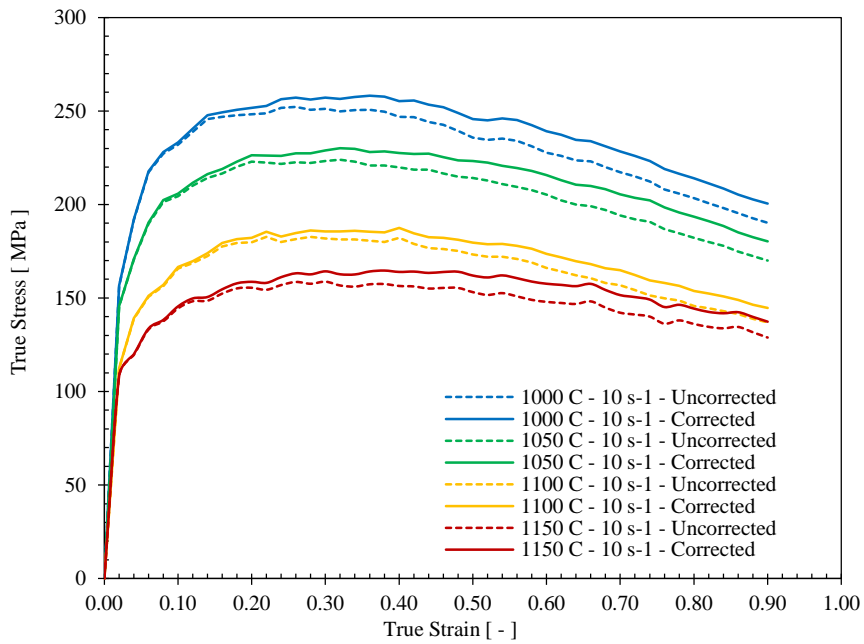
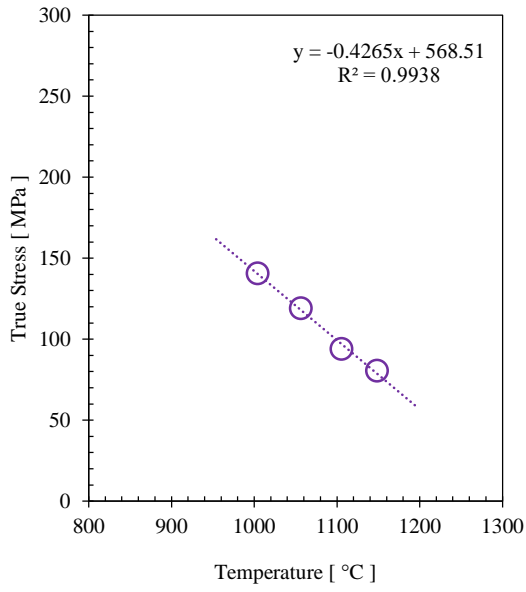


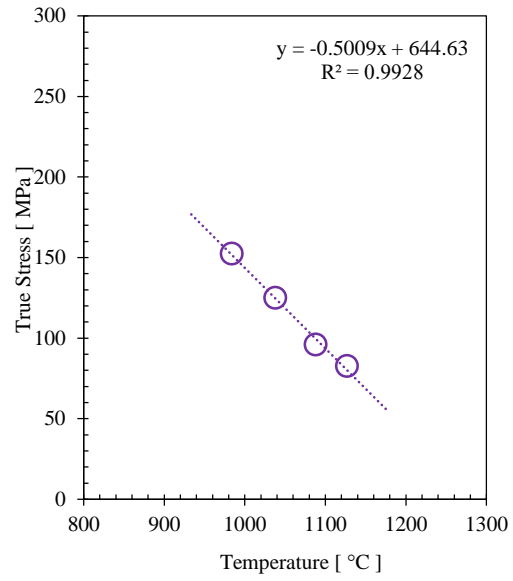
Figure 3.6. Uncorrected and corrected flow curves at 1000°C, 1050°C, 1100°C, and 1150°C with a 10 s<sup>-1</sup> strain rate

Figure 3.4 to Figure 3.6 illustrate the flow stress curves of M50 steel under various deformation conditions, showing a gradual increase in stress as the strain rate rises from  $0.1 \text{ s}^{-1}$  to  $10 \text{ s}^{-1}$  at a constant temperature. This occurs because Dynamic Recovery (DRV) mechanism depends on both time and temperature, and its contribution lessens as the strain rate increases and the temperature decreases. The flow stress curves also display peaks corresponding to Dynamic Recrystallization (DRX). These peaks appear at lower strains as the strain rate increases and temperature decreases. This is expected because the nucleation of recrystallized grains requires reaching a critical dislocation density, which is more easily achieved at lower temperatures and higher strain rates due to decreasing DRV.

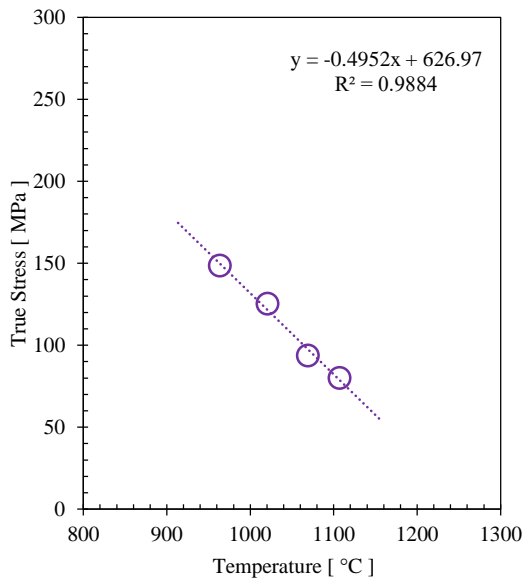
The stress correction was deducted from the true stress–strain curves derived from the M50 Gleeble experiments. The R-squared (the Coefficient of Determination) values obtained after the correction process are presented in Figure 3.7, Figure 3.8, Figure 3.9 for each strain rate and temperature.



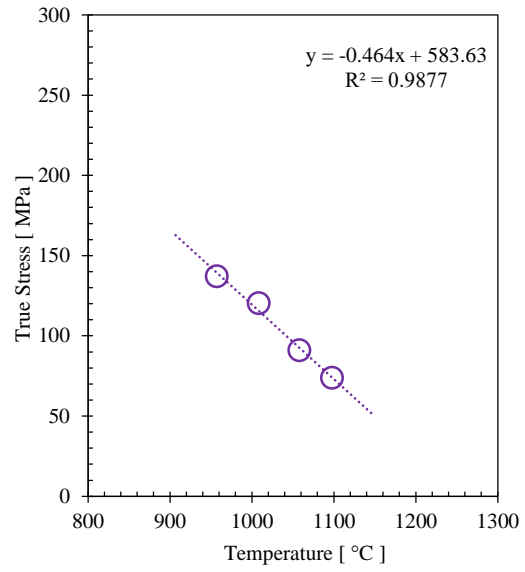
a)  $\epsilon=0.2, \dot{\epsilon}=0.1 \text{ s}^{-1}$



b)  $\epsilon=0.4, \dot{\epsilon}=0.1 \text{ s}^{-1}$

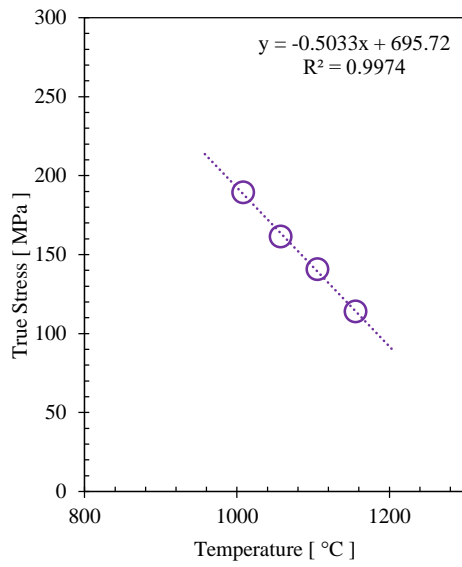


c)  $\epsilon=0.6, \dot{\epsilon}=0.1 \text{ s}^{-1}$

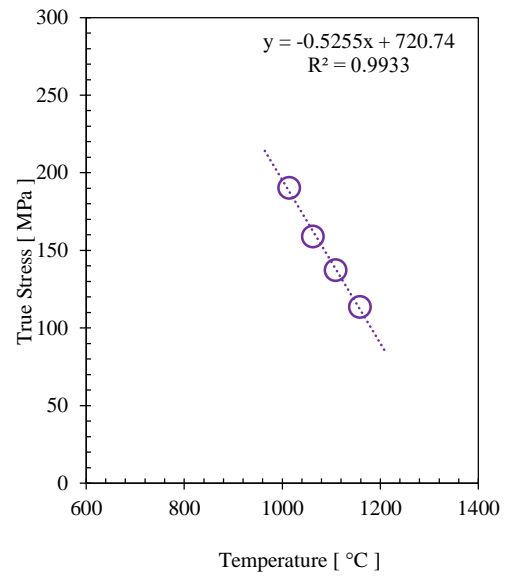


d)  $\epsilon=0.8, \dot{\epsilon}=0.1 \text{ s}^{-1}$

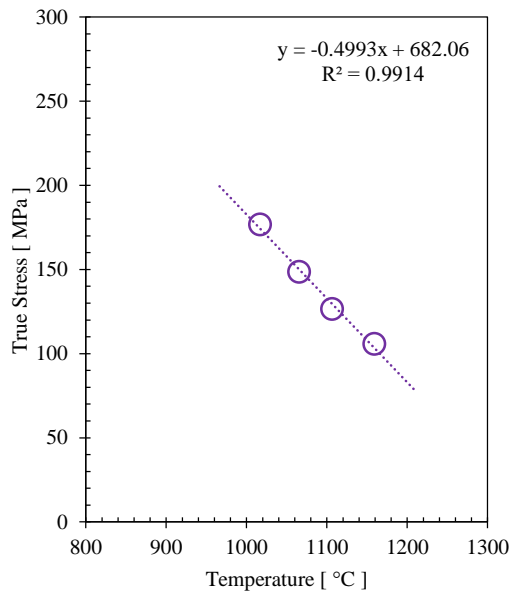
Figure 3.7.  $T= 1000^\circ\text{C}, 1050^\circ\text{C}, 1100^\circ\text{C}, 1150^\circ\text{C}$  ( $\dot{\epsilon}=0.1 \text{ s}^{-1}$ )



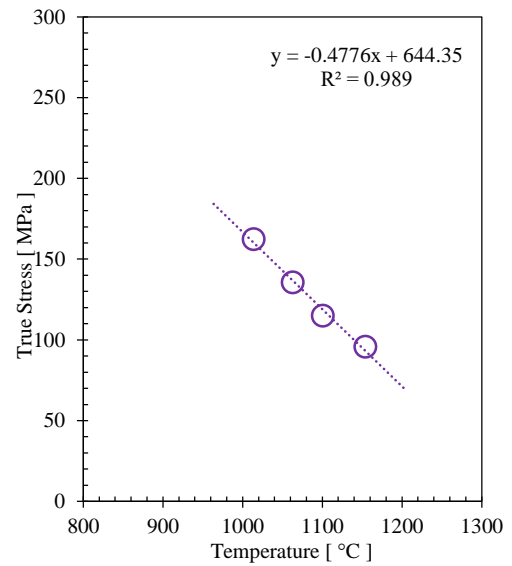
a)  $\epsilon=0.2, \dot{\epsilon}=1 \text{ s}^{-1}$



b)  $\epsilon=0.4, \dot{\epsilon}=1 \text{ s}^{-1}$

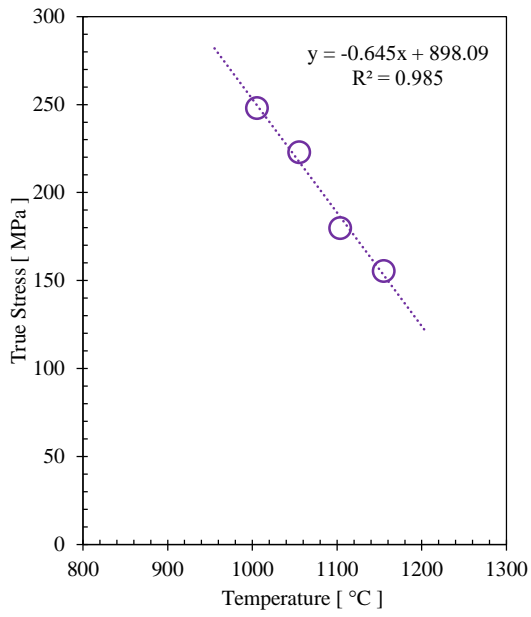


c)  $\epsilon=0.6, \dot{\epsilon}=1 \text{ s}^{-1}$

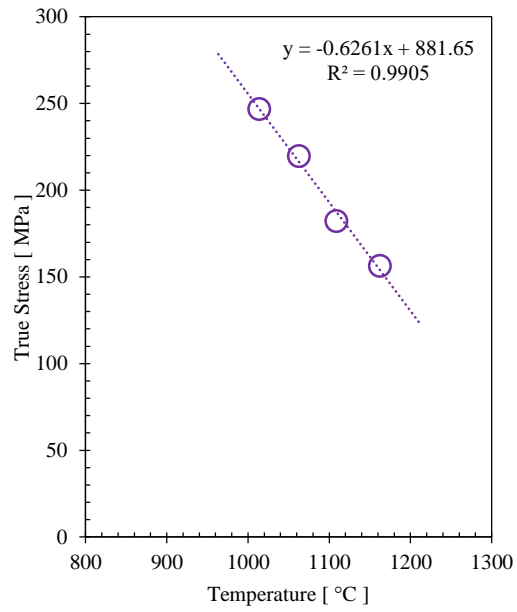


d)  $\epsilon=0.8, \dot{\epsilon}=1 \text{ s}^{-1}$

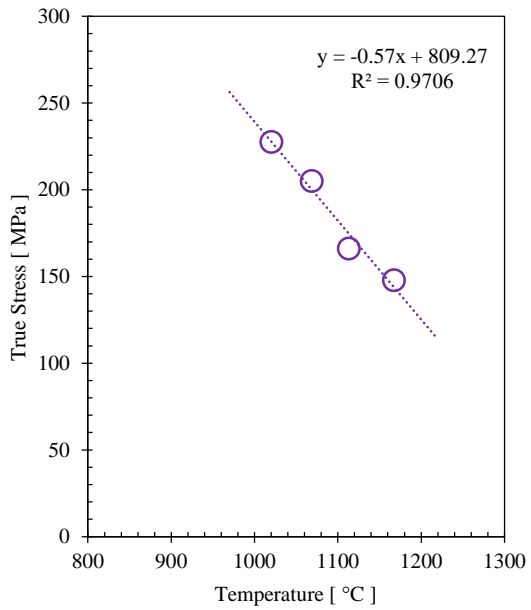
Figure 3.8.  $T=1000^\circ\text{C}, 1050^\circ\text{C}, 1100^\circ\text{C}, 1150^\circ\text{C}$  ( $\dot{\epsilon}=1 \text{ s}^{-1}$ )



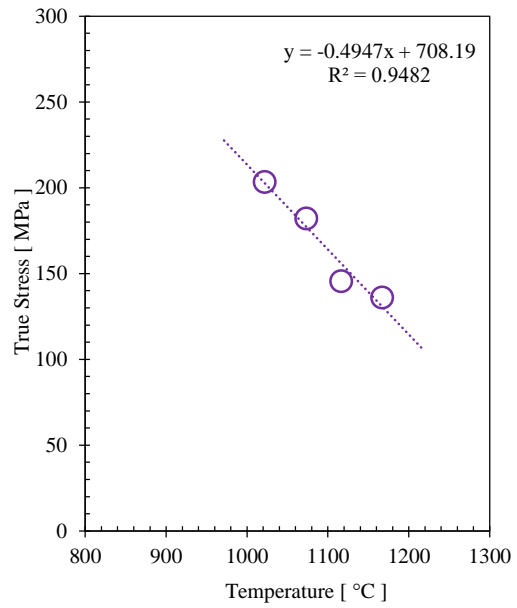
a)  $\epsilon=0.2$ ,  $\dot{\epsilon}=10 \text{ s}^{-1}$



b)  $\epsilon=0.4$ ,  $\dot{\epsilon}=10 \text{ s}^{-1}$



c)  $\epsilon=0.6$ ,  $\dot{\epsilon}=10 \text{ s}^{-1}$



d)  $\epsilon=0.8$ ,  $\dot{\epsilon}=10 \text{ s}^{-1}$

Figure 3.9.  $T=1000^\circ\text{C}, 1050^\circ\text{C}, 1100^\circ\text{C}, 1150^\circ\text{C}$  ( $\dot{\epsilon}=10 \text{ s}^{-1}$ )



The values of  $R^2$  (the Coefficient of Determination) derived from the correction process are outlined in Table 3.2, indicating that values closely approaching "1" were observed.

Table 3.2  $R^2$  values from the curve-fitting procedures

$R^2$				
$\dot{\epsilon}$ ( $s^{-1}$ )	$\epsilon$ (-)			
	0.2	0.4	0.6	0.8
0.1	0.9938	0.9928	0.9884	0.9877
1	0.9974	0.9933	0.9914	0.989
10	0.985	0.9905	0.9706	0.9482

The elevated  $R^2$  values shown in Table 3.2 make it clear that the proposed model offers a highly accurate estimate of the stress-strain curves for all the examined experimental results.

### 3.3 Modelling Material Behaviour

In cold forming processes, materials usually exhibit elastoplastic behaviour, whereas hot forming processes are better described by viscoplastic behavior because the effect of elasticity is minor compared to viscoplasticity at high temperatures. The metal experiences considerable deformations, leading to a significant plastic response. Consequently, the viscoplastic model is mainly applied to hot-forming materials. Thus, Forge NxT 3.2® simulation software employs rigid viscoplastic behaviour, a typical characteristic of hot-worked metals, along with "Hänsel-Spittel" strain hardening phenomena. It applies the Von Mises yield criterion with an associated flow rule and incorporates a regularization technique to correct self-inconsistency at the beginning of the flow curve [81].

Hot workability is a significant characteristic that can be assessed by observing changes in strain, strain rate and temperature. So, in this study, the flow stress curves of M50 steel were determined based on a function of temperature, strain and strain rate and the Hänsel-Spittel constitutive equation which describes the deformation behaviour of M50 steel was prepared.

In order to explore M50 steel behaviour under hot deformation, it is necessary to formulate constitutive equations that can simulate the progression of the hot forging procedure. Forge 3.2® software is employed for the purpose of replicating large-scale metal shaping processes, predominantly relying on thermo-viscoplastic constitutive models designed for high-temperature scenarios. So, the Hänsel-Spittel model, commonly employed in bulk forming processes, relies on a straightforward relationship among three fundamental factors: strain, strain rate, and temperature [45]. The developed model [44] by Hänsel-Spittel is given as follows:

$$\sigma = A e^{m_1 T} \varepsilon^{m_2} \dot{\varepsilon}^{m_3} e^{m_4/\varepsilon} (1 + \varepsilon)^{m_5 T} e^{m_7 \varepsilon} \dot{\varepsilon}^{m_8 T} T^{m_9} \quad (10)$$

Here,  $\sigma$  represents the equivalent stress,  $e$  is the natural constant,  $T$  is the deformation temperature ( $^{\circ}\text{C}$ ),  $\varepsilon$  is the strain and  $\dot{\varepsilon}$  is the strain rate. The material coefficients  $A$ ,  $m_1$ ,  $m_2$ ,  $m_3$ ,  $m_4$ ,  $m_5$ ,  $m_7$ ,  $m_8$ , and  $m_9$  describe the material's sensitivity to temperature, strain, and strain rate. The material constants of the Hänsel-Spittel model, derived from the corrected experimental stress-strain curves obtained from the hot compression tests on the Gleeble 3800, are detailed in Table 3.3.

Table 3.3 Parameters of the Hänsel-Spittel Equation

$A$	$m_1$	$m_2$	$m_3$	$m_4$	$m_5$	$m_6$	$m_7$	$m_8$	$m_9$
5387.669	-0.00345	-0.12852	0.138207	-0.0192	0	0	0	0	0

The obtained constants (Table 3.3) were subsequently utilized in the Equation (10) across different combinations of strain, strain rate, and temperature to determine stress values. Figure 3.10 to Figure 3.12 illustrates the comparison between the

corrected curves obtained from Gleeble hot compression tests and those calculated using the Hänsel-Spittel (HS) constitutive equations.

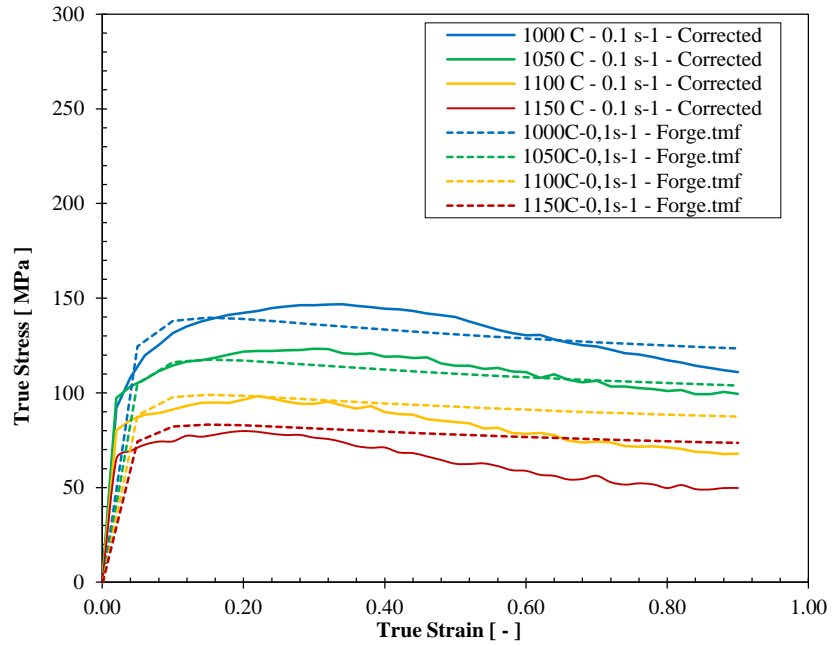


Figure 3.10. Corrected and HS calculated flow curves at  $0.1 \text{ s}^{-1}$

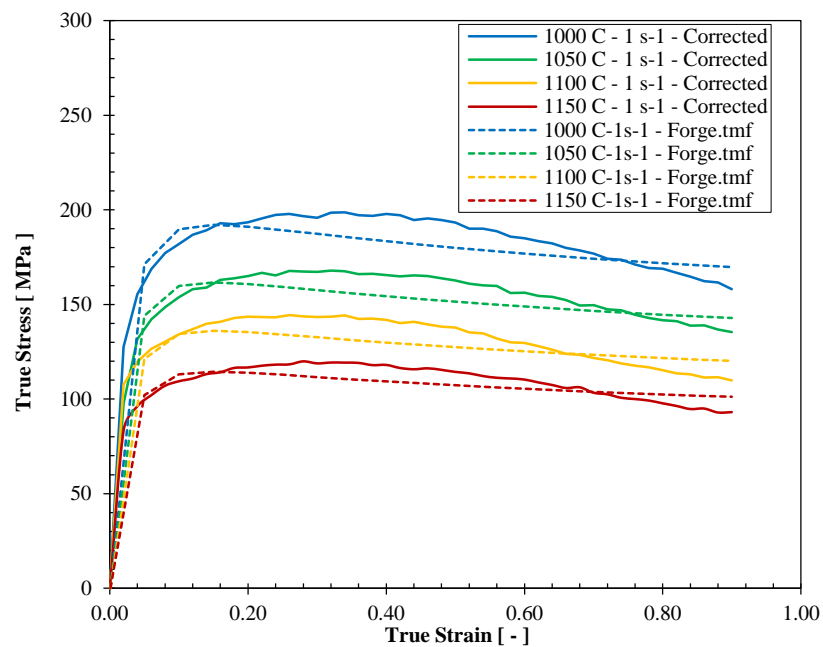


Figure 3.11. Corrected and HS calculated flow curves at  $1 \text{ s}^{-1}$

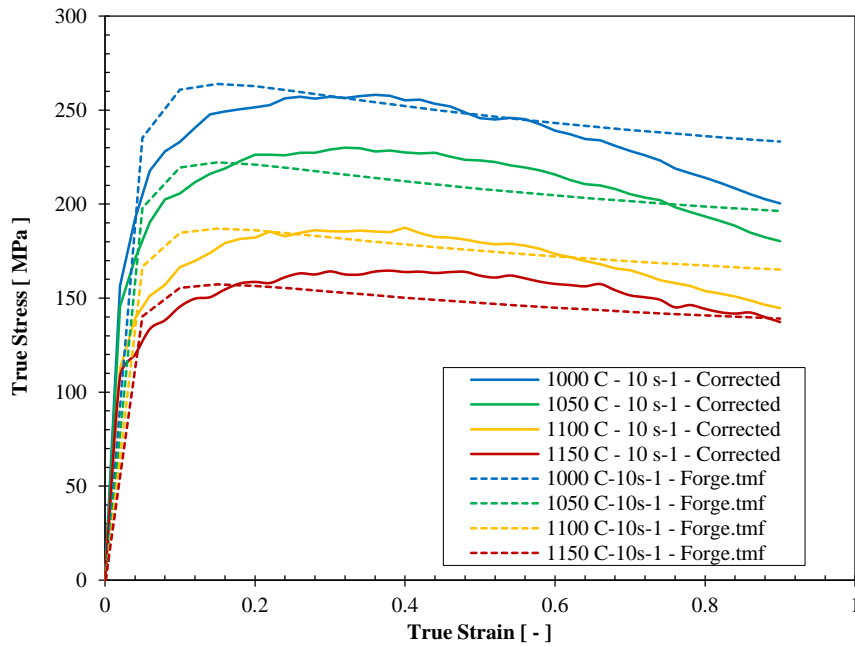


Figure 3.12. Corrected and HS calculated flow curves at  $10 \text{ s}^{-1}$

Using these material constants in Equation (10) results in calculated flow stress curves for different values of strain, strain rate, and temperature. The calculated stress-strain curves from the Hänsel-Spittel equation were then compared to the experimental flow stress curves, demonstrating that the developed model accurately predicts the material behavior at each strain rate. Before commencing the simulation studies, this observation validates the accuracy of the material data card information. Thus, the accuracy of the material data card prepared for M50 steel in Forge 3.2® was confirmed.

### 3.4 Parameter Identification for the Damage Criterion

Hot ductility refers to the ability of a metal or alloy to undergo plastic deformation without fracturing or cracking when it is subjected to elevated temperatures. This property is particularly relevant in high-temperature processing and forming operations. So, determining ductile fracture is crucial for the hot forging process as it defines M50's capacity for plastic deformation without cracking. In this study, the

normalized Latham-Cockroft ( $LC_n$ ) criterion was utilized to predict damage in a multi-stage hot forging process for M50 steel, which consists of four stages: upsetting, closed-die forging, and two stages of shearing to separate the rings and remove the scrap from the inner ring.

As explained in “2.2.1.2 Damage Prediction with Ductile Damage Criteria”, according to the Latham-Cockroft criterion, a fracture occurs when the tensile strain energy accumulation reaches a specific critical threshold (C). This threshold is a constant experimentally determined for each material, temperature, and strain rate. The criterion evaluates the overall tensile plastic work during the metalworking process, capturing microstructural damage such as the formation, growth, and coalescence of microvoids caused by tensile stresses and plastic deformation. Damage occurs when this critical value, C, is achieved [66]. So, this value was essential for creating a model that enables the analysis of ductile fracture in numerical simulations. In several studies [66,69,82], tensile tests were employed to examine the ductile fracture behaviour of materials.

Furthermore, as mentioned in the first paragraph of this section, two stages of shearing in the multi-stage hot forging process—separating the rings and removing the scrap from the inner ring—require precise and smooth cut surfaces. In this context, upon reviewing the literature, the shearing operation is described as being similar to the shear-punch test procedure, in which a flat solid punch shears material through a die at a constant speed. Several researchers [83-86] have observed a direct correlation between the shear-punch test data and tensile data. Additionally, the load-displacement curve observed during the shearing operation exhibits notable resemblances to tensile test curves, encompassing initial linear elastic and plastic deformation regions, a yield point, and an ultimate load [87].

Based on the provided references, experimental hot tensile tests were initially conducted in this thesis study to establish the  $LC_n$  criterion. Subsequently, the experimental studies were numerically simulated using finite element analysis.

### 3.4.1 Experimental Hot Tensile Tests

As mentioned in 3.2. Material Characterization w/ Experimental Methods, the Gleeble system employs a direct resistance heating mechanism. The Gleeble 3800 can heat specimens at rates exceeding  $10.000^{\circ}\text{C}/\text{sec}$  and maintain steady-state equilibrium temperatures within  $\pm 1^{\circ}\text{C}$ . To effectively control the heating and cooling rates, Dynamic Systems Inc., which designs and manufactures Gleeble, offers options for sample sizes that facilitate smooth regulation of the thermal system [73]. Therefore, the dimensions of the tensile test specimens presented in Figure 3.13 were prepared according to the technical drawings developed in accordance with the specifications of the Gleeble system. The tensile test specimens were prepared according to the technical drawing provided below in Figure 3.13.

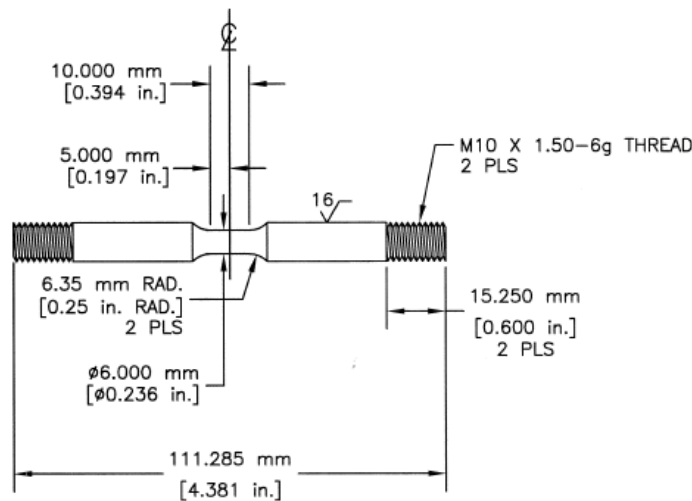


Figure 3.13. Tensile test specimens of M50 for the Gleeble 3800

Within the context of the M50 material characterization, utilizing the JMatPro program as outlined in the first part of this study, titled 3.1. Material Characterization w/ Computational Methods, it was established that flow instability occurred at high speeds below  $1000^{\circ}\text{C}$  and that the temperature should not exceed  $1200^{\circ}\text{C}$  to avoid any local melting. Therefore, the experimental compression test temperatures for

material characterization were set at 1000°C, 1050°C, 1100°C, and 1150°C, with tests conducted at three varying strain rates to develop the constitutive model.

The purpose of conducting the tensile test is to experimentally determine the specific threshold (C) value for the normalized Latham-Cockcroft damage criterion. The determined “C” value will be used in hot forging simulations, necessitating the establishment of a threshold value through tensile tests, particularly during the shearing process resulting from three following stages. Thus, the hot tensile test temperatures were determined, taking into account the experimental conditions of the hot forging process.

Based on the temperatures to be used in the field studies, the hot tensile test temperatures were determined within the expected temperature range during the shearing stage. On the forging machine where the trials took place (as described in the upcoming Chapter 5), the temperature read by the pyrometer had a tolerance of  $\pm 25^\circ\text{C}$ . Therefore, considering this tolerance under experimental conditions, working at 1000°C during the shearing stage would pose a risk of flow instability for the machine's equipment.

As a result, the hot tensile tests were conducted starting from a minimum of 1050°C instead of 1000°C, carried out at 50°C intervals of 1050°C, 1100°C, 1150°C, and 1200°C, with a strain rate of  $10\text{ s}^{-1}$ , and two specimens were prepared for each temperature in the Gleeble system, as shown in Figure 3.14. The specimens were heated using high-frequency induction at a rate of  $10\text{ }^\circ\text{C/s}$ .

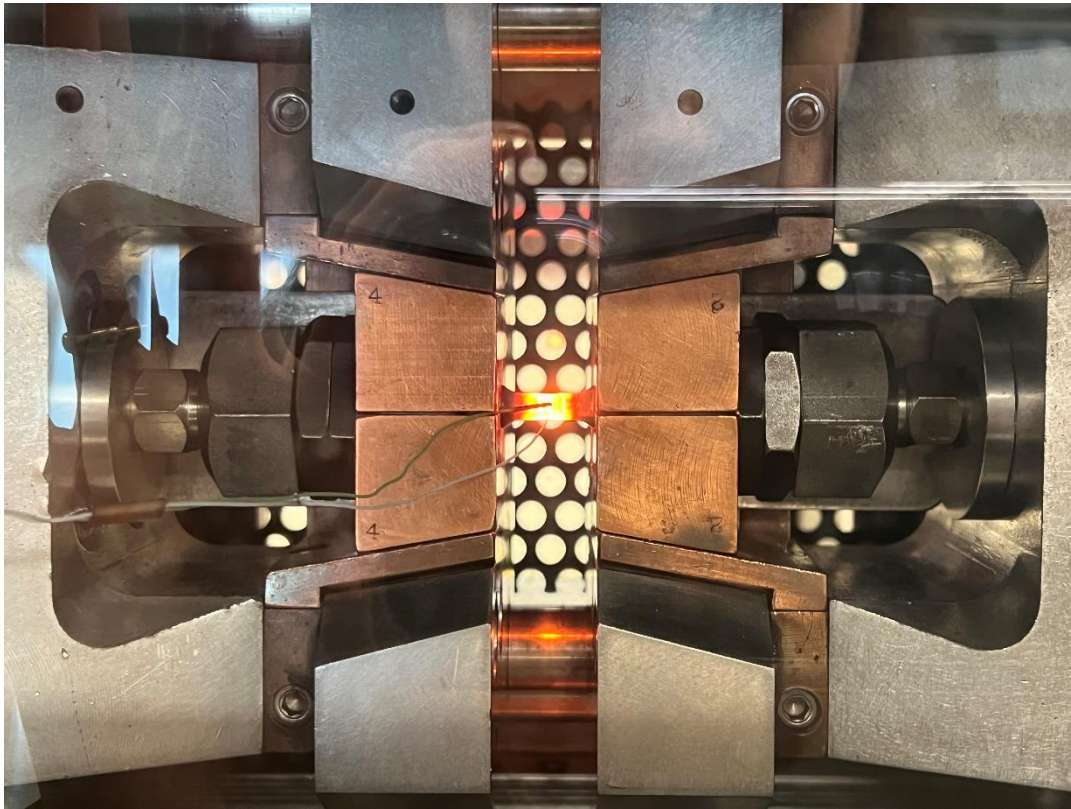


Figure 3.14. Hot tensile tests in Gleeble system

Engineering stress-strain diagrams derived from experimental hot tensile tests at temperatures of 1050°C, 1100°C, and 1150°C are presented in between Figure 3.15 and Figure 3.17. During the tensile tests at 1200°C, the specimens began to melt, preventing the acquisition of smooth tensile stress-strain curves. For this reason, the engineering stress-strain curve at this temperature is not given below.



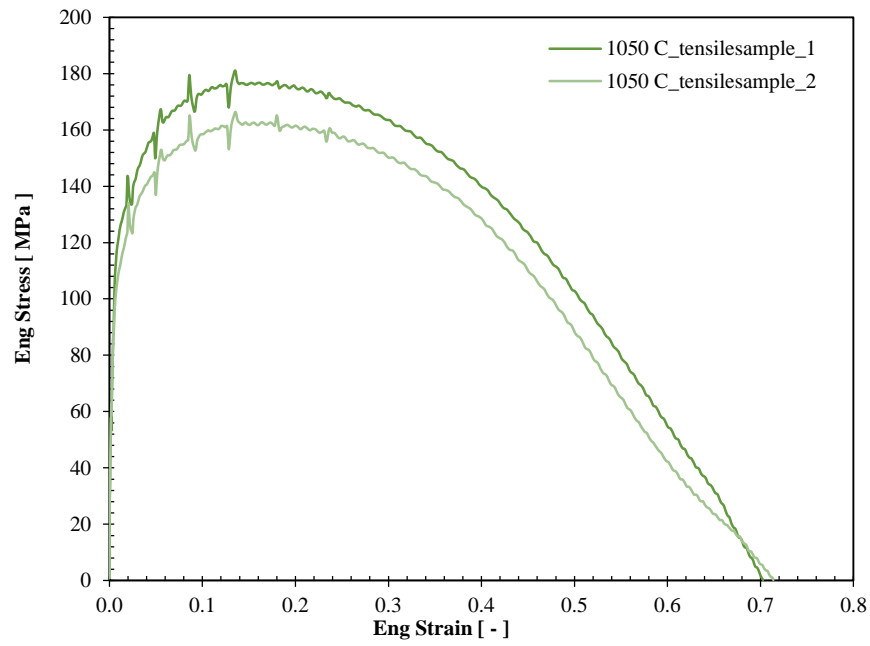


Figure 3.15. The experimental engineering stress-strain curve at 1050°C

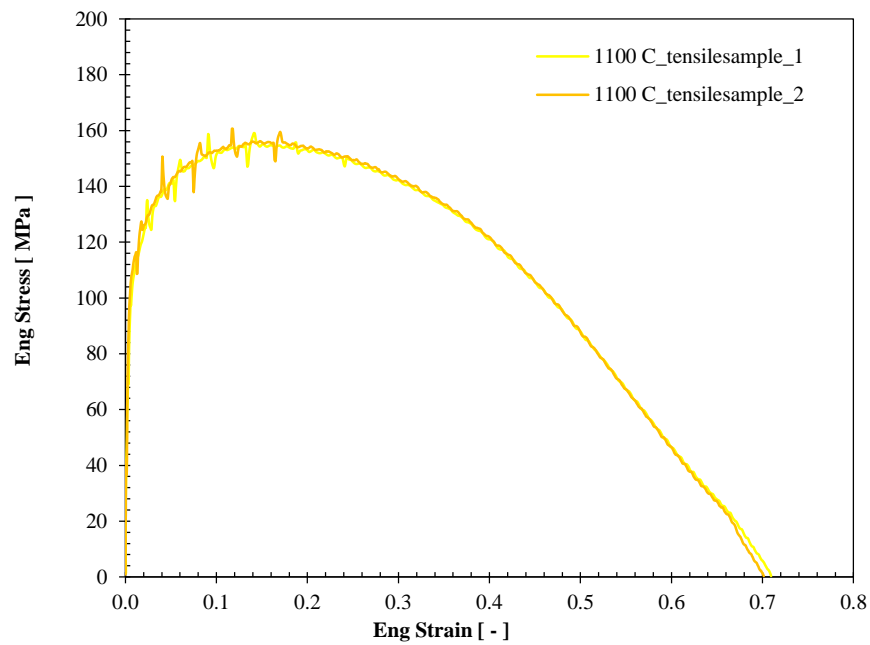


Figure 3.16. The experimental engineering stress-strain curve at 1100°C

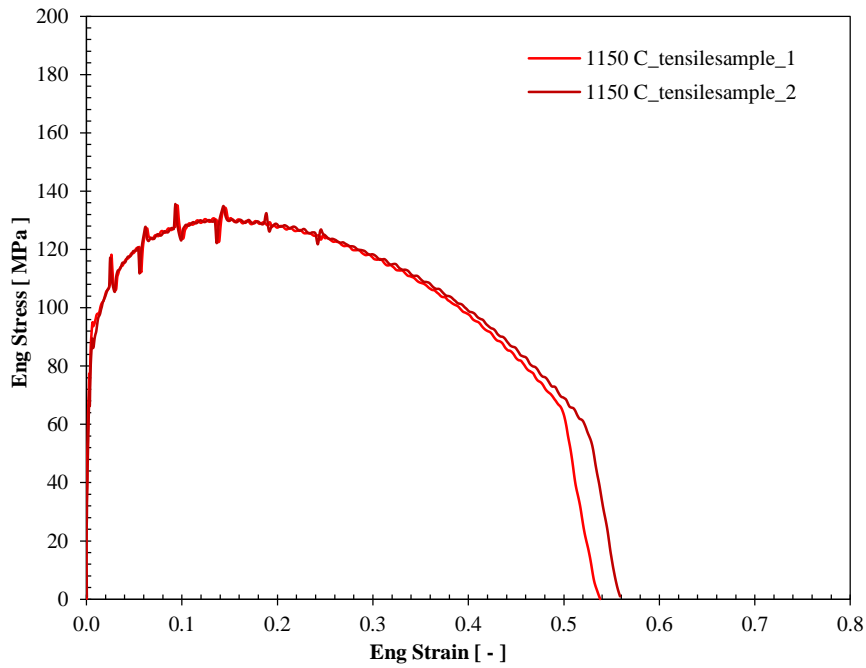


Figure 3.17. The experimental engineering stress-strain curve at 1150°C

After completing the hot tensile tests, the hot ductility behaviour was evaluated in terms of reduction of area (%) and strain (%) at fracture for each test temperature. The reduction of area was determined by assessing the diameter in the fractured region of the specimen after testing, with the measurements presented in Table 3.4.

Table 3.4 Measurements of Hot Tensile Test Samples' Diameters

Temperature (°C)	Repetition	Initial Area (mm <sup>2</sup> )	Final Area (mm <sup>2</sup> )	Initial Diameter (mm)	Final Diameter (mm)
1050	1	28.09	2.69	5.98	1.85
	2	27.99	2.01	5.97	1.60
1100	1	28.09	2.69	5.98	1.85
	2	27.90	2.54	5.96	1.80
1150	1	27.90	8.55	5.96	3.30
	2	28.18	8.04	5.99	3.20
1200	1	28.09	28.09	5.98	5.98
	2	27.81	27.81	5.95	5.95

Figure 3.18 and Figure 3.19 display reduction of area (%) and strain (%) at fracture for each hot tensile testing temperature.

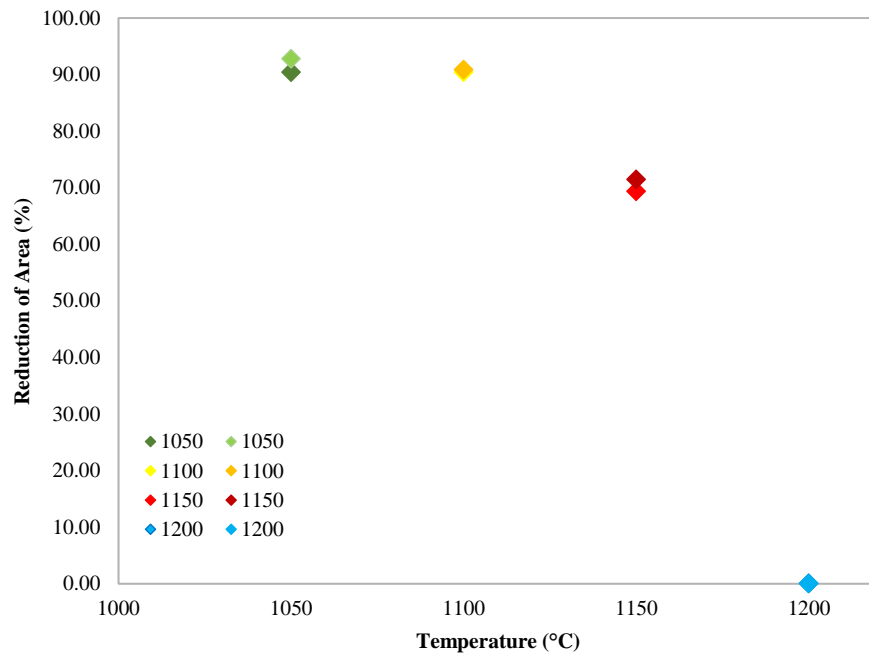


Figure 3.18. Reduction of area (%) vs temperature (°C)

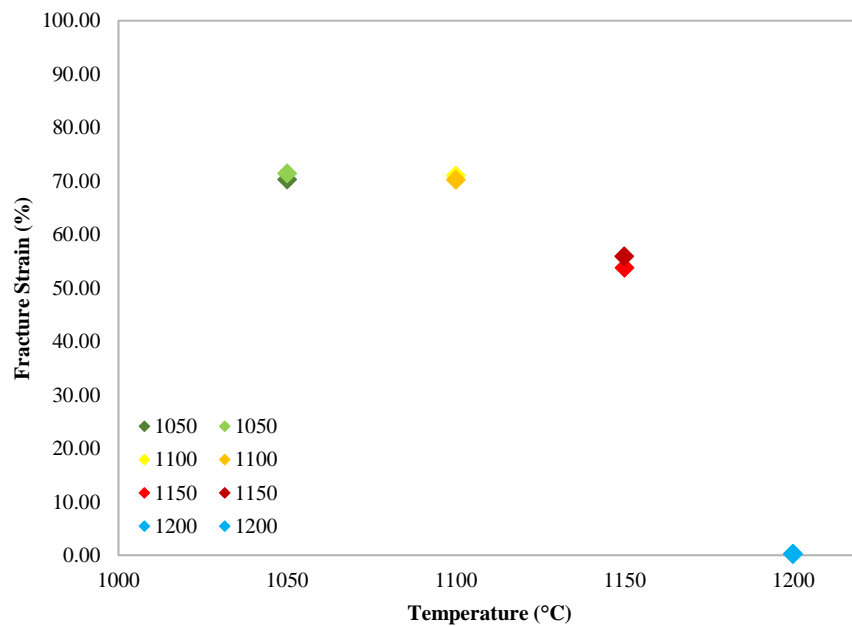


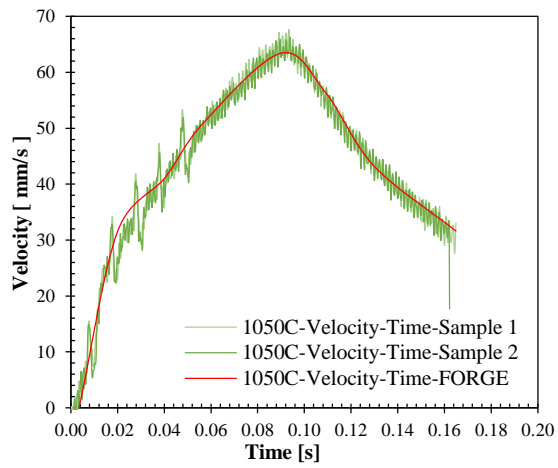
Figure 3.19. Fracture strain (%) vs temperature (°C)

Upon analyzing Figure 3.18 and Figure 3.19, decreases in the reduction of area from approximately 90% to about 70% and in the fracture strains from 70% to roughly 55% were observed with increasing temperatures up to 1150°C. Therefore, it is evident that plasticity under tensile loading reduces for M50 steel after 1150°C at the conclusion of the experimental hot tensile tests.

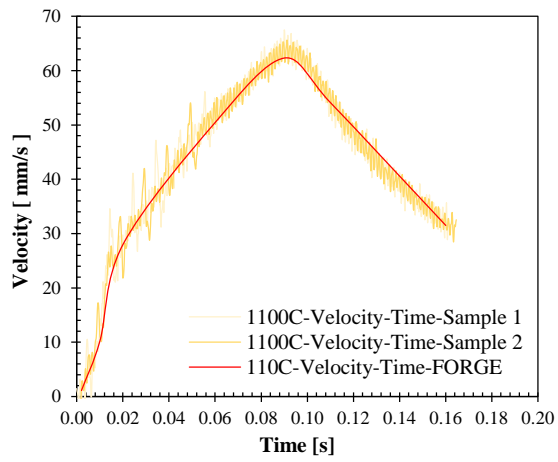
### **3.4.2 Numerical Hot Tensile Tests**

Following the experimental tests, numerical modeling was performed. In order to obtain reliable numerical results, the velocity-time curves from the experimental tensile tests were utilized as inputs for the 2D test simulations, which were conducted using Forge NxT 3.2® software.

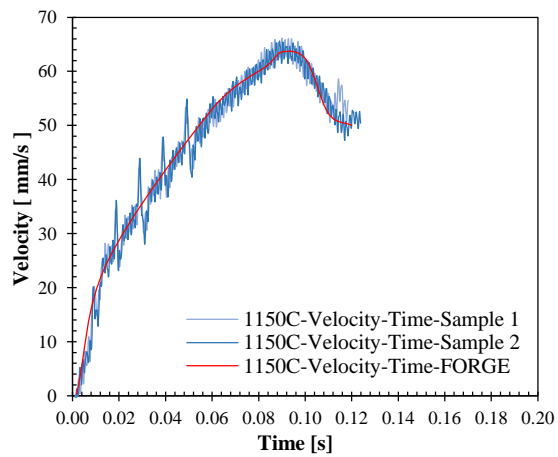
During the tensile tests at 1200°C, the specimens began to melt, which prevented the acquisition of smooth tensile stress-strain curves. Consequently, a tensile test simulation at this temperature was not conducted. The velocity-time curves used for the numerical analysis at the other three temperatures are shown below in Figure 3.20.



(a) Tensile test at 1050°C



(b) Tensile test at 1100°C



(c) Tensile test at 1150°C

Figure 3.20. Velocity-time curves (a-b-c) of tensile tests

To determine the triggering value for the Latham-Cockcroft normalized ( $LC_n$ ) damage criterion, the tensile test specimen was modeled with only the gauge length (10 mm) as a two-dimensional axisymmetric structure, using a mesh size of 0.05 mm, as shown in Figure 3.21.

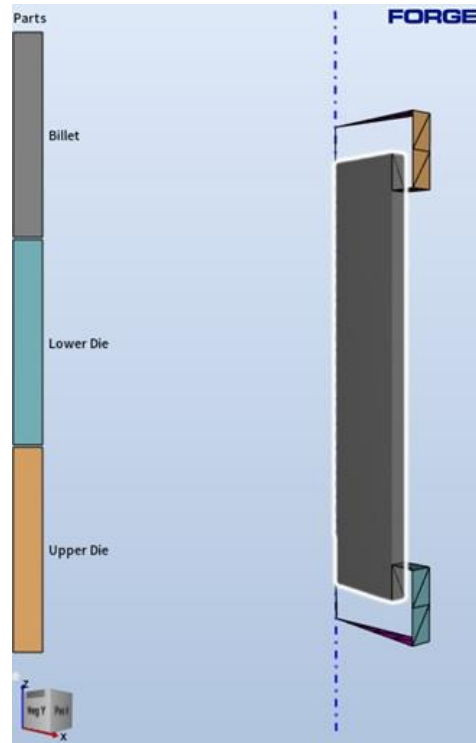
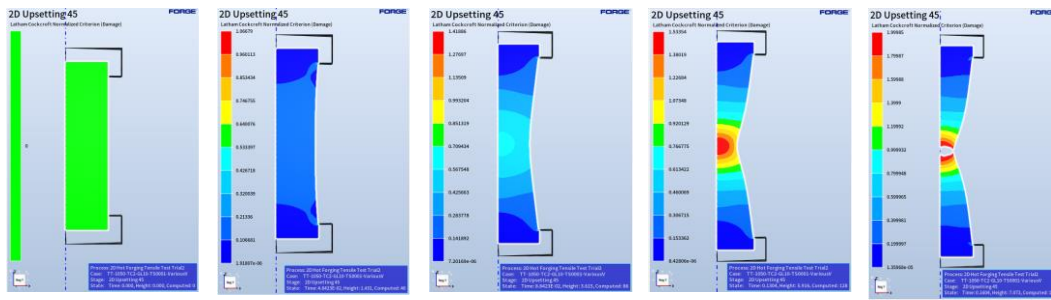


Figure 3.21. Gauge length modeling for the 2D test simulations in Forge NxT 3.2®

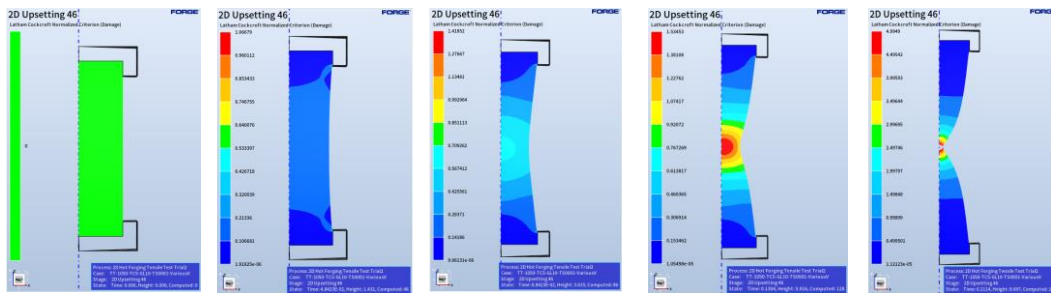
The simulation assumed adiabatic heat transfer between the part and the surrounding environment to replicate the conditions of the experimental hot tensile test. During the simulation of these tests using empirical velocity-time profiles, the upper die operated at specified velocities while the lower die remains stationary. Besides, bilateral sticking was chosen as the friction between the test sample and dies, causing the upper die and the test sample to move together. Afterward, engineering stress-strain diagrams were generated from load-displacement curves in numerical tensile

tests employing various damage criteria at temperatures of 1050°C, 1100°C, and 1150°C. Subsequently, the fracture strain values were evaluated through experimental tests and numerical simulations using different normalized Latham-Cockcroft criterion ( $LC_n$ ) values.

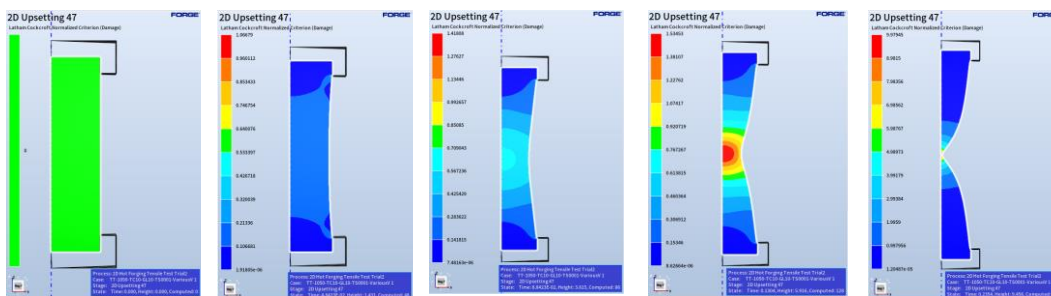
The engineering stress-strain curves from experimental hot tensile tests at 1050°C, 1100°C and 1150°C were compared with those generated by FEA simulations using different  $LC_n$  values. Specifically,  $LC_n$  values of 1, 2, 3, 5, and 10 were tested for the temperatures of 1050°C, 1100°C, and 1150°C. By adjusting the  $LC_n$  values (1, 2, 3, 5, 10) and overlaying the engineering stress-strain curves from the experimental hot tensile tests with those from the FEA simulations, the  $LC_n$  parameter that closely matched the experimental curves was chosen as the ductile damage criterion (the threshold) for each temperature. Figure 3.22 presents images illustrating how fracture varies with different  $LC_n$  values at 1050°C.



a) Hot tensile tests at 1050°C with  $LC_n=2$



b) Hot tensile tests at 1050°C with  $LC_n=5$



c) Hot tensile tests at 1050°C with  $LC_n=10$

Figure 3.22. FEM results of the tensile tests at 1050°C with  $LC_n=2, 5$  and 10

By adjusting the  $LC_n$  value for 1050°C, the fracture strain results obtained by comparing the experimental engineering stress-strain curves with the numerical ones are presented in Figure 3.23. Similarly, for 1100°C, the results are shown in Figure 3.24, and for 1150°C, they are provided in Figure 3.25.



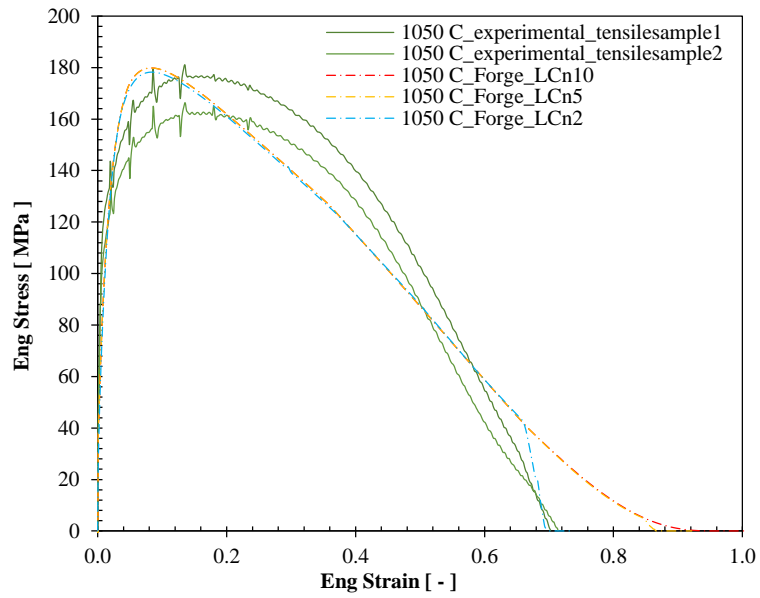


Figure 3.23. Comparison of experimental and calculated flow stresses at 1050°C

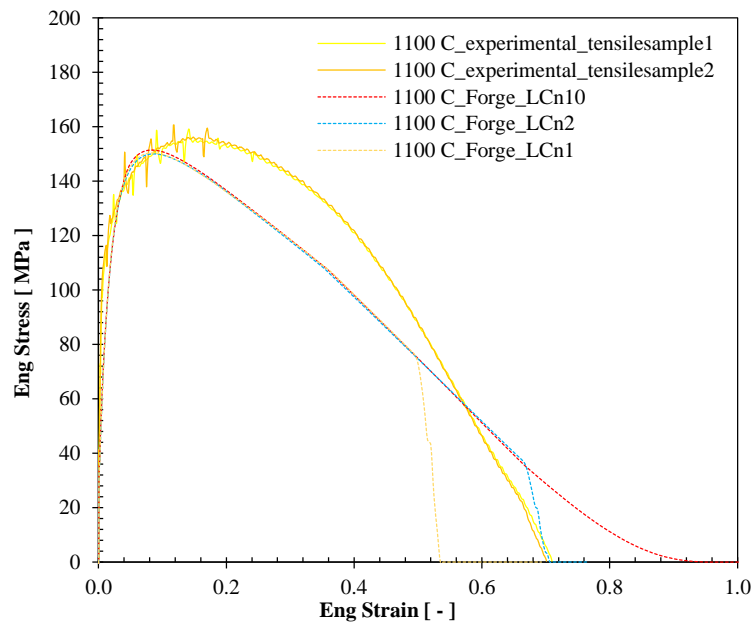


Figure 3.24. Comparison of experimental and calculated flow stresses at 1100°C

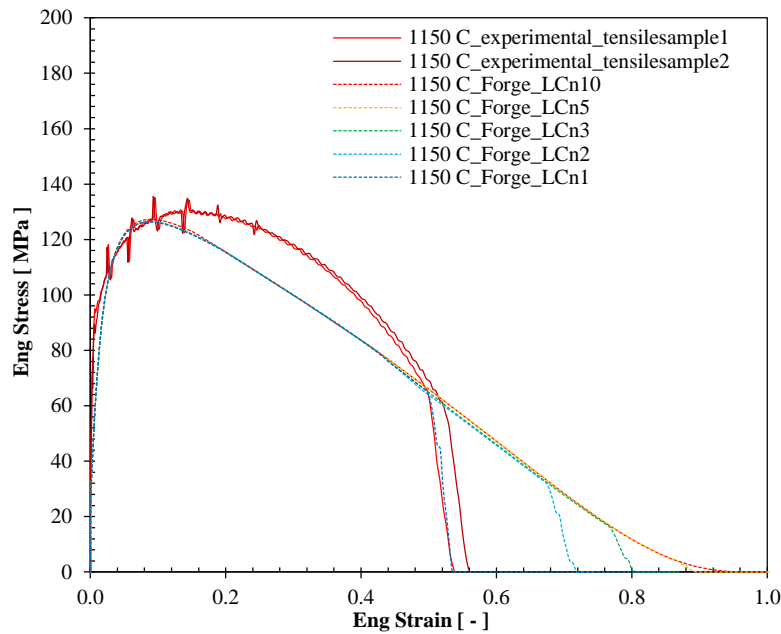


Figure 3.25. Comparison of experimental and calculated flow stresses at 1150°C

As illustrated in Figure 3.23 and Figure 3.24, the experimental and simulation engineering stress-strain curves matched when  $LC_n=2$  was used for tests at 1050°C and 1100°C. However, at 1150°C,  $LC_n=2$  did not coincide with the experimental data, as the fracture point was farther from the experimental data. Therefore, by decreasing the  $LC_n$  value to “1”, the curves overlapped accurately, as shown in Figure 3.25. As a result, this analysis revealed that damage criteria vary with temperature, showing that the  $LC_n$  damage criterion is a temperature-dependent material property. Consequently, the  $LC_n$  value of “2” was selected for temperatures up to 1150°C, while a value of “1” was chosen for higher temperatures.

### 3.5 Summary and Conclusions

At the conclusion of this chapter, a comprehensive dataset for M50 steel was generated, and corresponding flow curves were established through the execution of hot compression tests on the Gleeble 3800 at four discrete temperatures (1000°C, 1050°C, 1100°C, and 1150°C), and three different strain rates ( $0.1 \text{ s}^{-1}$ ,  $1 \text{ s}^{-1}$ ,  $10 \text{ s}^{-1}$ ).

Subsequently, the Hänsel-Spittel model parameters were derived from the corrected experimental stress-strain curves obtained from the hot compression tests in order to investigate the hot deformation behaviour of M50 steel. Comparison between stress-strain curves calculated using the Hänsel-Spittel equation and experimental flow stress curves demonstrates the model's precise prediction of M50 steel behaviour across varying strain rates.

Additionally, based on the results of experimental hot tensile tests and subsequent simulations, fracture strain values were assessed both experimentally and numerically to determine the threshold value for the Latham-Cockcroft normalized criterion. To establish the threshold value of the normalized Latham-Cockcroft criterion ( $LC_n$ ), experimental hot tensile tests were conducted at temperatures of 1050°C, 1100°C, 1150°C, and 1200°C.

Upon completion of the experimental hot tensile tests, the hot ductility behaviour was assessed based on the reduction of area (%) and strain (%) at fracture for each test temperature. The analysis revealed a decline in both the reduction of area (%) and the fracture strains (%) as temperatures increased up to 1150°C. Consequently, it is clear that the plasticity of M50 steel under tensile loading decreases beyond 1150°C.

Subsequently, numerical simulations were performed based on these experiments, and fracture strain values were evaluated. The findings from both the experimental tests and simulations indicate that the  $LC_n$  damage criterion is a temperature-dependent material property. Consequently, an  $LC_n$  criterion of “2” was selected for temperatures up to 1150°C, while a criterion of “1” was chosen for temperatures exceeding this threshold.

At the end of this chapter with the obtained results, an important point to consider is that a temperature-dependent criterion is rare in simulations of hot metal forming, and it is believed that this study will demonstrate the first use of such a model in the literature. Therefore, a detailed explanation of the metallurgical reasons behind this behaviour in M50 steel has been left for Chapter 4.



## CHAPTER 4

### MICROSTRUCTURE OBSERVATIONS OF M50 STEEL

At the end of Chapter 3, the  $LC_n$  damage criterion is evaluated as a temperature-dependent material property. Since M50 is a type of high-speed steel characterized by its high content of alloying elements and significant presence of carbides [9], this behaviour of the damage criterion is believed to be associated with the presence of primary carbides in M50 steel. Therefore, the microstructural evolution of the thermal deformation behaviour of M50 steel are important for this thesis study.

In this context, the as-received microstructures of M50 were initially examined. Following this, additional hot tensile tests were conducted to observe the microstructural changes at intermediate temperatures, in addition to the hot tensile test data presented in “3.4.1 Experimental Hot Tensile Tests.” As indicated in 3.4.1, the hot tensile tests were completed at 1050°C, 1100°C, and 1150°C. During the tensile tests at 1200°C, the specimens began to melt, which prevented the acquisition of smooth tensile stress-strain curves. Furthermore, hot tensile tests were conducted at intermediate temperatures to evaluate the transition of the microstructure and the microstructural changes of M50 steel under thermal deformation. Accordingly, the temperatures of 1125°C, 1138°C, 1163°C, and 1175°C were selected for these additional hot tensile tests, which were conducted in the Gleeble system at a strain rate of  $10 \text{ s}^{-1}$  and heated at a rate of  $10 \text{ }^\circ\text{C/s}$ .

In this chapter, to provide a detailed explanation of the metallurgical reasons behind the behaviour in M50 steel, both the as-received microstructures and the microstructures observed after tensile testing were examined using optical microscope (OM) and scanning electron microscope (SEM). Therefore, the thermal deformation behaviour of M50 steel was explored after hot tensile test experiments conducted in the Gleeble system.

#### 4.1 Microstructure of As-Received M50 Steel

In order to compare the effects of hot tensile test temperature on the carbides and microstructure, the as-received microstructure of M50 steel was first observed using an optical microscope (OM).

Microstructural examinations of the as-received material were conducted on the surface and cross-section of a slice taken from a 45 mm diameter rod. To provide clarity on the examined surfaces, the relevant cross-sections are shown in Figure 4.1 for illustrative purposes. Accordingly, the rod's cross-section is shown in Figure 4.1 (a), which will be referred to as “surface” in the following part of this chapter. Meanwhile, the cross-section of the slice taken from the rod, which will be referred to as “cross-section”, is shown in Figure 4.1(b).

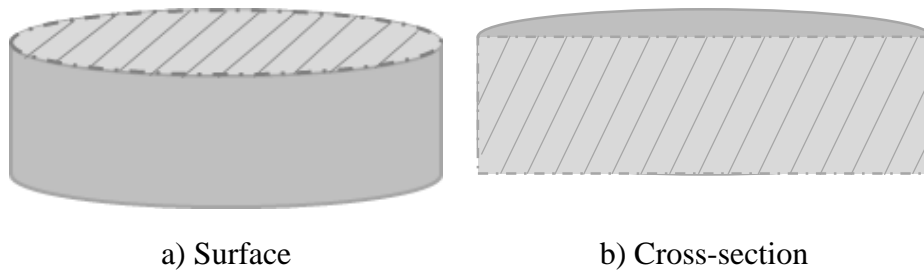


Figure 4.1. Microstructural analysis of the examined sections

Metallographic preparation was done by etching with 3% nital solution. Optical microscope images taken from the surface and cross-section are provided in the Figure 4.2.

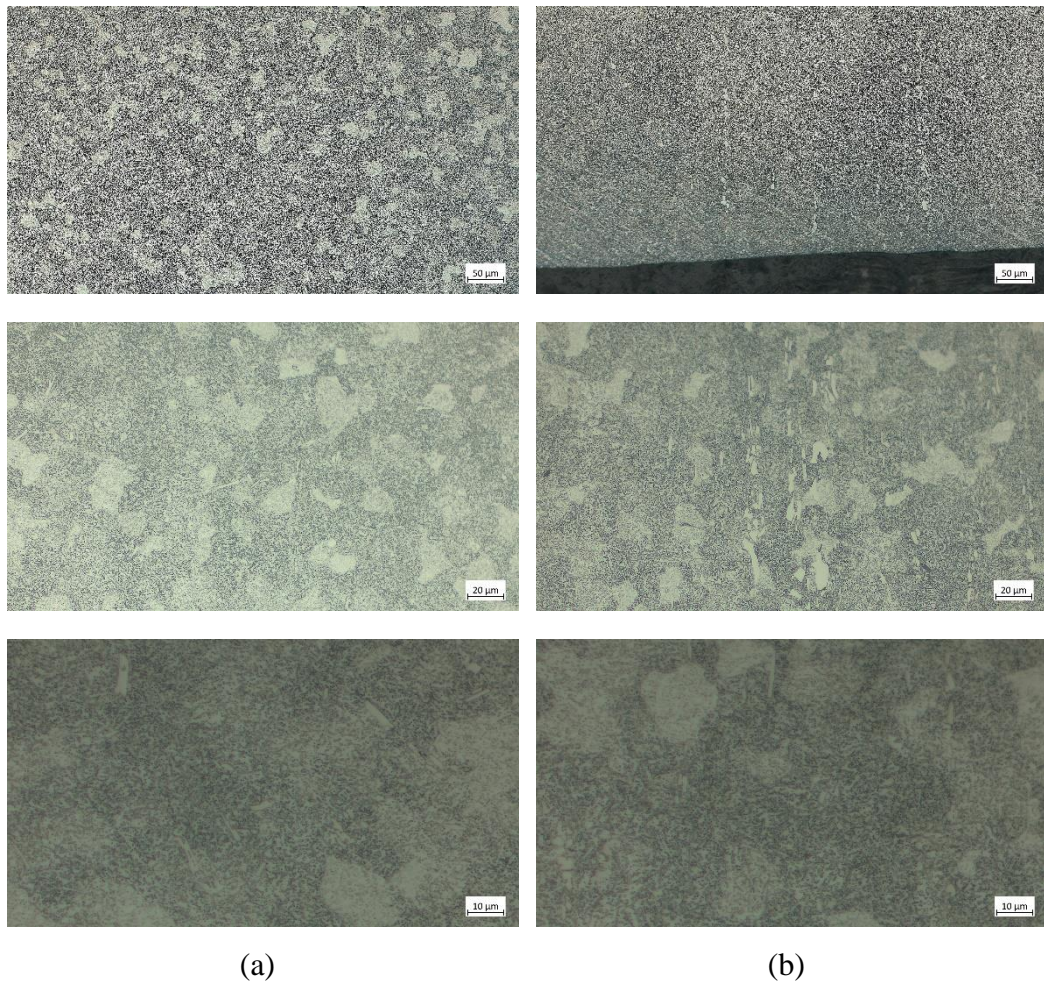


Figure 4.2. OM images of M50 from (a) the surface and (b) cross-section

Subsequently, the same as-received structure was examined using a scanning electron microscope (SEM). Firstly, the cross-section (Figure 4.1 (b)), in other words, the rolling direction of the steel rod, was analyzed under SEM. Additionally, EDS (Energy Dispersive Spectroscopy) was used to map the elemental composition. The areas examined in the cross-section were assessed region by region, as indicated in Figure 4.3, including the center, mid-radius, and surface. SEM examinations were conducted on the cross-section with mapping at 200X magnification, mapping plus chemical analysis with EDS at 500X magnification, and EDS analysis at 10.000X magnification for each of the three regions.

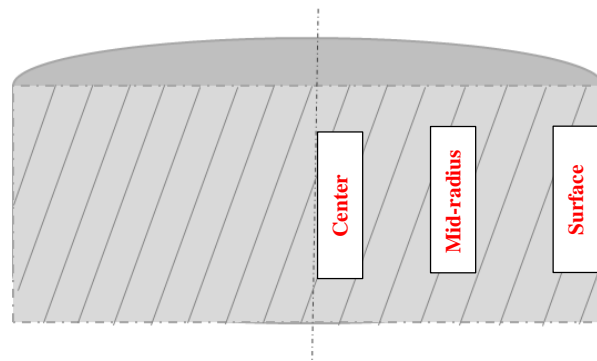


Figure 4.3. Regions analyzed by SEM in the cross-section

Firstly, the center of the cross-section shown in Figure 4.3 was examined. The cross-section center mapping at 200X magnification is provided in Figure 4.4, which includes SEM images of the M50 steel matrix and carbides.

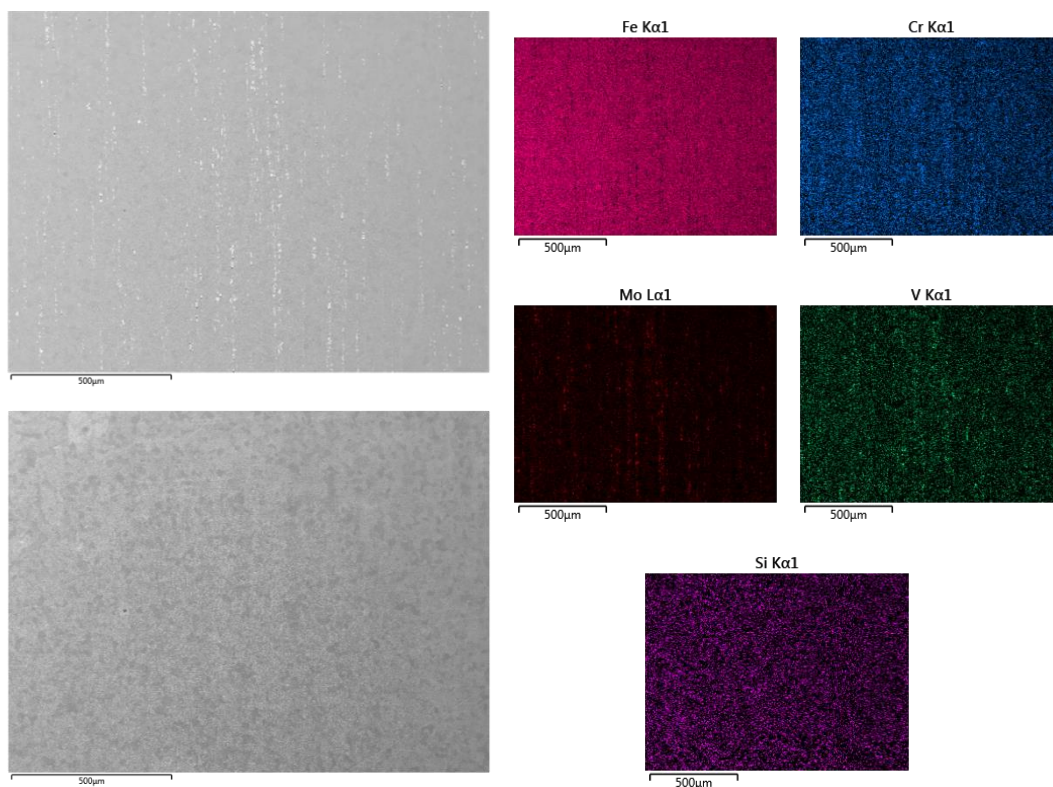


Figure 4.4. Center mapping with SEM at 200X magnification



Subsequently, mapping of the cross-section center was performed at 500X magnification. Additionally, EDS analysis was conducted at different points within the mapped area to examine the elemental composition in terms of weight % of iron (Fe), chromium (Cr), molybdenum (Mo), vanadium (V), and silicon (Si). The cross-section center mapping at 500X magnification is shown in Figure 4.5, while the EDS analysis results from these different points are provided in Figure 4.6.

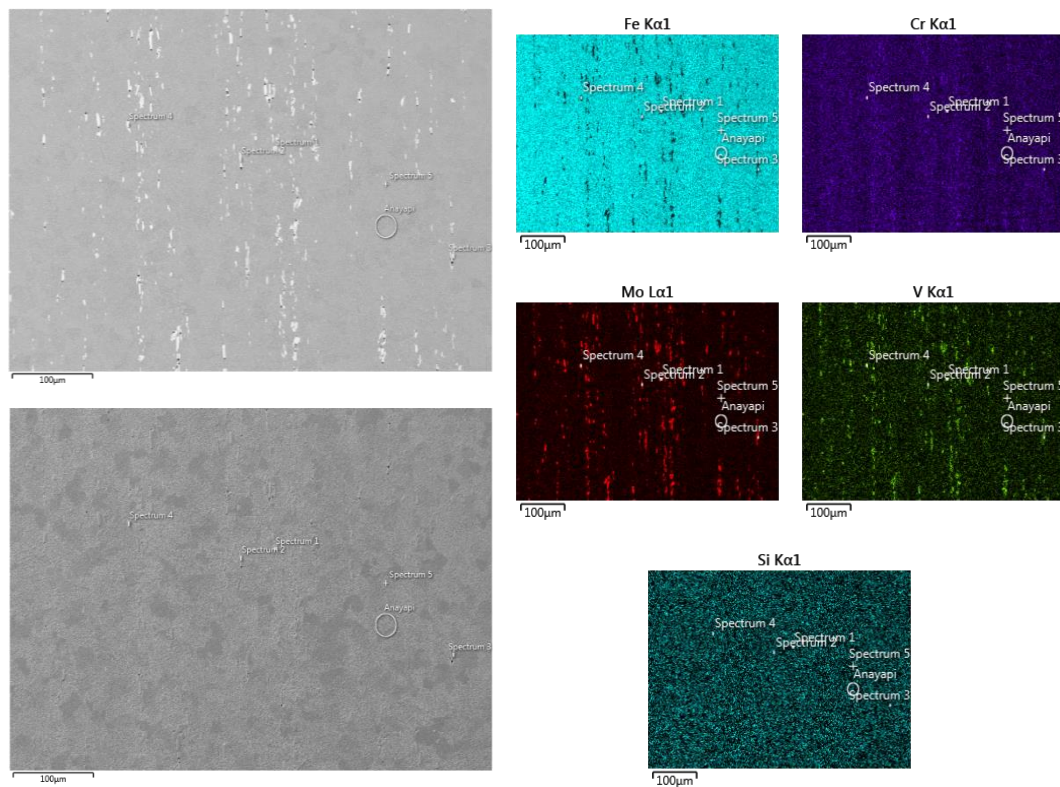


Figure 4.5. Center mapping with SEM at 500X magnification

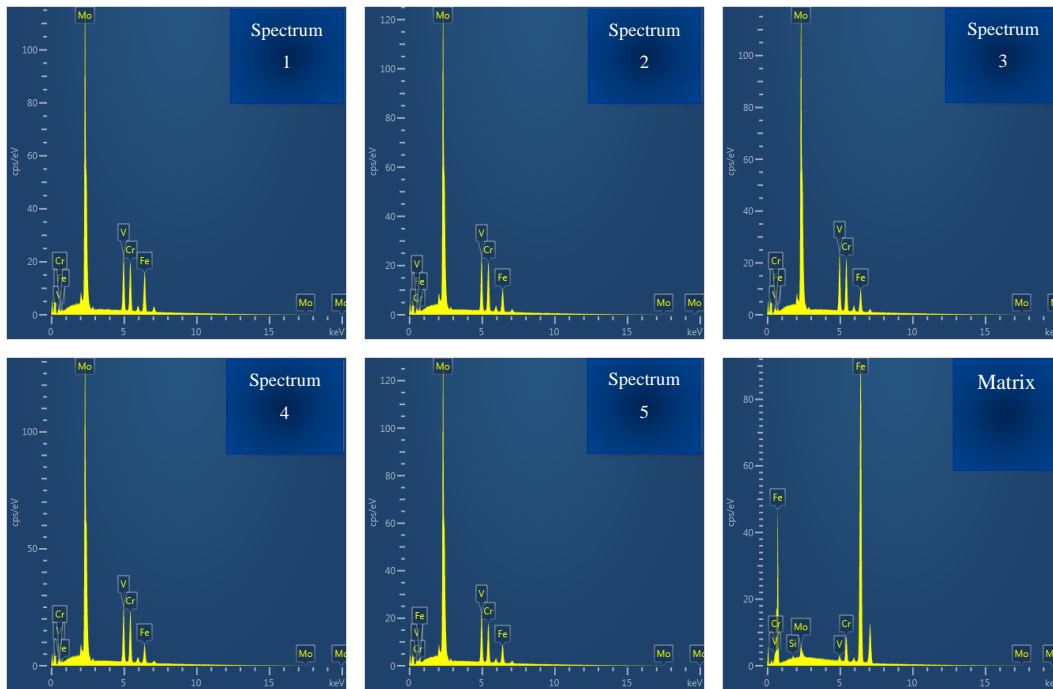


Figure 4.6. EDS analysis results of center mapping with SEM at 500X

The elemental composition of the carbides/matrix, as given in Figure 4.6, is shown in Table 4.1.

Table 4.1 Chemical Composition of the Spectrums Analyzed in Figure 4.5

	Element (wt%)					
	Spectrum 1	Spectrum 2	Spectrum 3	Spectrum 4	Spectrum 5	Matrix
<b>Si</b>	-	-	-	-	-	0.22
<b>V</b>	12.96	13.63	14.38	14.05	13.57	0.82
<b>Cr</b>	11.32	12.24	12.82	13.06	10.31	4.27
<b>Fe</b>	14.92	9.23	8.93	7.48	7.74	92.08
<b>Mo</b>	60.79	64.91	63.87	65.42	68.37	2.62

As it is seen in Figure 4.6 and Table 4.1, EDS analysis of the primary carbides reveals the distribution of Mo, V, Fe and Cr. Following the cross-section center analysis, similar examinations were conducted at the mid-radius and surface regions of the cross-section under SEM at 200X and 500X magnifications. The relevant regions for comparison are shown below in the Figure 4.7.

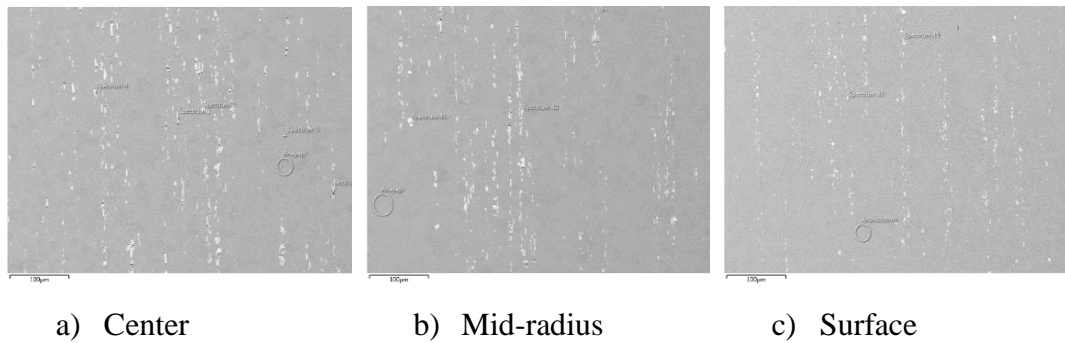


Figure 4.7. Mapping of the cross-section with SEM at 500X magnification

Upon examining the midradius and surface regions of the as-received M50, it was observed that banding was less frequent compared to the center region. The reason for the more intense banding observed at the center is due to the surface region being more deformed during the rod formation of the M50 bar, causing the banding to disappear, while the center region remains less affected. Additionally, when the mapping results of the center, midpoint, and surface regions were examined, Mo bands were observed to be much clearer, and the Si element was uniformly distributed, similar to the homogeneous distribution observed in Figure 4.5.

For the final analysis taken from the center point, EDS analysis was repeated on the primary carbides at 10.000X magnification. The carbides analyzed are shown in Figure 4.8 below.

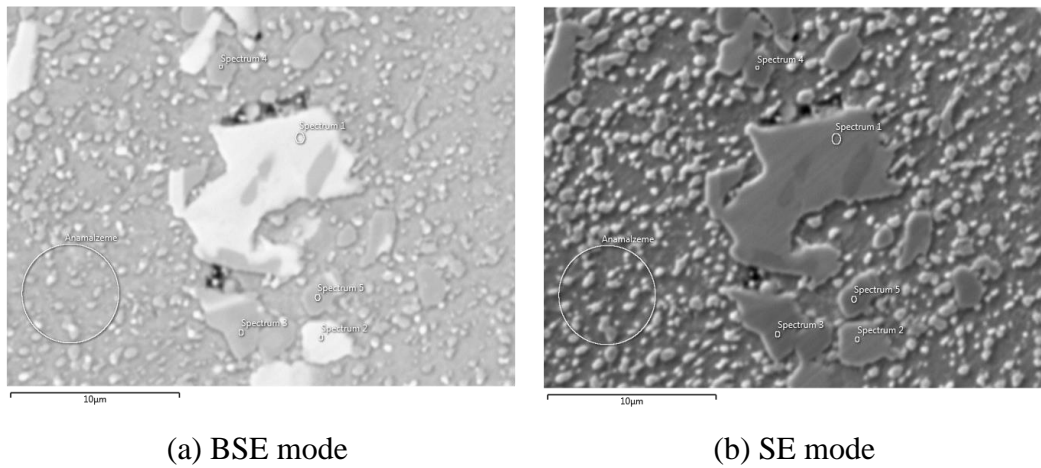


Figure 4.8. SEM images of the M50 steel matrix and primary carbides at 10.000X magnification from the center of the cross-section (a) Back Scattered Electron (BSE) (b) Secondary Electron (SE) imaging modes of SEM

EDS measurements taken from the primary carbides and one measurement taken from the matrix shown in Figure 4.8 are provided in Figure 4.9.

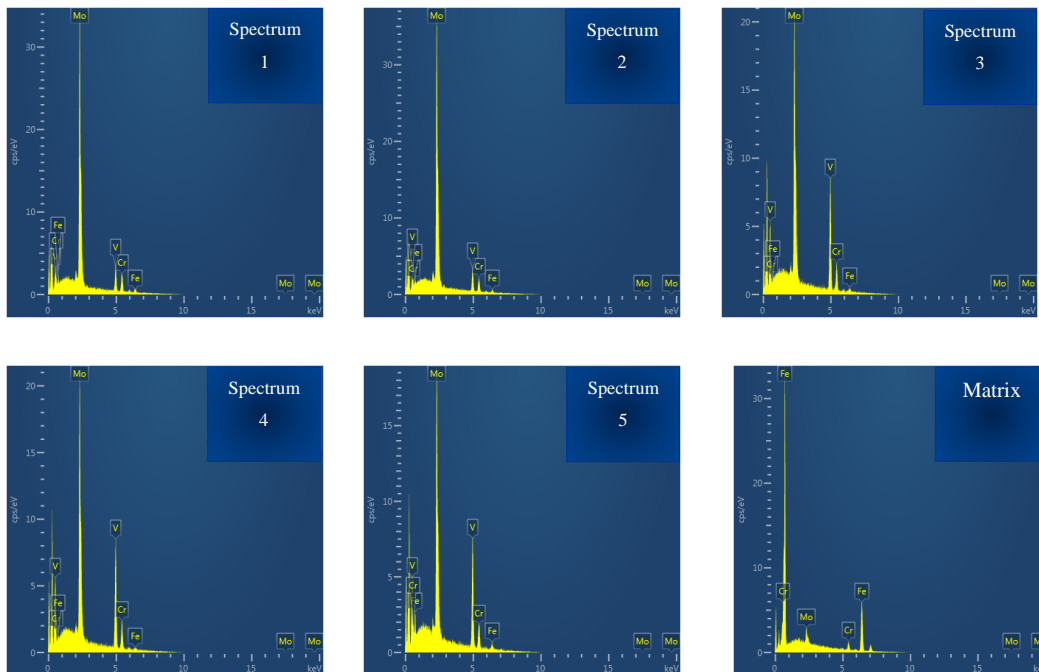


Figure 4.9. EDS analysis results of center with SEM at 10.000X

The elemental composition of the carbides/matrix, as given in Figure 4.9, is shown in Table 4.2.

Table 4.2 Chemical Composition of the Spectrums Analyzed in Figure 4.8

	Element (wt%)					Matrix
	Spectrum 1	Spectrum 2	Spectrum 3	Spectrum 4	Spectrum 5	
<b>V</b>	15.11	14.78	45.37	45.01	43.78	-
<b>Cr</b>	13.06	9.41	7.32	8.1	6.75	5.36
<b>Fe</b>	7.38	5.86	3.95	2.66	6.85	90.75
<b>Mo</b>	64.46	69.95	43.36	44.23	42.62	3.89

Additionally, primary carbide analyses performed for the mid-radius and surface regions of the cross-section at 10.000X magnification, along with the EDS analyses, are provided in Figure 4.10 to Figure 4.13.

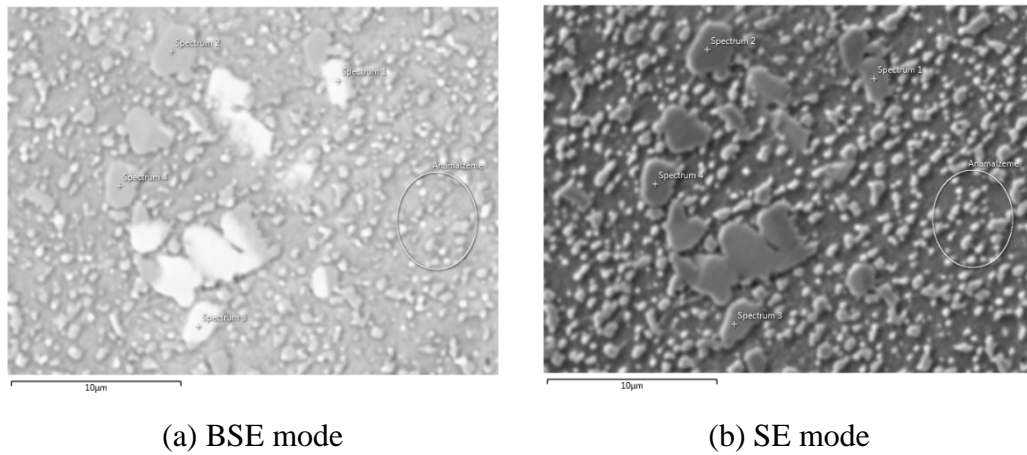


Figure 4.10. SEM images of the M50 steel matrix and primary carbides at 10.000X magnification from the mid-radius of the cross-section (a) Back Scattered Electron (BSE) (b) Secondary Electron (SE) imaging modes of SEM

Figure 4.11 presents EDS measurements obtained from the primary carbides and the matrix, as shown in Figure 4.10, with their elemental composition detailed in Table 4.3.

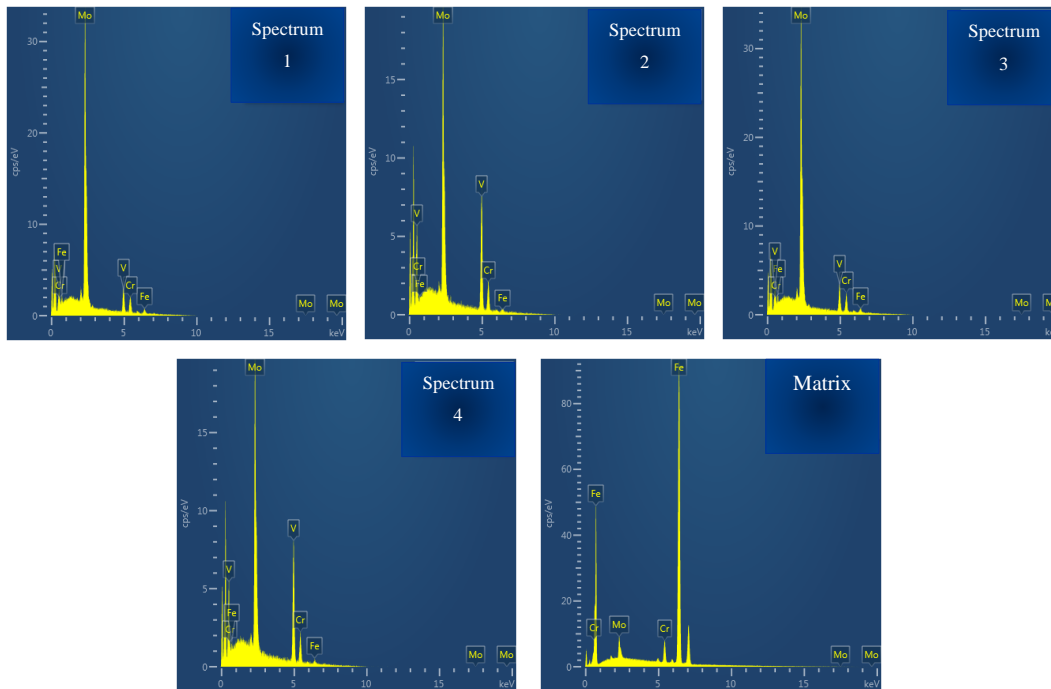


Figure 4.11. EDS analysis results of mid-radius with SEM at 10.000X

Table 4.3 Chemical Composition of the Spectrums Analyzed in Figure 4.10

	Element (wt%)				
	Spectrum 1	Spectrum 2	Spectrum 3	Spectrum 4	Matrix
<b>V</b>	14.09	45.44	15.17	45.07	-
<b>Cr</b>	10.43	7.52	11.29	6.87	3.9
<b>Fe</b>	7.53	3.23	6.57	4.41	91.57
<b>Mo</b>	67.95	43.81	66.98	43.65	4.53

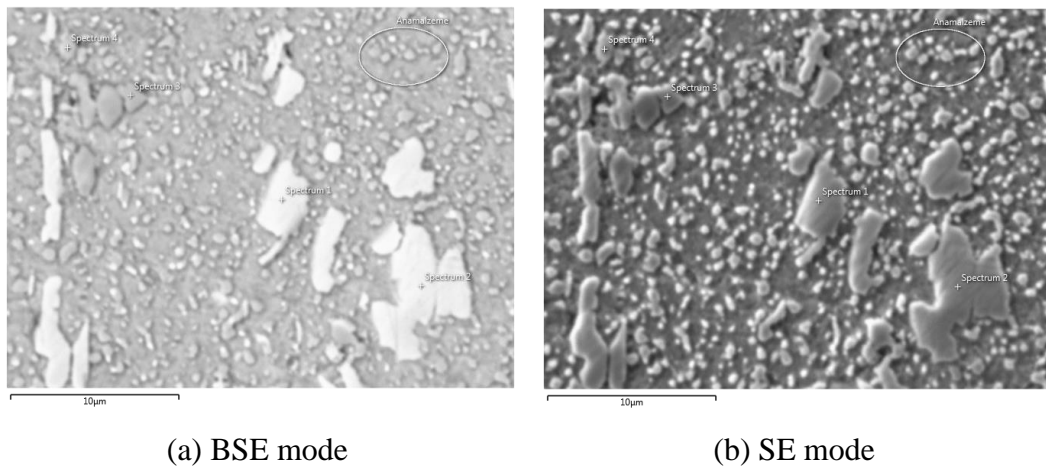


Figure 4.12. SEM images of the M50 steel matrix and primary carbides at 10.000X magnification from the surface of the cross-section (a) Back Scattered Electron (BSE) (b) Secondary Electron (SE) imaging modes of SEM

EDS measurements from the primary carbides and the matrix, depicted in Figure 4.12, are presented in Figure 4.13.

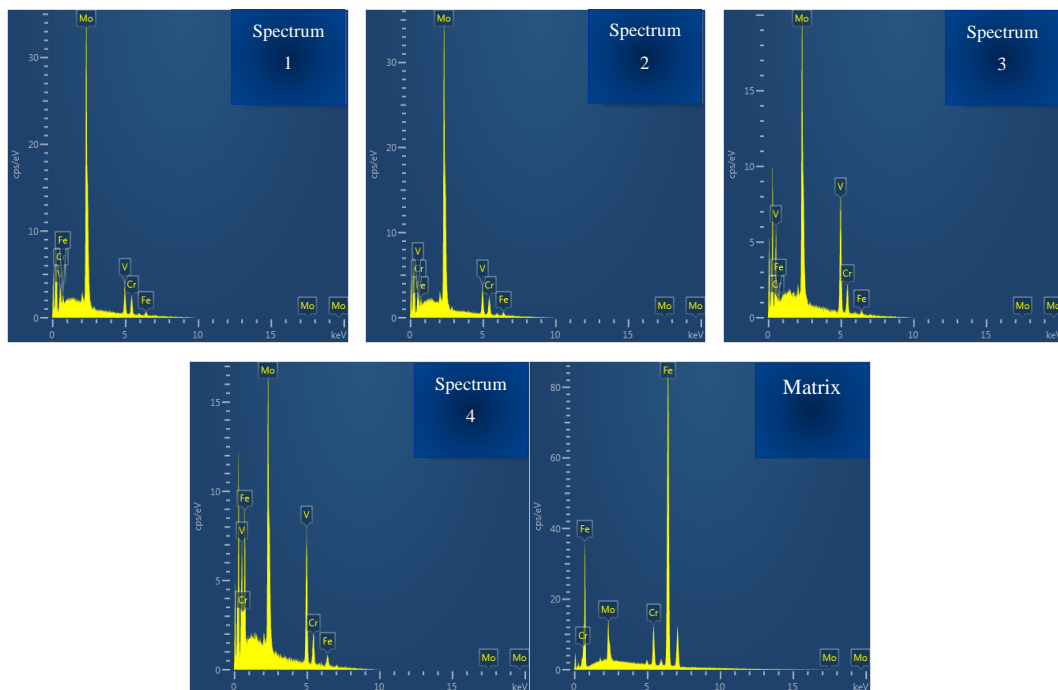


Figure 4.13. EDS analysis results of surface with SEM at 10.000X

The elemental composition of the carbides and matrix, illustrated in Figure 4.13, is summarized in Table 4.4.

Table 4.4 Chemical Composition of the Spectrums Analyzed in Figure 4.12

	<b>Element (wt%)</b>				<b>Matrix</b>
	<b>Spectrum 1</b>	<b>Spectrum 2</b>	<b>Spectrum 3</b>	<b>Spectrum 4</b>	
<b>V</b>	15.15	14.93	44.25	43.17	-
<b>Cr</b>	12.18	11.15	7.67	7.31	6.61
<b>Fe</b>	6.59	6.69	4.34	11.43	85.72
<b>Mo</b>	66.09	67.23	43.74	38.09	7.67

In addition to the SEM examination of the cross-sectional area, as indicated in Figure 4.3, the surface shown in Figure 4.1(a) was also examined. For the surface, SEM examinations were conducted with mapping at 500X magnification and EDS analysis at 10.000X magnification from the mid-radius. Figure 4.14 shows the mapping at 500X magnification, while Figure 4.15 presents the EDS analysis results from various points. Additionally, EDS analysis results of center mapping, as depicted in Figure 4.15, are outlined in Table 4.5.



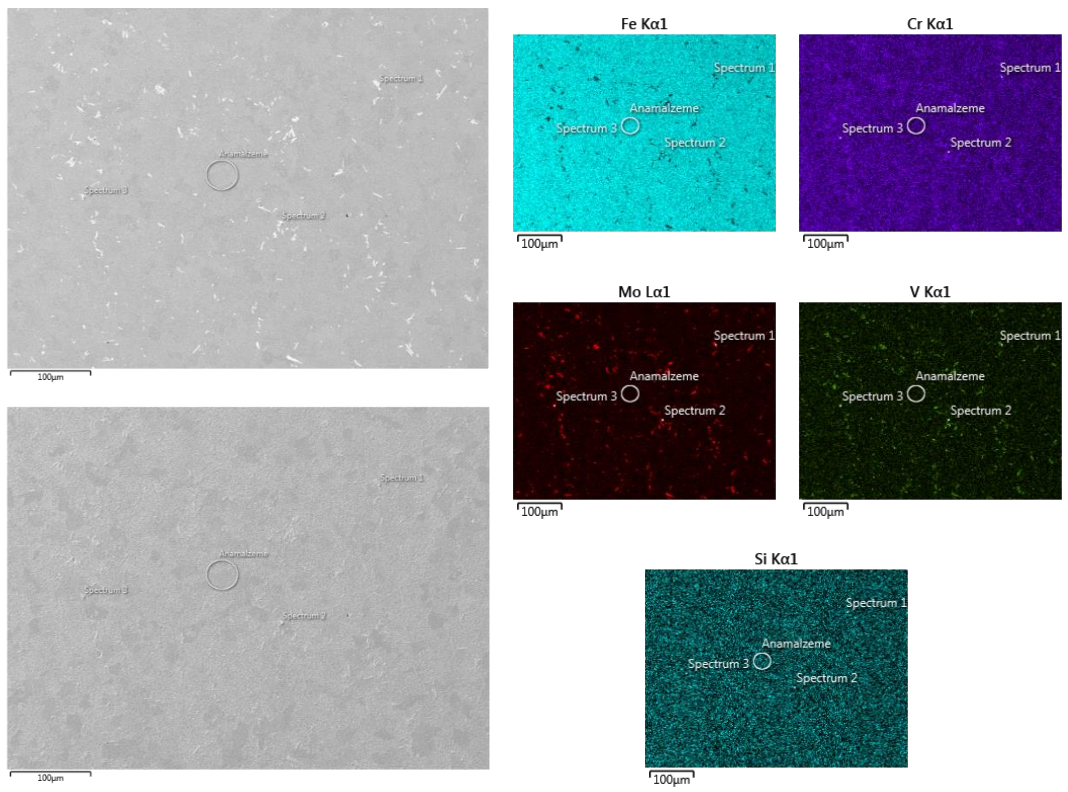


Figure 4.14. Surface mapping with SEM at 500X magnification

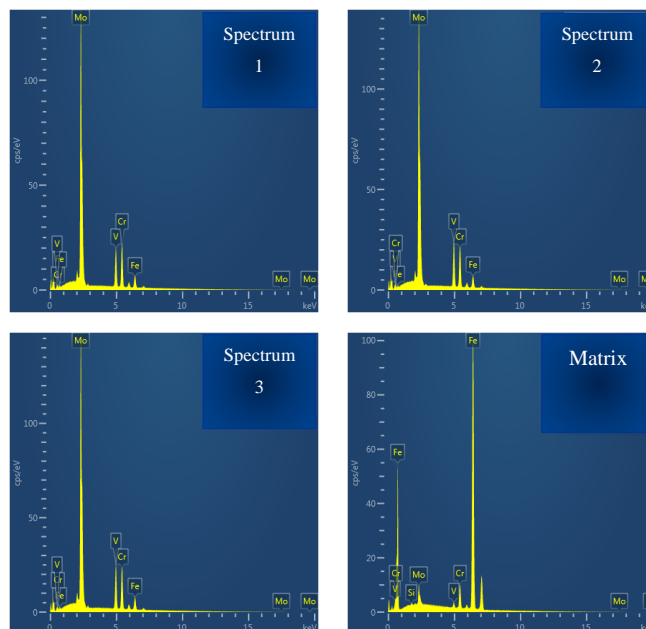


Figure 4.15. EDS analysis results of the surface mapping with SEM at 500X

Table 4.5 Chemical Composition of the Spectrums Analyzed in Figure 4.14

	Element (wt%)			
	Spectrum 1	Spectrum 2	Spectrum 3	Matrix
<b>Si</b>	-	-	-	0.17
<b>V</b>	11.82	13.92	13.45	0.92
<b>Cr</b>	13.1	12.27	12.52	4.39
<b>Fe</b>	5.7	5.58	5.88	90.36
<b>Mo</b>	69.38	68.23	68.15	4.17

In addition to the measurements made on the cross-section, EDS analysis of the primary carbides at 10.000X magnification was also conducted during the surface examination. Figure 4.16 below displays the analyzed carbides.

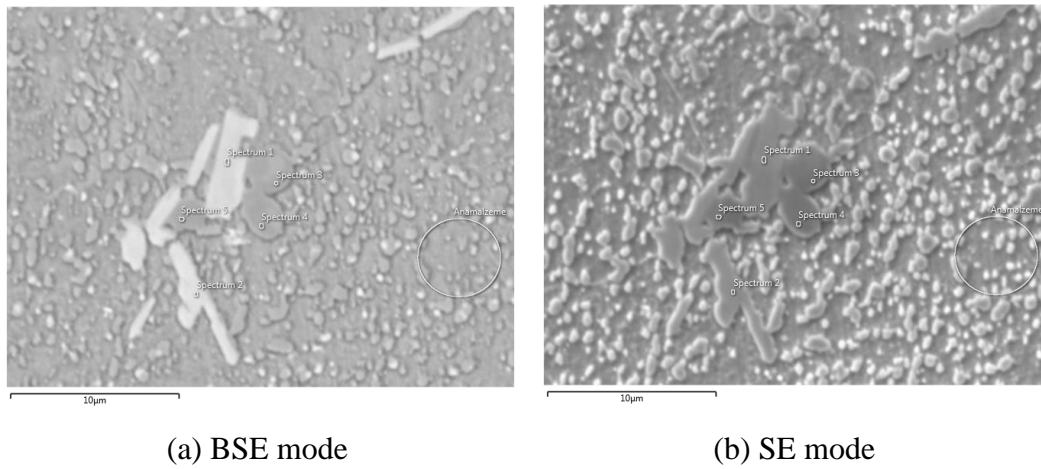


Figure 4.16. SEM images of the M50 steel matrix and primary carbides at 10.000X magnification from the surface (a) Back Scattered Electron (BSE) (b) Secondary Electron (SE) imaging modes of SEM

EDS measurements taken from the matrix and the primary carbides, as marked in Figure 4.16, are provided below in Figure 4.17 and the elemental composition of the carbides and matrix is summarized in Table 4.6.

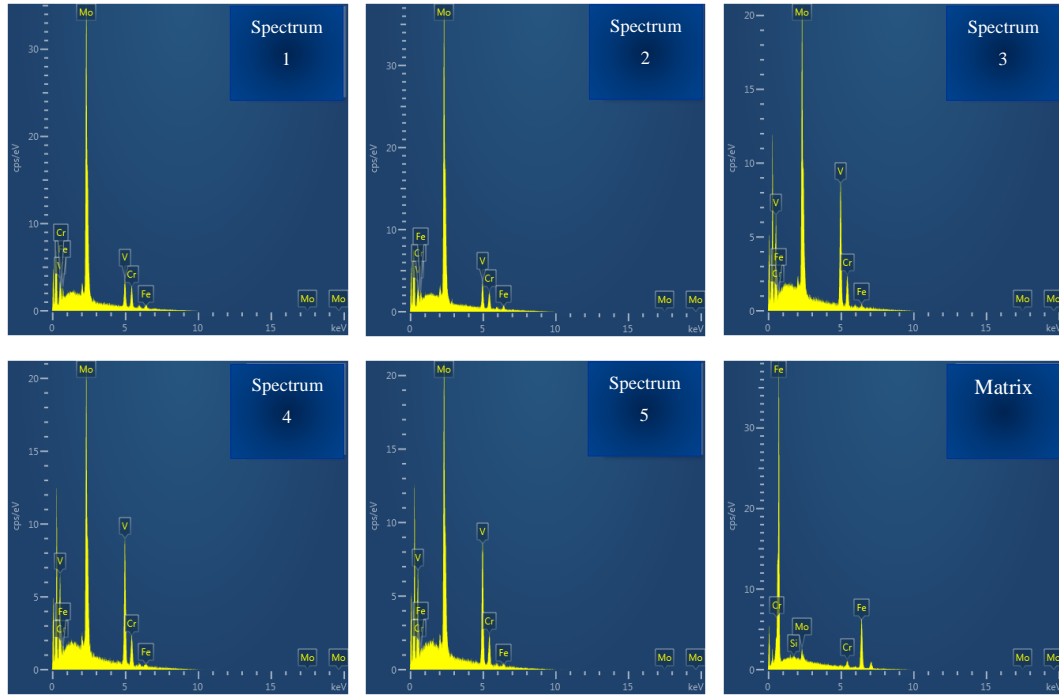


Figure 4.17. EDS analysis results of surface with SEM at 10.000X

Table 4.6 Chemical Composition of the Spectrums Analyzed in Figure 4.16

	Element (wt%)					
	Spectrum 1	Spectrum 2	Spectrum 3	Spectrum 4	Spectrum 5	Matrix
<b>Si</b>	-	-	-	-	-	0.11
<b>V</b>	15.25	15.29	46.34	46.66	45.89	-
<b>Cr</b>	13.46	10.87	8.04	8.03	7.88	4.14
<b>Fe</b>	6.29	7.63	3.87	2.96	3.76	92.95
<b>Mo</b>	65	66.21	41.75	42.34	42.48	2.8

Literature indicates that the carbides found in high-speed and high-alloy steels include MC (M denotes a metal atom),  $M_2C$ ,  $M_3C$ ,  $M_6C$ ,  $M_7C_3$ , and  $M_{23}C_6$  [88]. Additionally, Bridge et al. [89] examined the carbides in M50 using X-ray diffraction and microchemical analysis. Two types of primary carbides were identified in M50 steel, attributed to the different atomic numbers of the carbide-forming elements. EDS analysis of the element distribution clearly indicated that Mo, V, and C were primarily present in both types of primary carbides, with the key difference being the varying content of Mo and V. The primary carbides with bright contrast, rich in Mo, were referred to as Mo-rich primary carbides. In contrast, the dark-contrast primary carbides, which were rich in V, were termed V-rich primary carbides. The Mo-rich and V-rich primary carbides corresponded to  $M_2C$ -type and MC-type carbides, respectively. Characterization results further revealed that MC-type carbides generally exhibited a more circular profile, whereas  $M_2C$ -type carbides displayed a more complex shape with a higher aspect ratio overall [90-92].

When comparing the literature results with the as-received M50 microstructure from this study, EDS analyses of the primary carbides reveal that they mainly contain Mo, V, and C elements. Additionally, it was observed that Mo-rich carbides are white and have a complex shape, while V-rich carbides are gray and exhibit a more circular profile. Thus, the microstructure of M50 bearing steel is found to be in good agreement with the findings reported in the literature.

## **4.2 Microstructure After Hot Tensile Test Conditions**

This section describes the examination of microstructures observed after hot tensile testing using Stereo Microscope (SM) and Scanning Electron Microscope (SEM). In addition to the initial hot tensile tests performed at 1050°C, 1100°C, and 1150°C, further tests were carried out at intermediate temperatures to investigate microstructural changes. For this purpose, temperatures of 1125°C, 1138°C, 1163°C, and 1175°C were chosen, and these additional hot tensile tests were conducted again

using the Gleeble system. Consequently, the thermal deformation behaviour of M50 steel was analyzed based on the experiments conducted in the Gleeble system.

#### **4.2.1 Fracture Morphology After Hot Tensile Testing**

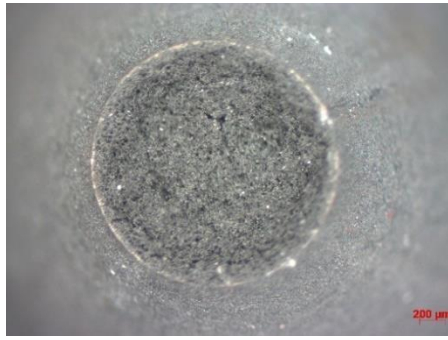
Based on the results from experimental hot tensile tests and subsequent simulations, fracture strain values were evaluated both experimentally and numerically, establishing the threshold value of the normalized Latham-Cockcroft criterion in Chapter 3. It was found that damage criteria vary with temperature, demonstrating that the  $LC_n$  damage criterion is a temperature-dependent material property. It is important to note that a temperature-dependent criterion is not common in hot metal forming simulations, and according to the literature review conducted, this study is the first to use such a model in the literature. For this reason, the microstructural evolution during the thermal deformation of M50 steel is critical to this thesis. For brevity, the metallurgical reasons for this behaviour in M50 steel were discussed in this chapter. To understand the implications of this behaviour, the fracture surfaces were examined first with a stereo microscope (SM) and then with a scanning electron microscope (SEM). The image of the specimens after hot tensile tests conducted at 1050°C, 1100°C, 1125°C, 1138°C, 1150°C, 1163°C, and 1175°C in the Gleeble system is shown below in Figure 4.18.



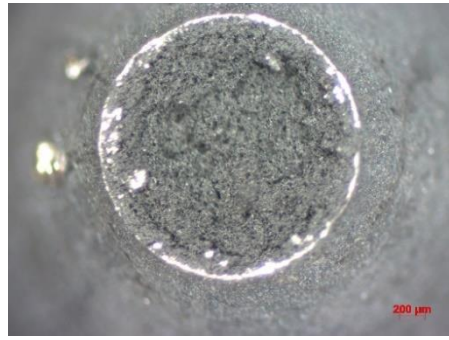
Figure 4.18. Specimens after hot tensile tests at various temperatures

The stereo microscope images of the fracture surface examinations of the tensile test specimens shown in Figure 4.18 are also provided in Figure 4.19. Subsequently, the fracture morphologies at different tensile test temperatures were examined in detail using SEM. Since the SEM images were taken regionally for each temperature, they are provided in detail in Figure 4.20 to Figure 4.26.





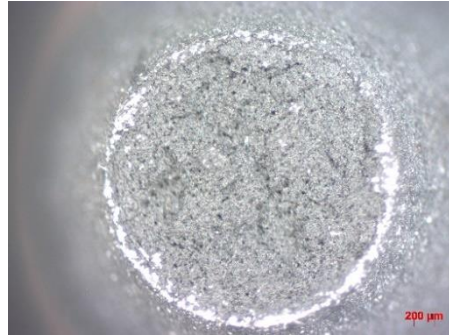
(a) 1050°C



(b) 1100°C



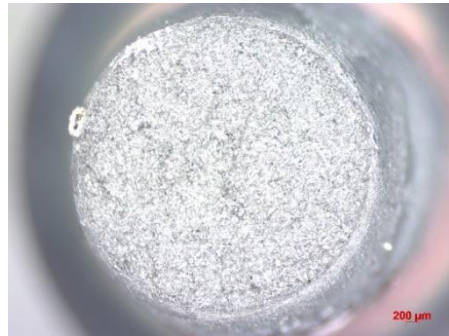
(c) 1125°C



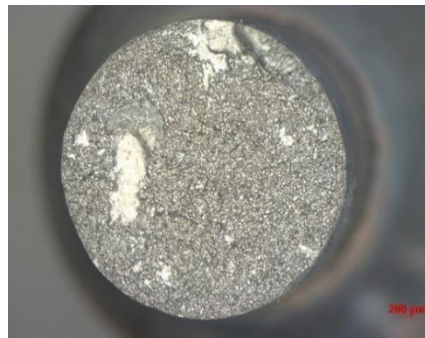
(d) 1138°C



(e) 1150°C



(f) 1163°C



(g) 1175°C

Figure 4.19. Fracture surfaces under SM after hot tensile tests



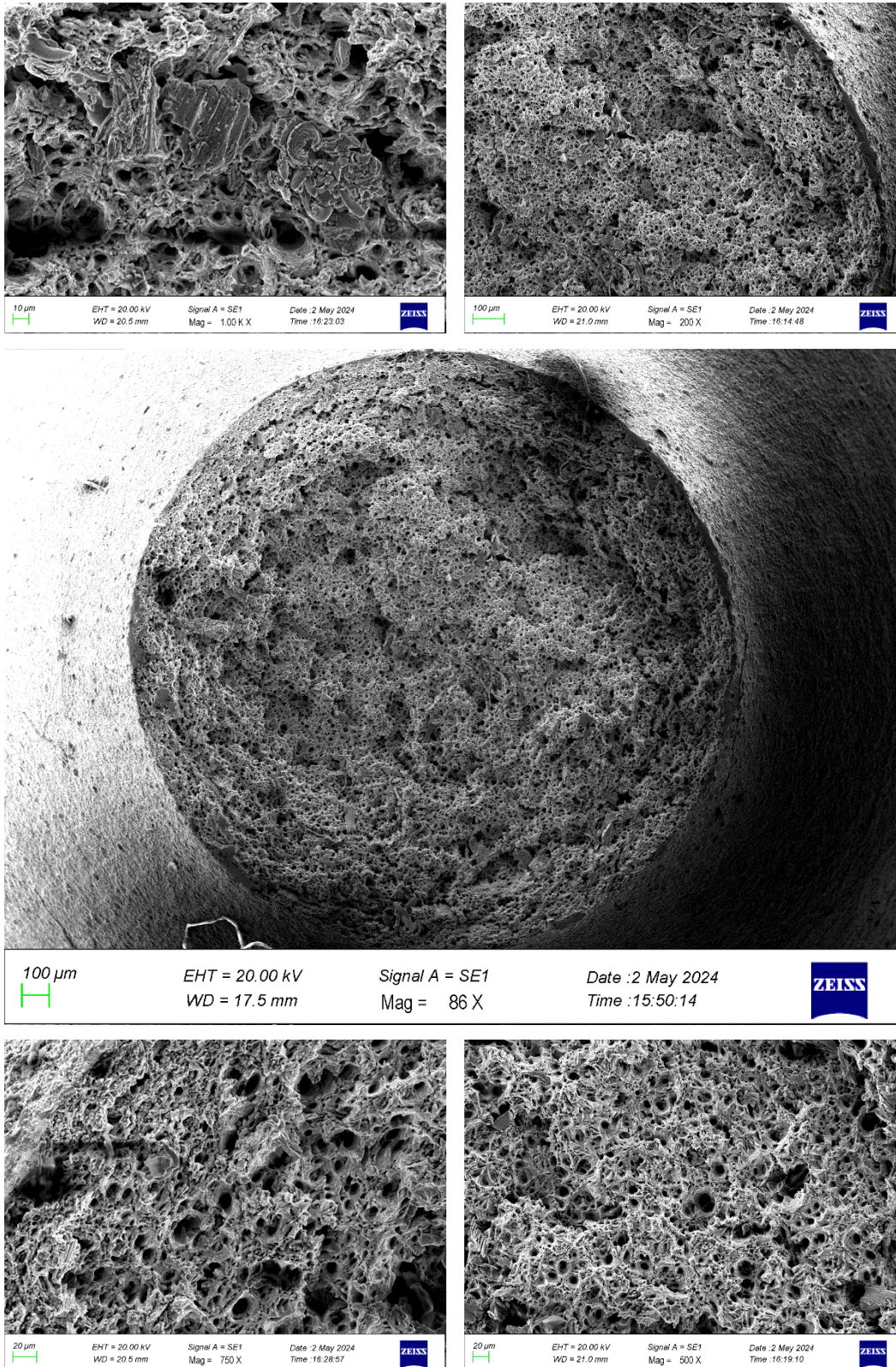


Figure 4.20. Fracture morphology under SEM after hot tensile test at 1050°C



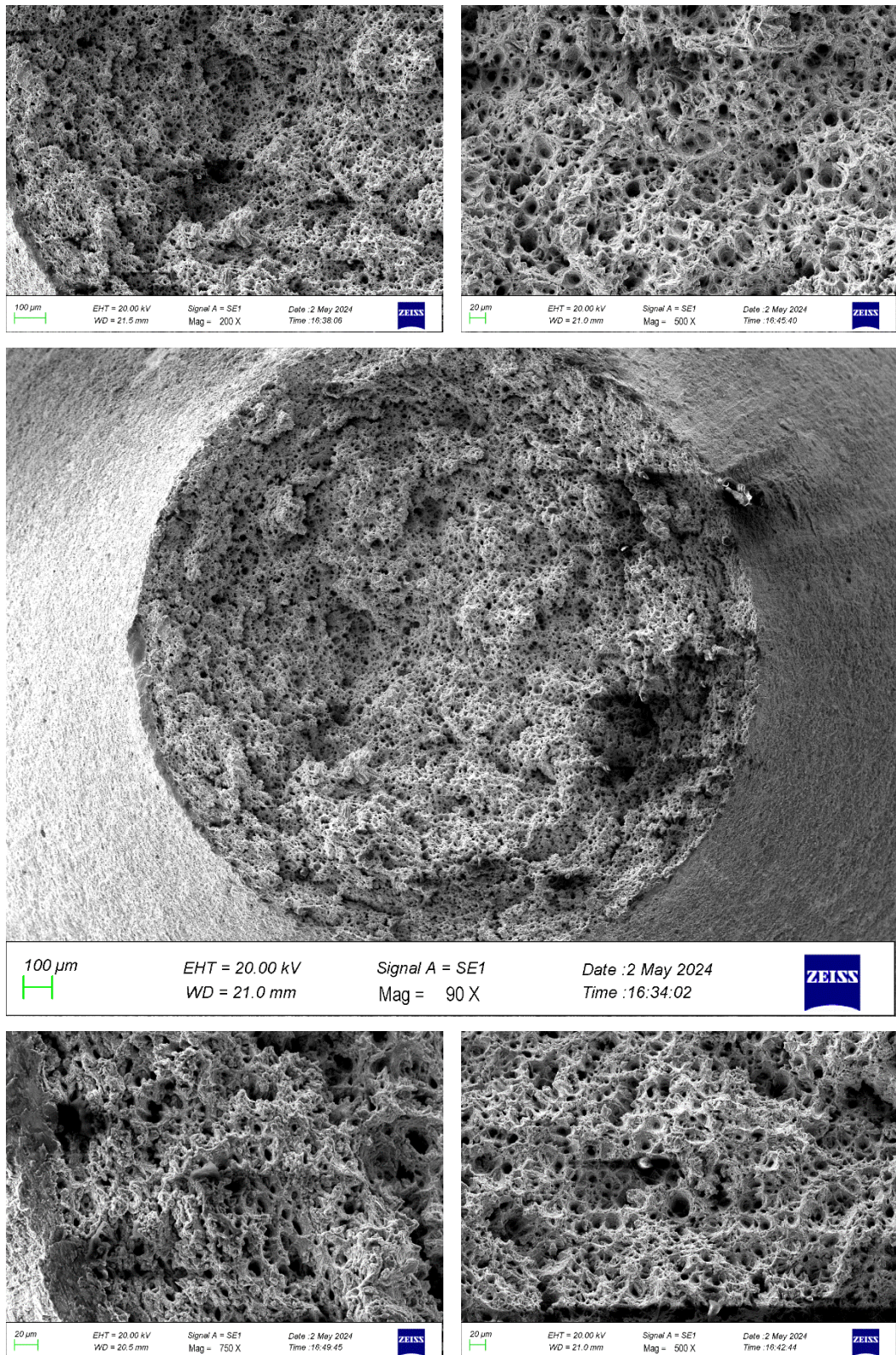


Figure 4.21. Fracture morphology under SEM after hot tensile test at 1100°C



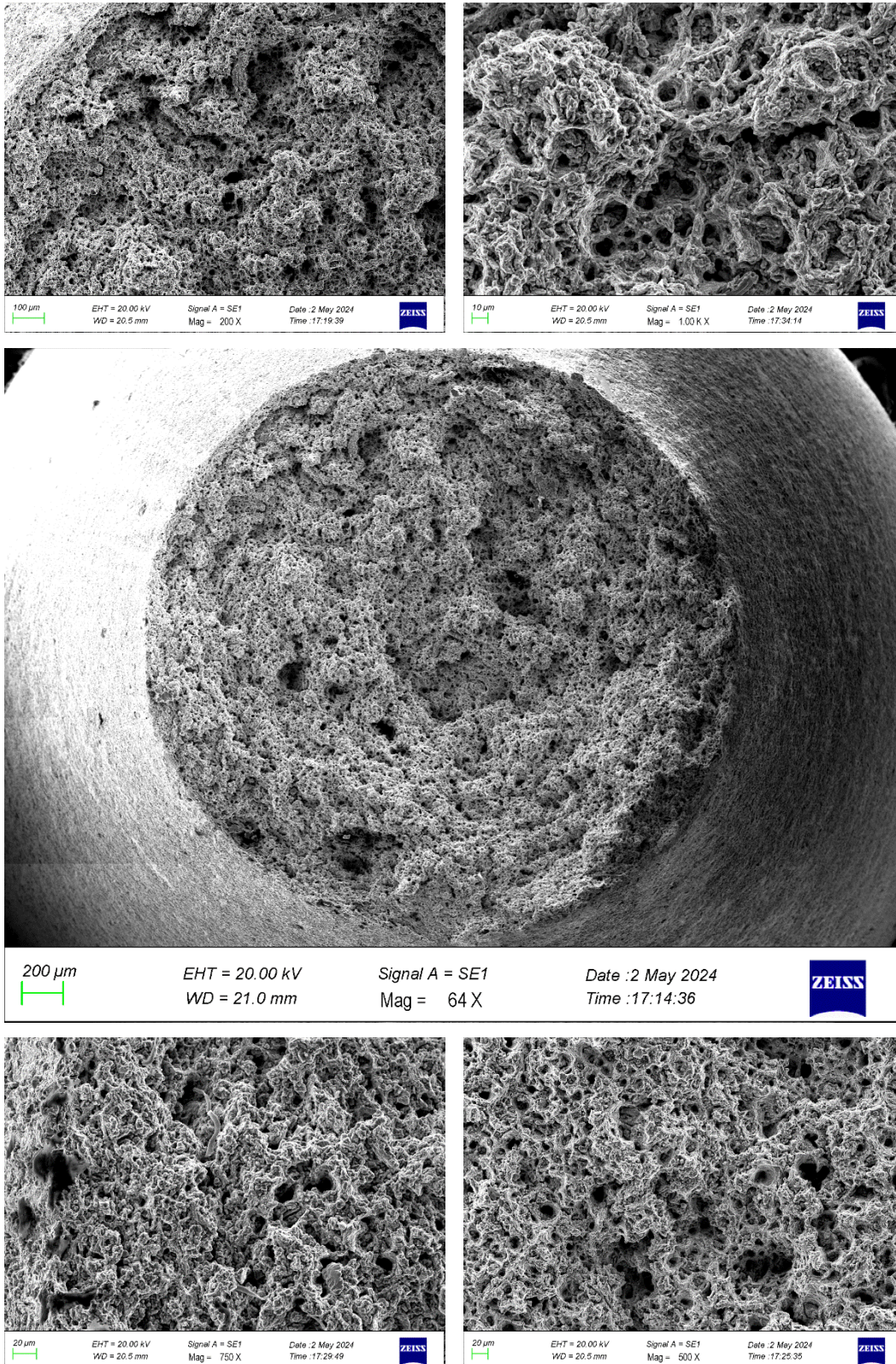


Figure 4.22. Fracture morphology under SEM after hot tensile test at 1125°C



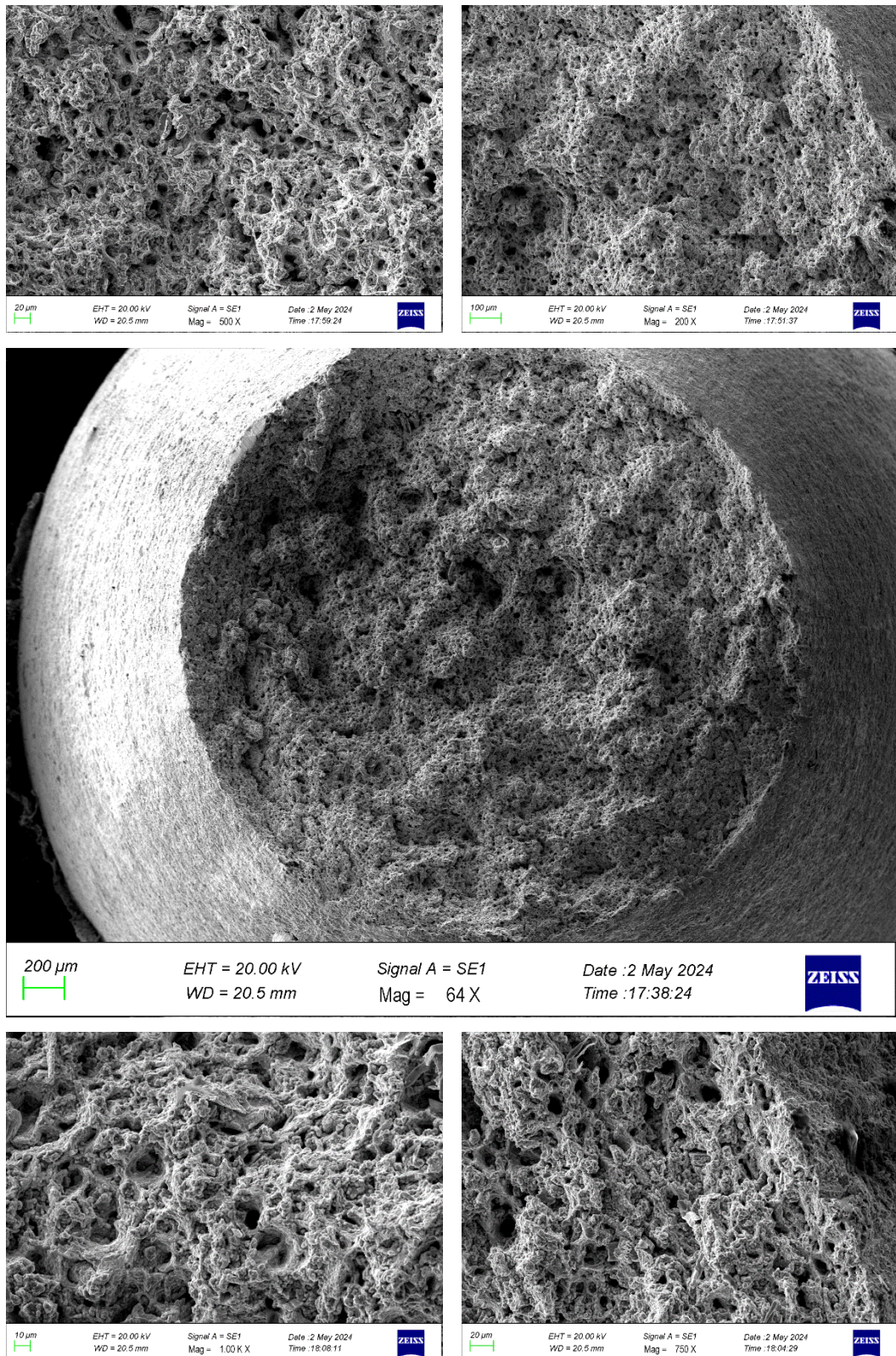


Figure 4.23. Fracture morphology under SEM after hot tensile test at 1138°C



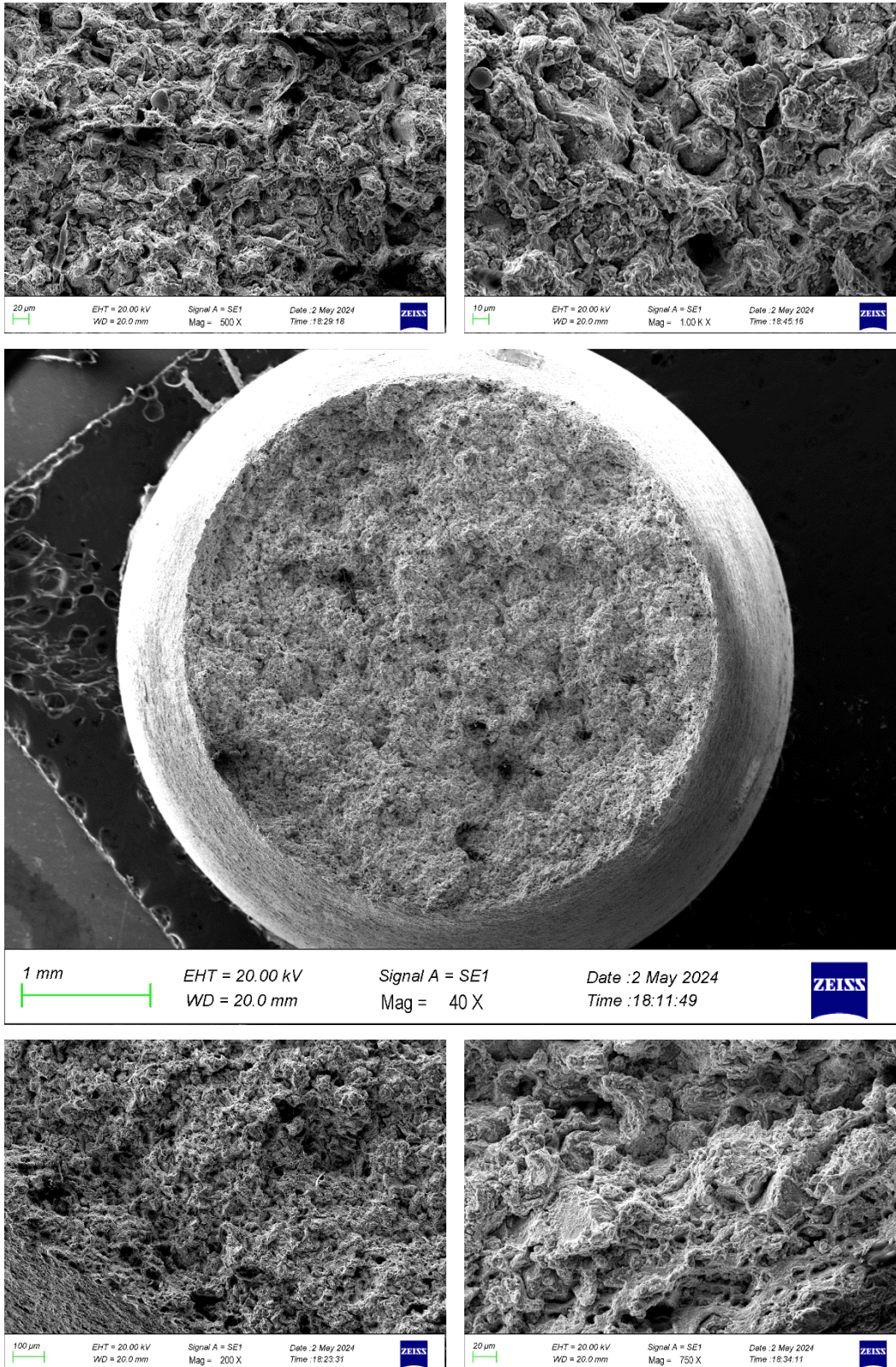


Figure 4.24. Fracture morphology under SEM after hot tensile test at 1150°C



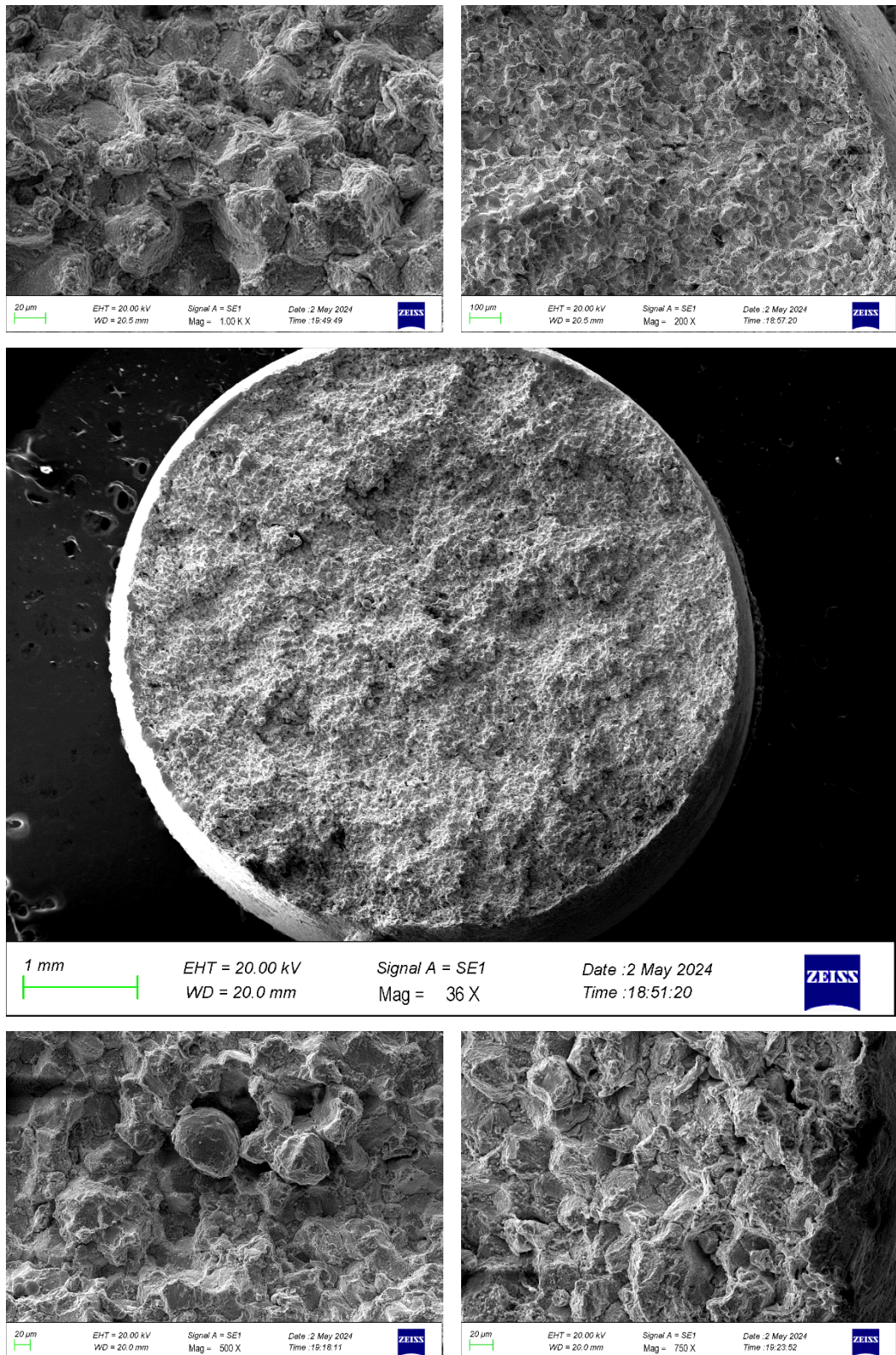


Figure 4.25. Fracture morphology under SEM after hot tensile test at 1163°C



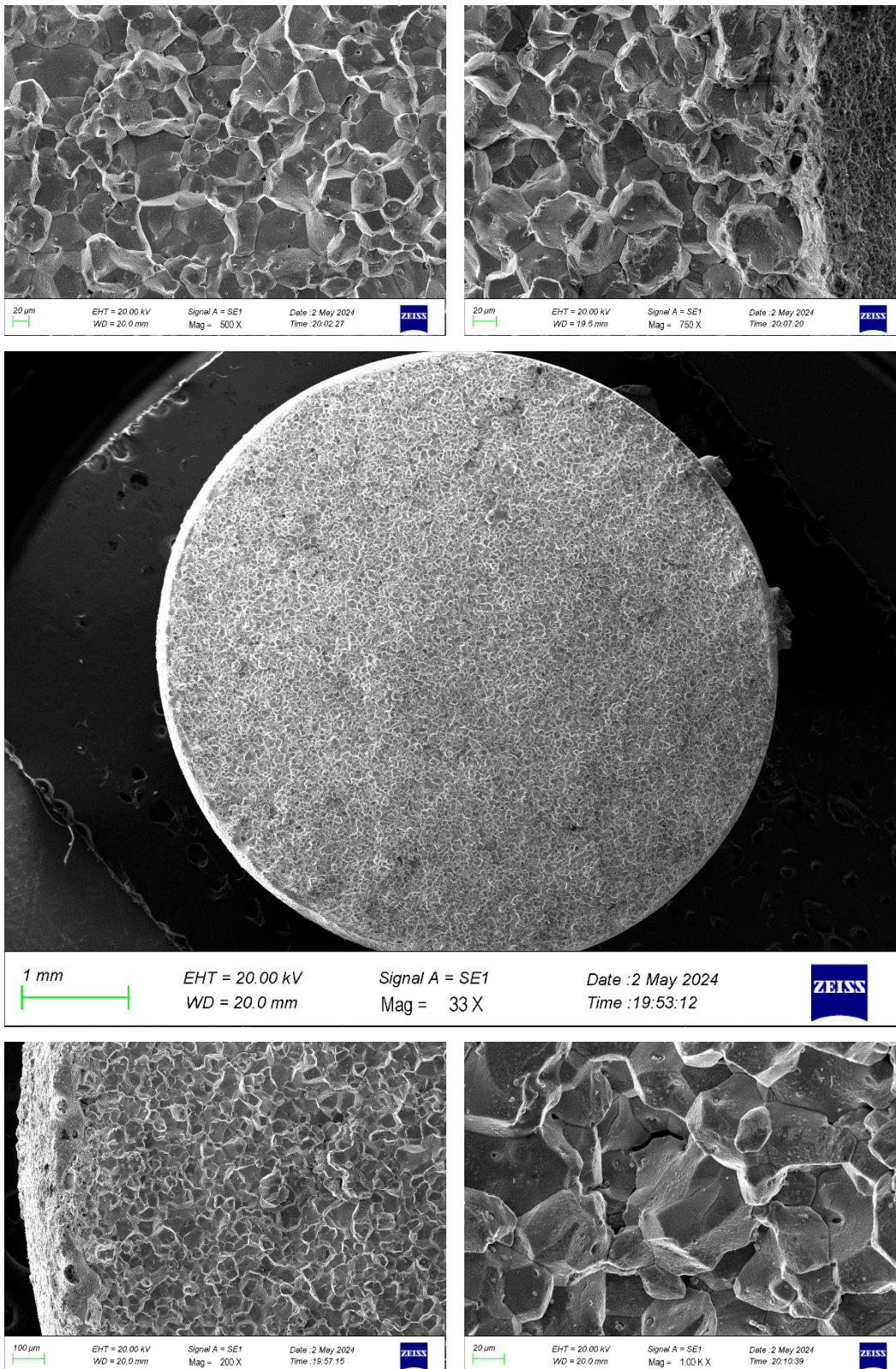


Figure 4.26. Fracture morphology under SEM after hot tensile test at 1175°C

Upon detailed examination of Figure 4.20 to Figure 4.26, a reduction in ductility can be observed. At temperatures below 1150°C (1050°C, 1100°C, 1125°C, 1138°C), as shown in Figure 4.20 to Figure 4.23, the appearance of dimples represents classic ductile fracture characteristics; in other words, a spongy appearance is clearly observed. After hot tensile testing at 1163°C, the microstructure examined in Figure 4.25 reveals partial grain boundary reduction.

When testing was conducted at 1175°C, complete loss of grain boundaries was observed. At this temperature, the complete disappearance of grain boundaries and the visibility of only the grains are detailed in Figure 4.26. This condition may be attributed to the segregation of impurities to grain boundaries caused by hot tensile tests (thermal processing) [93,94].

The strength of metals is understood to consist of two components: grain interior strength and grain boundary strength. At lower temperatures, grain boundary strength surpasses that of the grain interior. As the temperature rises, both diminish. Due to the instability of atoms and the higher presence of defects in the grain boundaries, the reduction in grain boundary strength occurs more rapidly than in the grain interior. At a specific temperature, known as the equi-cohesive temperature ( $T_E$ ), the strengths of the grain boundary and grain interior become equal. Beyond this point, further increases in temperature cause the grain boundary strength to fall below that of the grain interior. Therefore, when a material fractures at temperatures below  $T_E$ , the fracture is transgranular, whereas at temperatures above  $T_E$ , the fracture is intergranular [95,96].

Additionally, it was mentioned in the literature [97], that once the tensile test temperature surpassed the equi-cohesive temperature, intergranular fracture occurred due to the rapid decrease in grain boundary strength.

When the outputs from Figure 4.20 to Figure 4.26 were evaluated, and the fracture morphology after hot tensile tests was examined, it was observed that there was a transition from ductile fracture to intergranular fracture due to reduced ductility after

1150°C. Therefore, it was concluded that 1150°C can be assigned as the equi-cohesive temperature for M50.

Figure 4.27 provides higher magnification SEM images of the fracture morphology shown in Figure 4.26, taken after the hot tensile test at 1175°C, to investigate the cause of the complete disappearance of grain boundaries. In addition to the detailed SEM analysis of the 1175°C sample's subsurface, EDS analysis of trace-like regions was also conducted.

EDS analysis was performed on five different regions of the 1175°C sample's subsurface to examine the elemental composition in terms of weight percentages of iron (Fe), chromium (Cr), molybdenum (Mo), vanadium (V), oxygen (O), and manganese (Mn). Within this context, EDS measurements from the marked points in these regions are presented in Figure 4.28 to Figure 4.32.

Additionally, the chemical compositions of the analyzed spectra from these points can be found in Table 4.7 to Table 4.11.



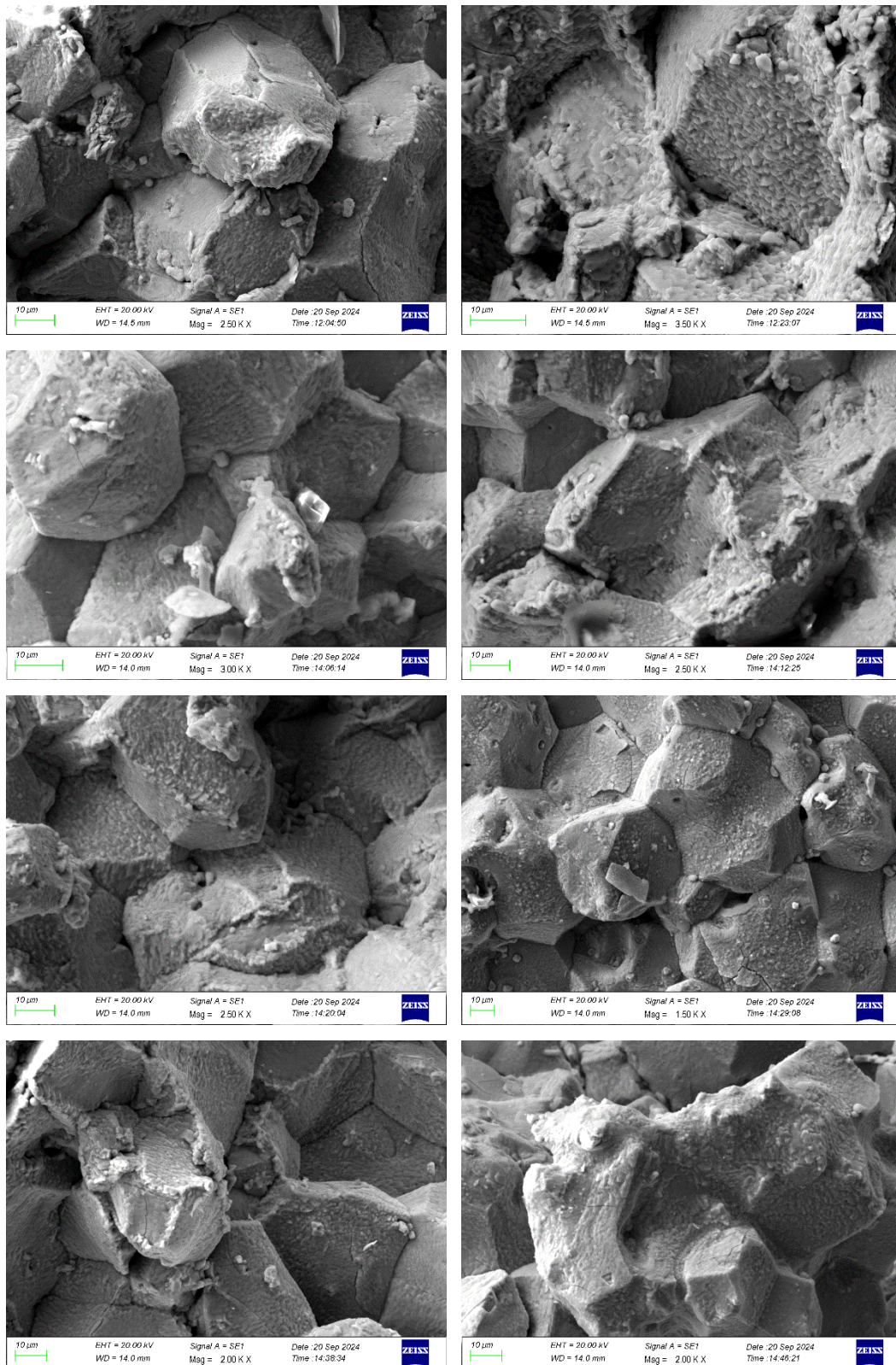
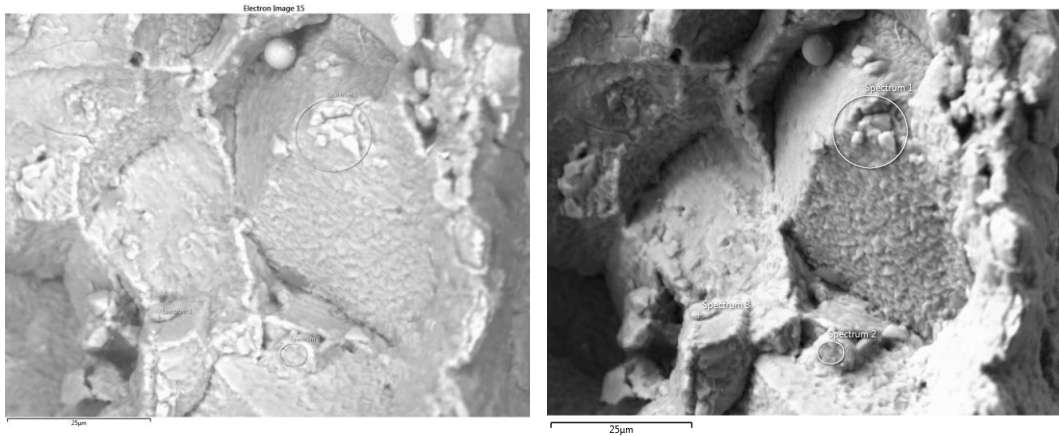


Figure 4.27. SEM examination of Figure 4.26 at higher magnification



(a) BSE mode

(b) SE mode

Figure 4.28. EDS spectra for subsurface (region 1) of the 1175°C sample (a) Back Scattered Electron (BSE) (b) Secondary Electron (SE) imaging modes of SEM

Table 4.7 Chemical Composition of the Spectrums Analyzed in Figure 4.34

	<b>Element (wt%)</b>		
	<b>Spectrum 1</b>	<b>Spectrum 2</b>	<b>Spectrum 3</b>
<b>O</b>	29.69	32.18	32.35
<b>V</b>	0.76	0.58	0.21
<b>Cr</b>	2.90	2.63	1.01
<b>Mn</b>	0.14	0.27	0.48
<b>Fe</b>	64.21	64.34	65.96
<b>Mo</b>	2.30	-	-

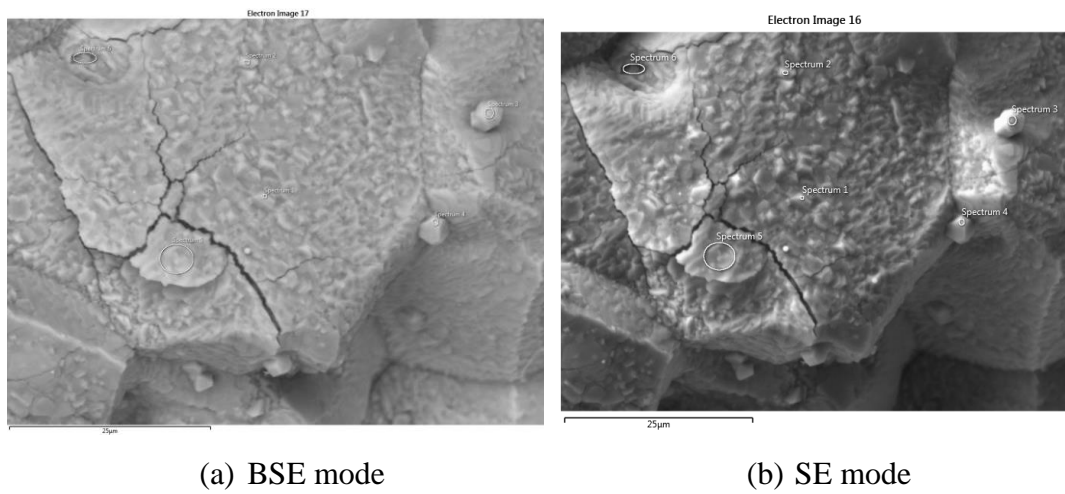


Figure 4.29. EDS spectra for subsurface (region 2) of the 1175°C sample (a) Back Scattered Electron (BSE) (b) Secondary Electron (SE) imaging modes of SEM

Table 4.8 Chemical Composition of the Spectrums Analyzed in Figure 4.29

	<b>Element (wt%)</b>					
	<b>Spectrum 1</b>	<b>Spectrum 2</b>	<b>Spectrum 3</b>	<b>Spectrum 4</b>	<b>Spectrum 5</b>	<b>Spectrum 6</b>
<b>O</b>	27.53	30.85	31.09	37.74	24.32	21.96
<b>V</b>	0.67	0.75	26.53	7.11	0.80	1.78
<b>Cr</b>	1.92	1.78	3.48	1.63	3.29	6.55
<b>Mn</b>	0.25	0.23	0.24	0.34	0.32	-
<b>Fe</b>	67.80	64.01	13.55	46.17	68.04	63.64
<b>Mo</b>	1.83	2.38	25.11	7.01	3.22	6.07

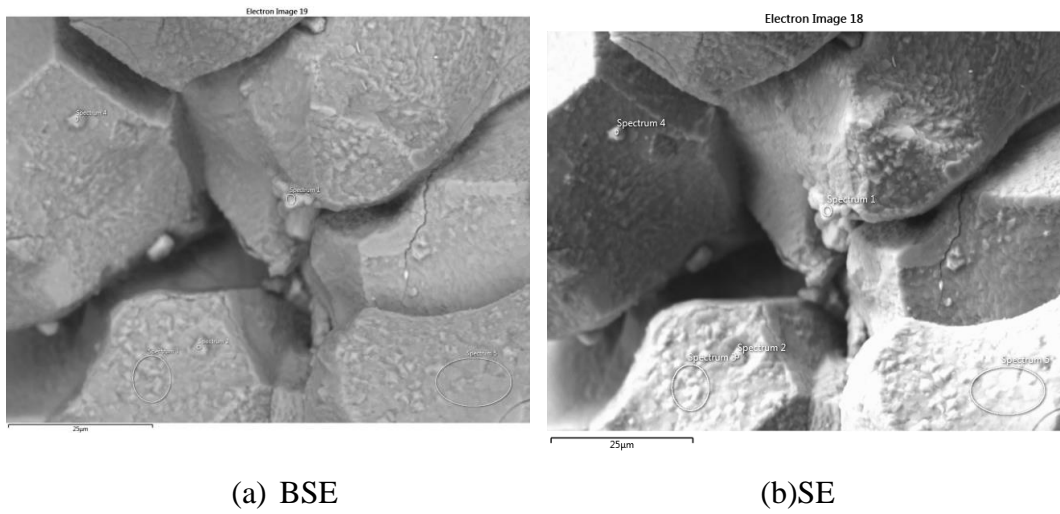


Figure 4.30. EDS spectra for subsurface (region 3) of the 1175°C sample (a) Back Scattered Electron (BSE) (b) Secondary Electron (SE) imaging modes of SEM

Table 4.9 Chemical Composition of the Spectrums Analyzed in Figure 4.30

	Element (wt%)				
	Spectrum 1	Spectrum 2	Spectrum 3	Spectrum 4	Spectrum 5
<b>O</b>	38.74	39.64	33.68	40.18	32.72
<b>V</b>	11.05	7.02	1.43	6.86	1.11
<b>Cr</b>	4.00	1.73	3.25	2.01	3.30
<b>Mn</b>	0.25	-	-	0.22	-
<b>Fe</b>	25.25	44.46	55.94	43.27	57.55
<b>Mo</b>	20.72	7.15	5.70	7.46	5.32

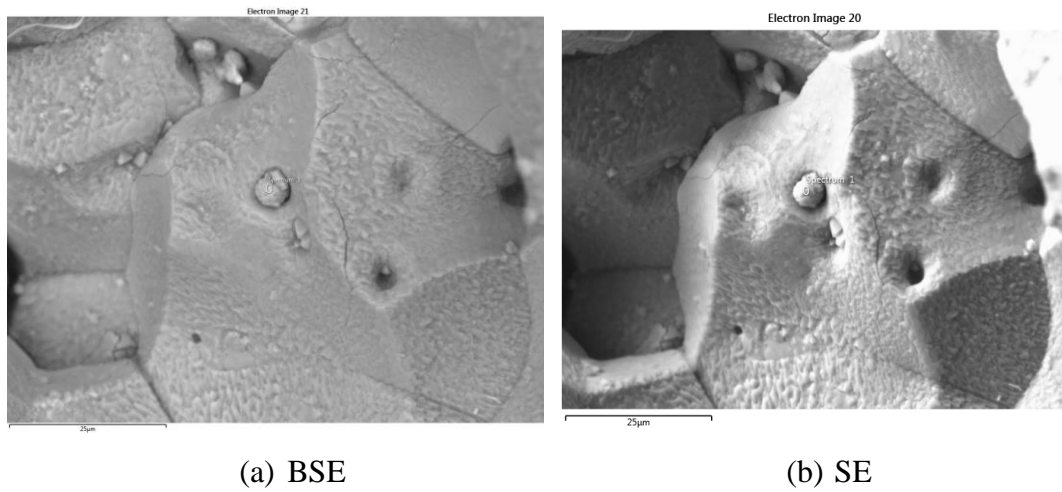


Figure 4.31. EDS spectra for subsurface (region 4) of the 1175°C sample (a) Back Scattered Electron (BSE) (b) Secondary Electron (SE) imaging modes of SEM

Table 4.10 Chemical Composition of the Spectrums Analyzed in Figure 4.31

	<b>Element (wt%)</b>
	<b>Spectrum 1</b>
<b>O</b>	38.60
<b>V</b>	14.13
<b>Cr</b>	3.13
<b>Mn</b>	0.20
<b>Fe</b>	22.98
<b>Mo</b>	20.97

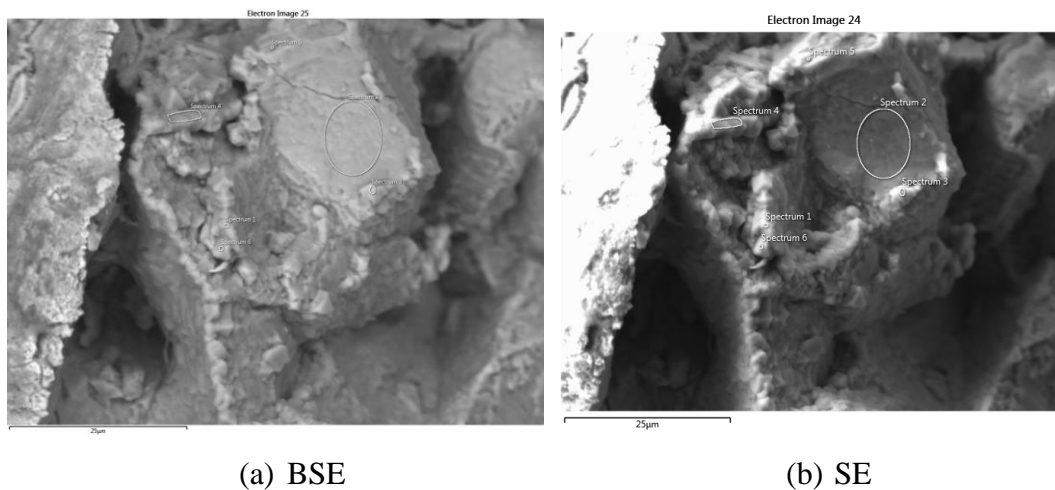


Figure 4.32. EDS spectra for subsurface (region 5) of the 1175°C sample (a) Back Scattered Electron (BSE) (b) Secondary Electron (SE) imaging modes of SEM

Table 4.11 Chemical Composition of the Spectrums Analyzed in Figure 4.32

	<b>Element (wt%)</b>					
	<b>Spectrum 1</b>	<b>Spectrum 2</b>	<b>Spectrum 3</b>	<b>Spectrum 4</b>	<b>Spectrum 5</b>	<b>Spectrum 6</b>
<b>O</b>	34.09	16.89	32.53	5.95	27.06	35.30
<b>V</b>	0.35	0.66	0.39	0.44	1.15	0.40
<b>Cr</b>	1.37	3.54	1.95	1.67	2.88	1.39
<b>Mn</b>	0.29	0.42	0.21	0.43	0.32	0.25
<b>Fe</b>	63.09	75.86	63.68	90.94	67.06	61.56
<b>Mo</b>	0.82	2.61	1.24	0.56	1.53	1.11

In the literature [98], it is stated that brief exposure to high temperatures in M50 steel results in the formation of a carbide shell along grain boundaries. It is also highlighted that this carbide layer facilitates the initiation of cracks at grain boundaries under tensile loads, significantly reducing the steel's plasticity. Additionally, the hardness and strength of the steel are slightly reduced.



Upon a more detailed examination of the sub-surface images of the fracture after hot deformation at 1175°C, as shown in Figure 4.28 to Figure 4.32, the structure was considered to be layered, resembling a carbide shell in the grain boundaries. EDS analyses were also conducted to examine the chemical composition of these surfaces, with the results presented in Table 4.7 to Table 4.11. These analyses revealed the presence of Fe and O elements on the shell-like surfaces instead of Mo and V elements.

As the final part of the fractography, an EDS trial was conducted on the fracture surface to determine whether traces of inclusions or carbide-forming elements could be detected in the dimples. On the surface of a ductile fracture, as illustrated in Figure 4.33 and Figure 4.34, dimples are visible, each corresponding to a void.

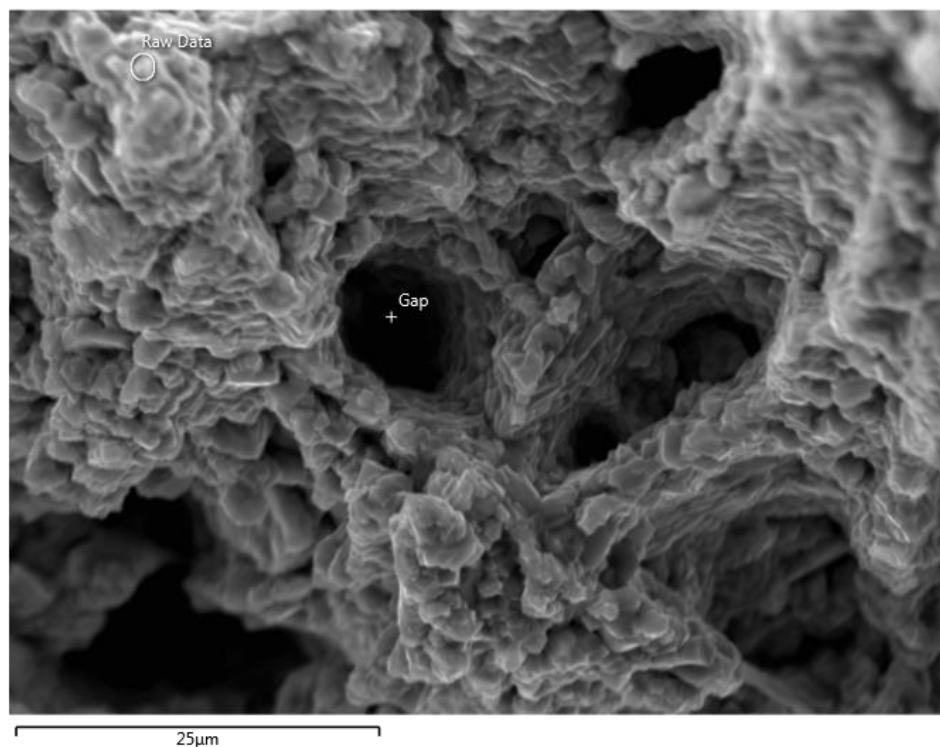


Figure 4.33. Dimple on the fracture surface after tensile test at 1125°C



Figure 4.34. Dimple on the fracture surface after tensile test at 1150°C

Ductile fracture follows considerable plastic deformation. When a material includes relatively hard particles that do not deform in sync with the surrounding matrix, voids form to accommodate these differences. This void nucleation process can involve events such as the breaking of the inclusion or separation at the boundary between the inclusion and the matrix. Fracture of a macroscopic sample only occurs when voids originating from different inclusions have expanded enough to merge. It is often possible to identify the inclusion responsible for the void by examining the depth of the dimple [99].

Within this concept, EDS analyses were also conducted on the dimples shown in Figure 4.33 and Figure 4.34. As a result of the SEM analyses, for accurate chemical analysis from the EDS detector, the output data should be at least 20,000 counts per second (cps). However, since the measurements from the dimples showed a value around 600 cps, the data collected from the dimples was considered unreliable and therefore not presented in the thesis.



## **4.2.2 Subsurface Examination of Fractured Surfaces**

Following the fracture morphology study, to gain insight into what might be causing decohesion at the lost grain boundaries and to understand the changes occurring in the microstructure at temperatures above 1138°C, the subsurface close to the fracture surface was metallographically prepared and examined using SEM. Additionally, to assess the microstructure along with the hot tensile test results, the average grain size was calculated from the subsurface microstructure, and hardness measurements were conducted.

### **4.2.2.1 Subsurface Analysis Using SEM**

To understand the thermal deformation of M50 specimens after hot tensile tests conducted at 1050°C, 1100°C, 1125°C, 1138°C, 1150°C, 1163°C and 1175°C, the fracture subsurfaces were first examined with SEM, and then their crystallographic structures were evaluated using EBSD (Electron Backscatter Diffraction). Subsurface SEM examinations following the hot tensile tests are presented in Figure 4.35 to Figure 4.41.

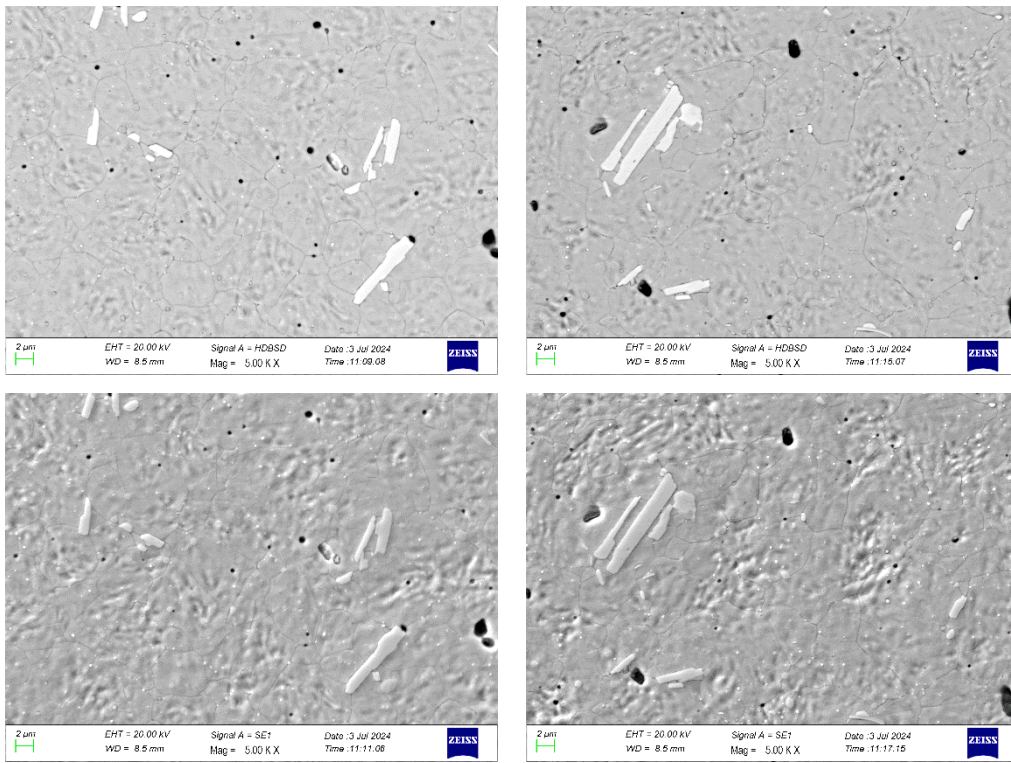


Figure 4.35. Subsurface of the fracture surface after hot tensile test at 1050°C

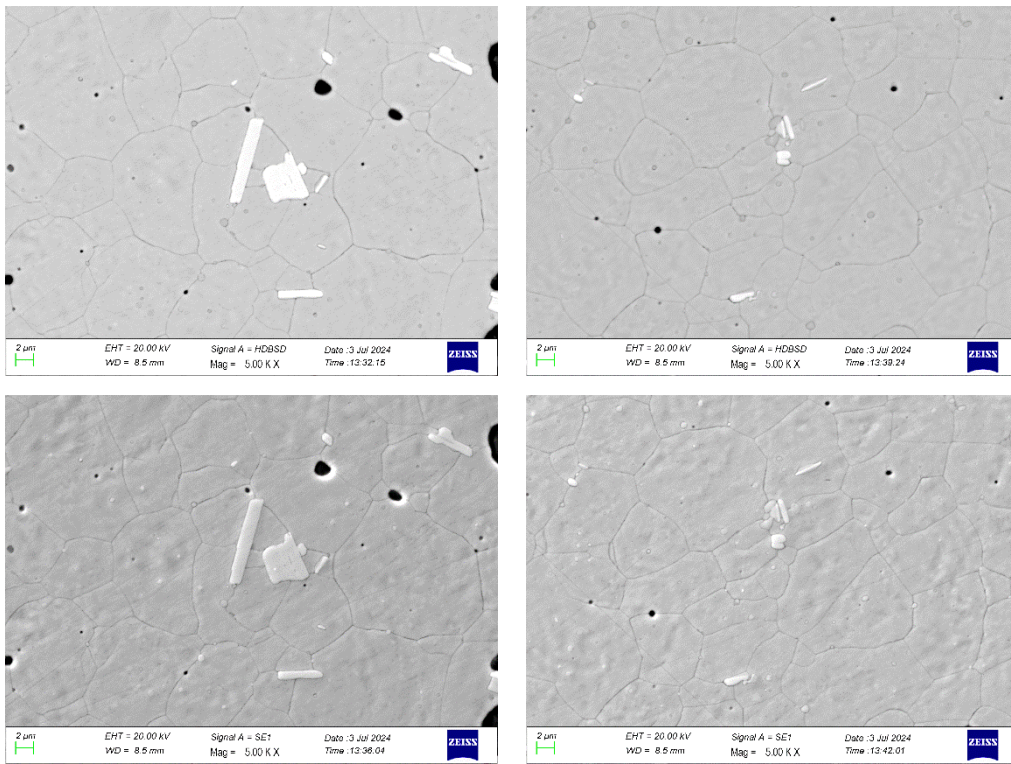


Figure 4.36. Subsurface of the fracture surface after hot tensile test at 1100°C

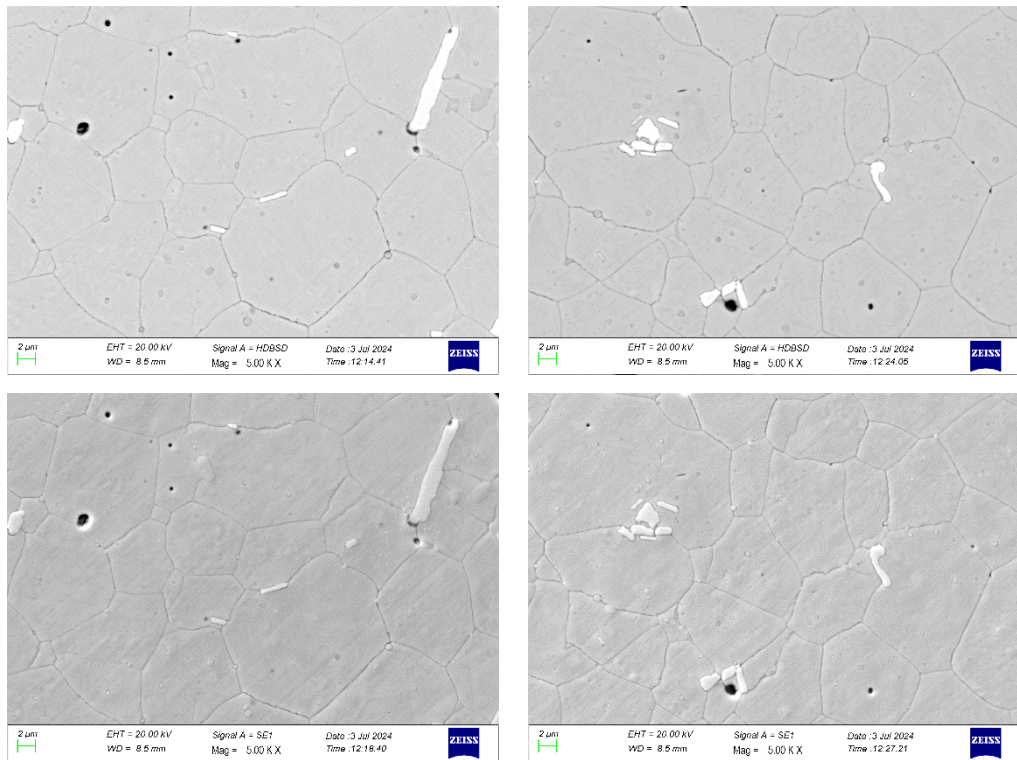


Figure 4.37. Subsurface of the fracture surface after hot tensile test at 1125°C

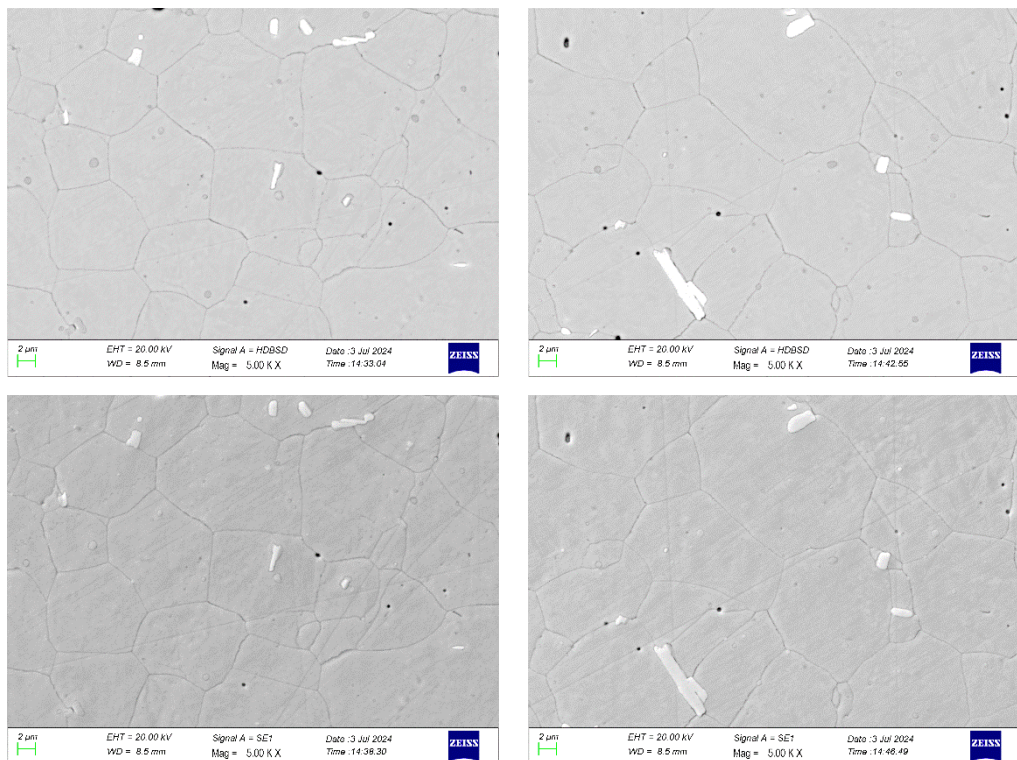


Figure 4.38. Subsurface of the fracture surface after hot tensile test at 1138°C



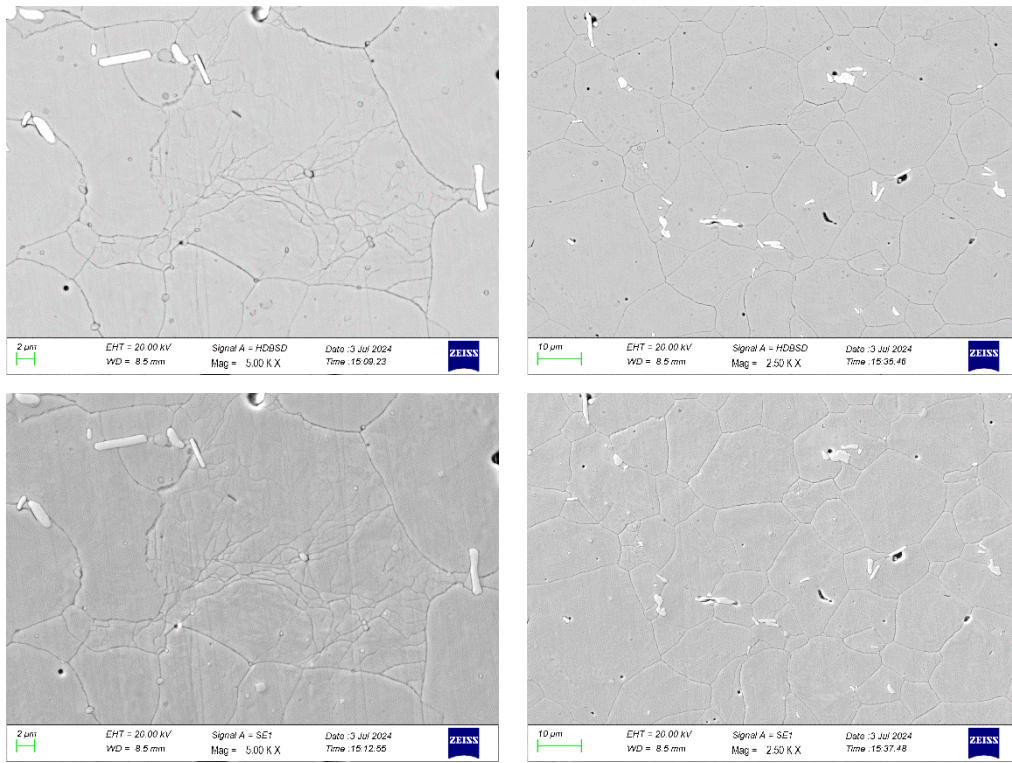


Figure 4.39. Subsurface of the fracture surface after hot tensile test at 1150°C

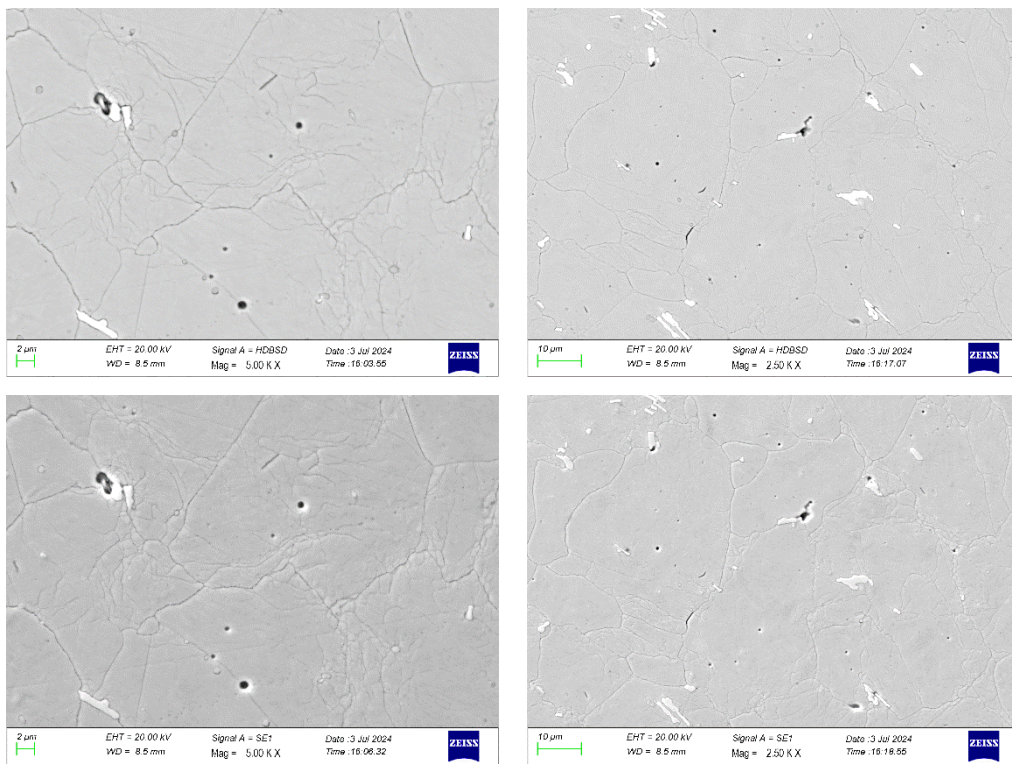


Figure 4.40. Subsurface of the fracture surface after hot tensile test at 1163°C

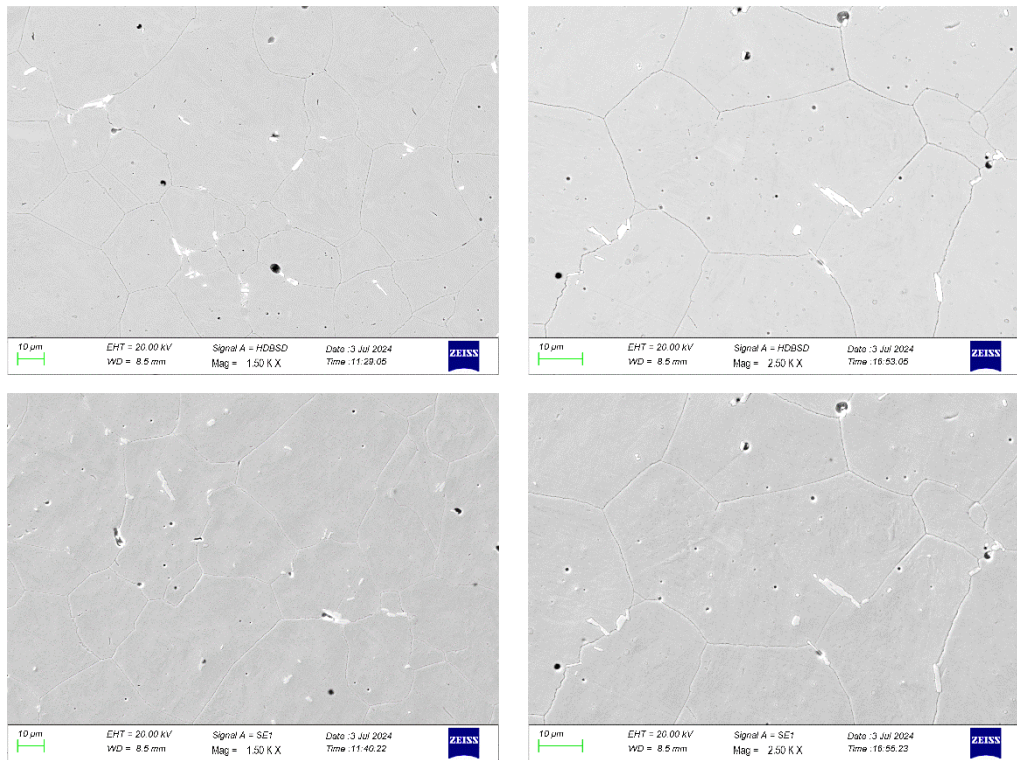


Figure 4.41. Subsurface of the fracture surface after hot tensile test at 1175°C

Based on Figure 4.35 to Figure 4.38, similar microstructures were observed in the subsurface examinations. After the hot tensile tests conducted at 1150°C and 1163°C, which occurred above 1138°C, different microstructures were observed in these subsurfaces, as shown in Figure 4.39 and Figure 4.40. Despite 1150°C being a high temperature, the presence of partially dynamically recrystallized grains is thought to possibly be due to the very rapid strain rate of  $10 \text{ s}^{-1}$  during the hot tensile tests. This raises the question of whether the observed differences in the microstructure could be attributed to dynamic recrystallization. To assess whether the microstructure observed at 1150°C and 1163°C was due to dynamic recrystallization, the crystallographic structure of the specimens tested at temperatures above 1138°C was analyzed using EBSD. To compare these structures with the microstructure below 1138°C, the specimen from the 1125°C tensile test was selected as a representative microstructure, and the EBSD analyses were

compared. Between Figure 4.42 and Figure 4.45, the EBSD analysis results are provided.

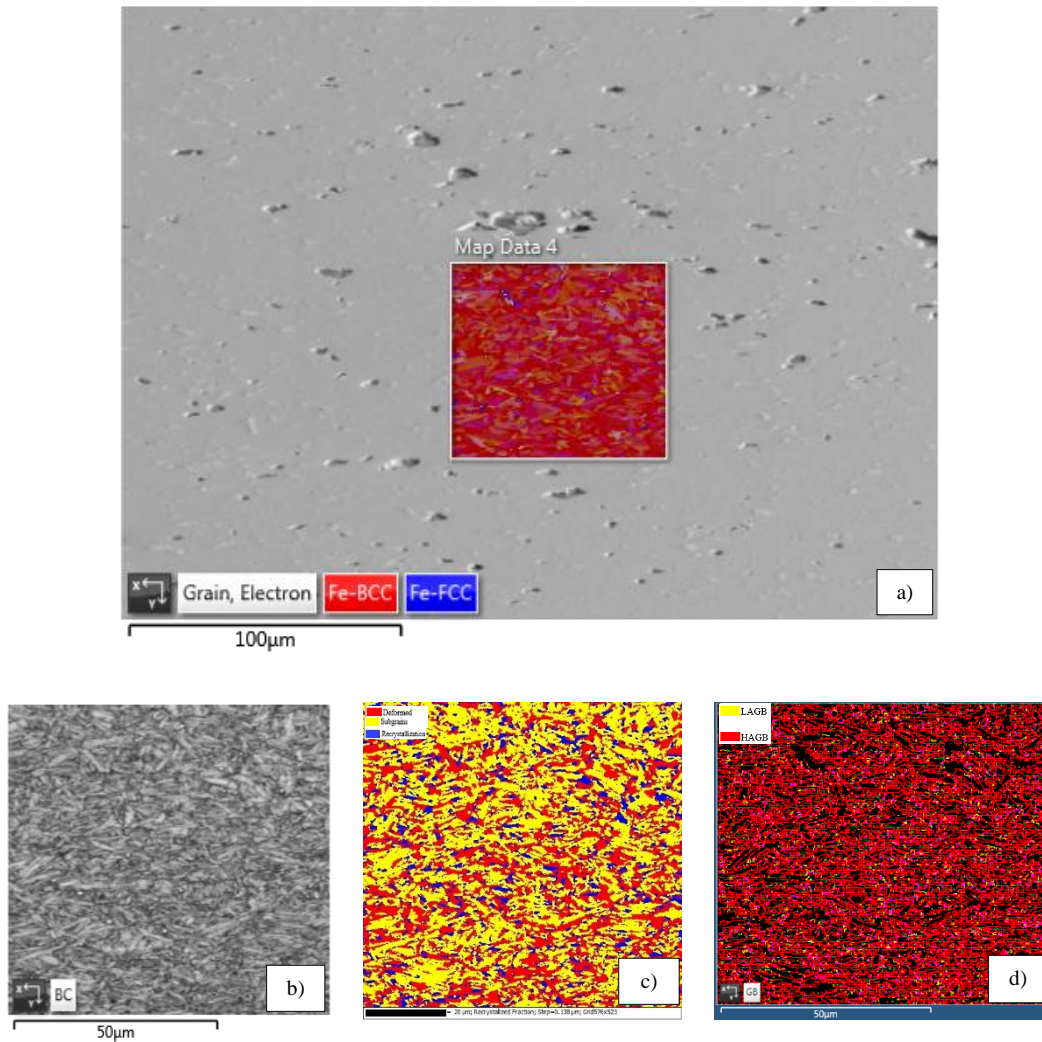


Figure 4.42. EBSD images (a) Layered, b) Band Contrast (BC), c) Recrystallized Fraction and d) Grain Boundary (GB) of the map data) for specimen under deformed at  $1125^{\circ}\text{C} / 10\text{s}^{-1}$



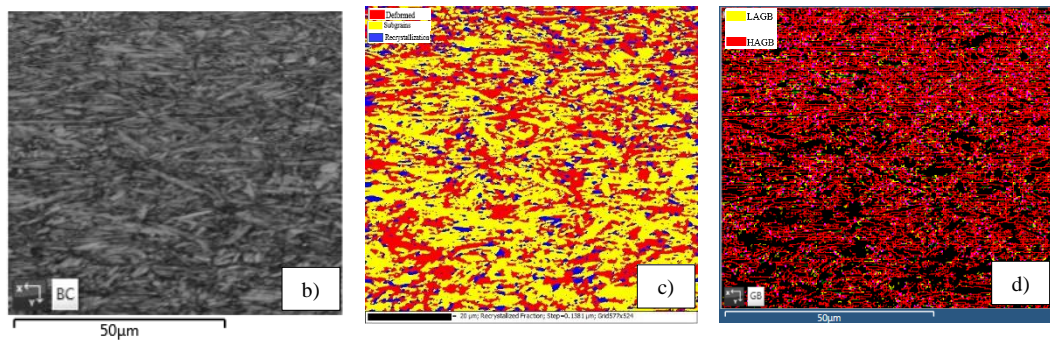
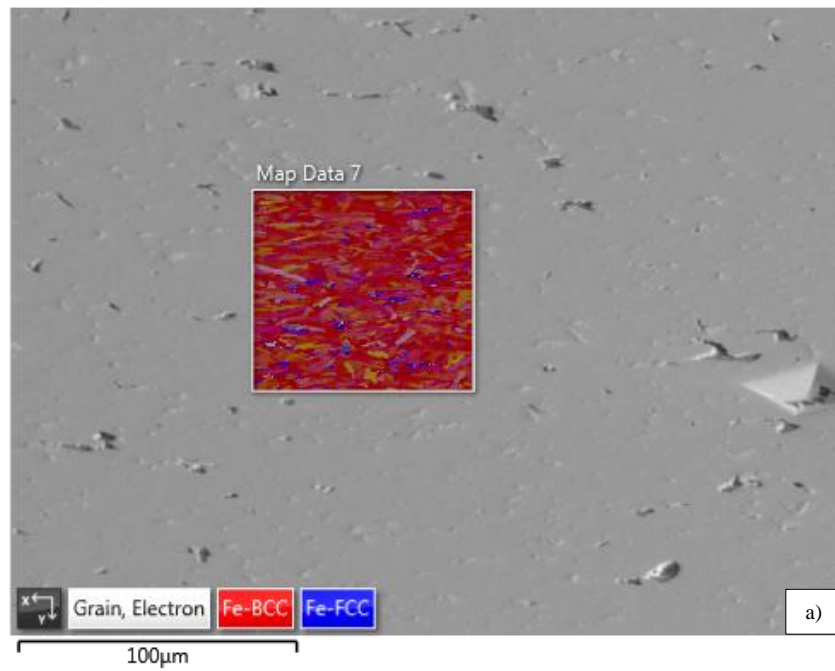


Figure 4.43. EBSD images (a) Layered, b) Band Contrast (BC), c) Recrystallized Fraction and d) Grain Boundary (GB) of the map data) for specimen under deformed at  $1150^{\circ}\text{C} / 10\text{s}^{-1}$

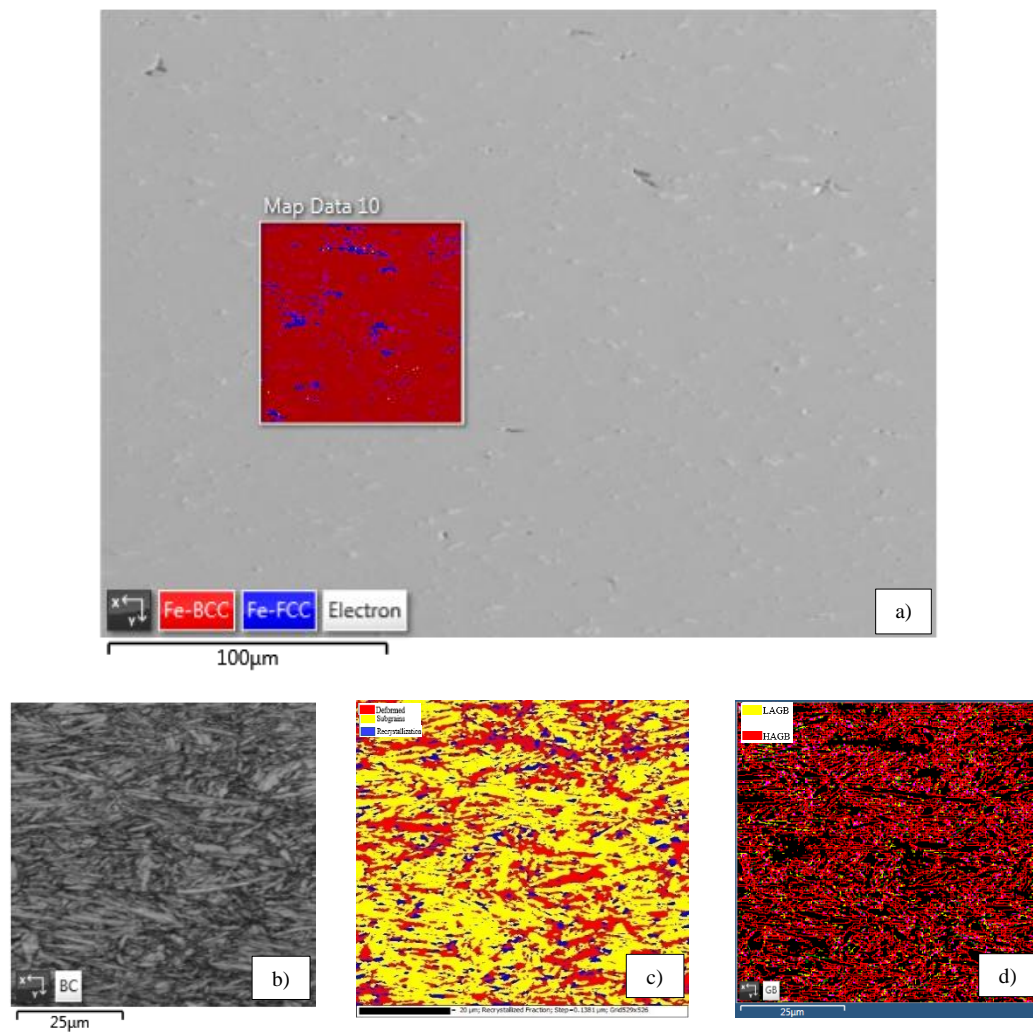


Figure 4.44. EBSD images (a) Layered, b) Band Contrast (BC), c) Recrystallized Fraction and d) Grain Boundary (GB) of the map data) for specimen under deformed at  $1163^{\circ}\text{C} / 10\text{s}^{-1}$



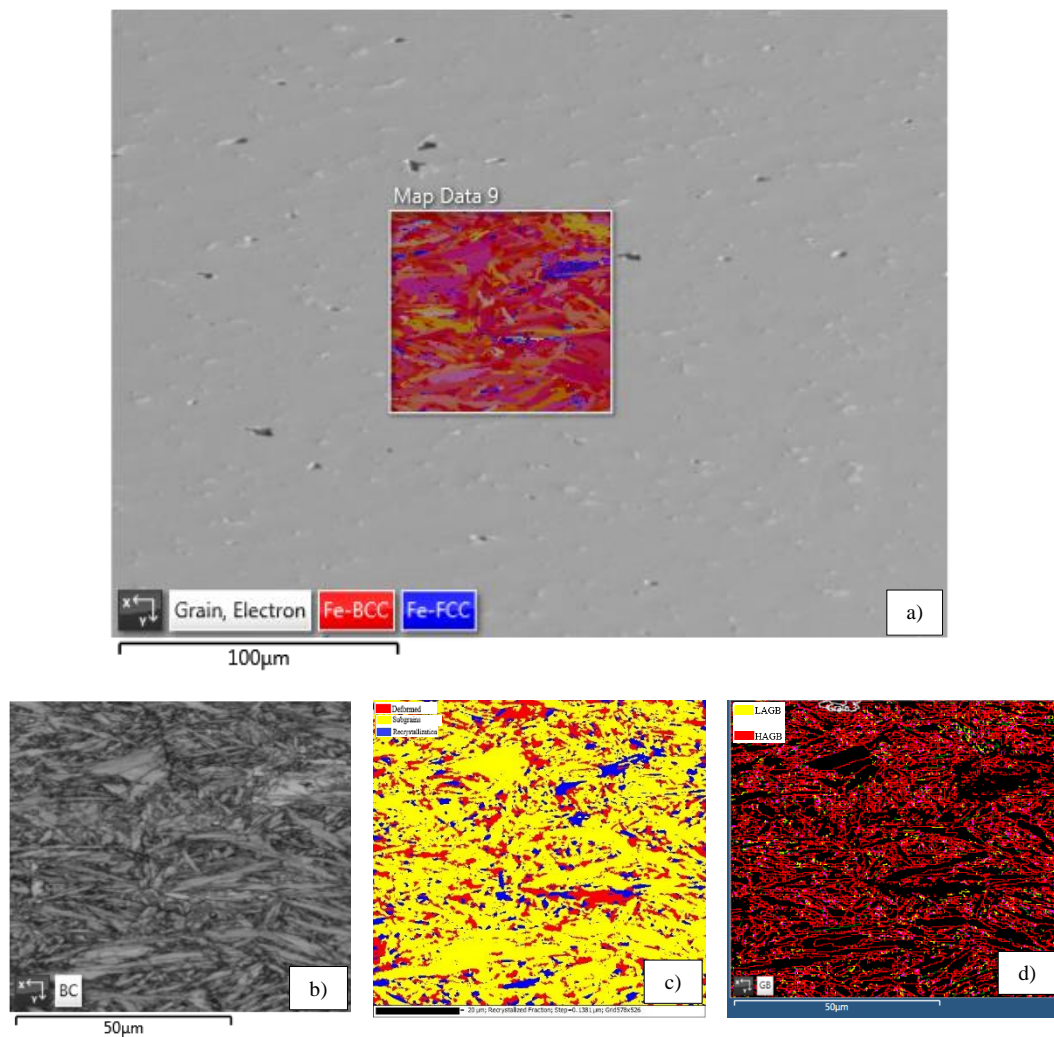


Figure 4.45. EBSD images (a) Layered, (b) Band Contrast (BC), (c) Recrystallized Fraction and (d) Grain Boundary (GB) of the map data) for specimen under deformed at  $1175^{\circ}\text{C} / 10\text{s}^{-1}$

The misorientation angle at the interface of neighboring crystal grains is denoted by  $\Theta$  with high angle grain boundaries evaluated as  $\Theta > 15^{\circ}$  and low angle grain boundaries as  $15^{\circ} > \Theta > 5^{\circ}$ . The rise in the fraction of dynamically recrystallized (DRXed) grains can be attributed to the alteration in the proportion of low angle grain boundaries. Dynamically recrystallized grains develop through the conversion of low angle grain boundaries (LAGBs) into high angle grain boundaries (HAGBs),

indicating that a reduction in the LAGB fraction signifies the formation of DRXed grain [100,101]. Figure 4.46 and Figure 4.47 show the results from EBSD characterization of specimens subsurfaces tested under 1125°C, 1150°C, 1163°C and 1175°C.

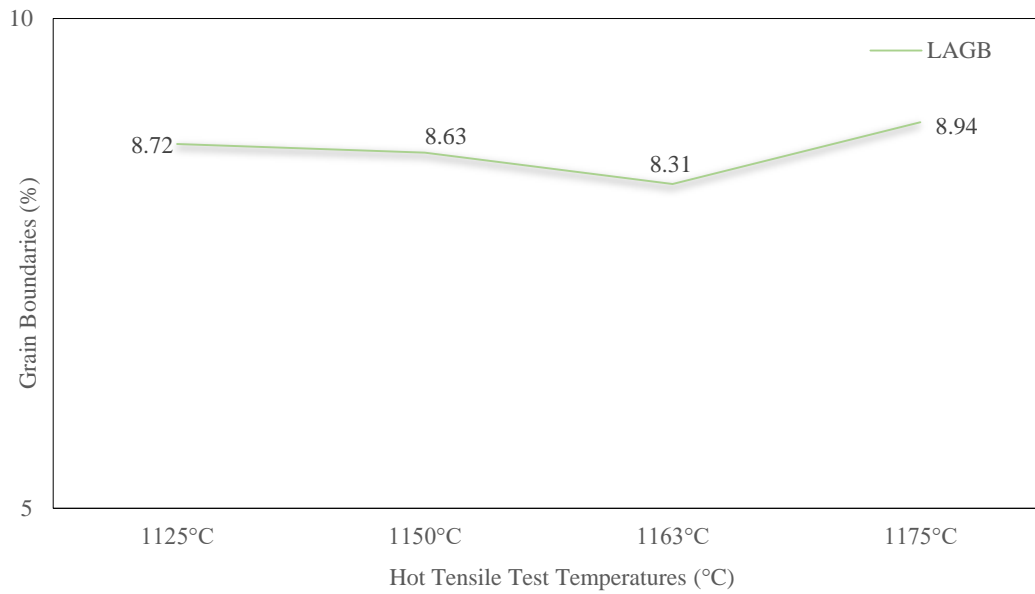


Figure 4.46. LAGB (%) vs hot tensile test temperatures (°C)

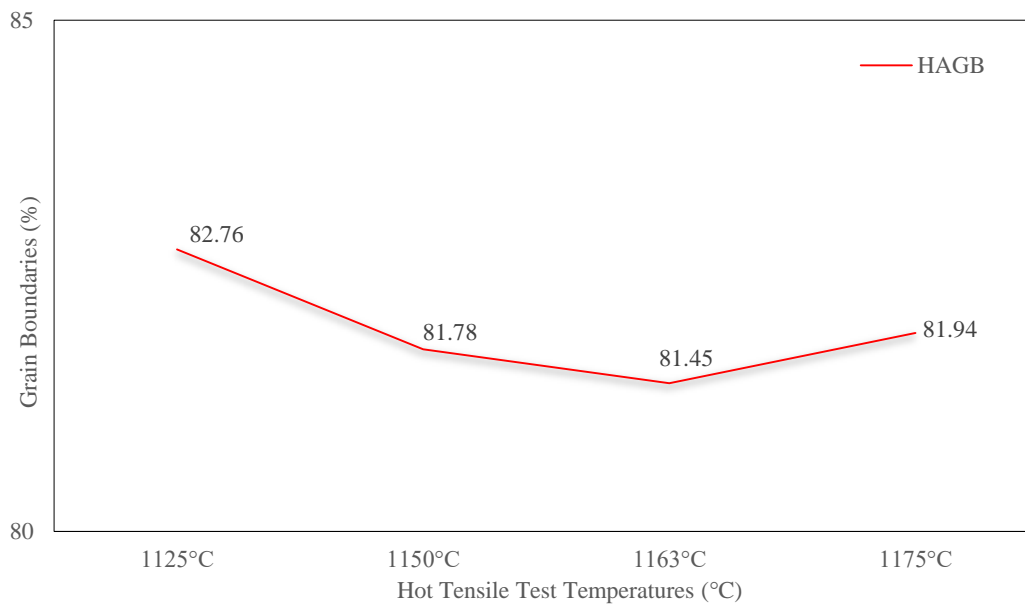


Figure 4.47. HAGB (%) vs hot tensile test temperatures (°C)

Analysis of EBSD results for subsurface specimens following hot tensile tests conducted at 1125°C, 1150°C, 1163°C, and 1175°C (as shown in Figure 4.46 and Figure 4.47) reveals that the amount of LAGBs remains relatively unchanged, with no increase in HAGB content.

In addition, the number of sub-boundaries (SB) formed during hot tensile tests, with misorientation angles in the range of  $2^\circ < \theta < 5^\circ$ , was examined in Figure 4.48.

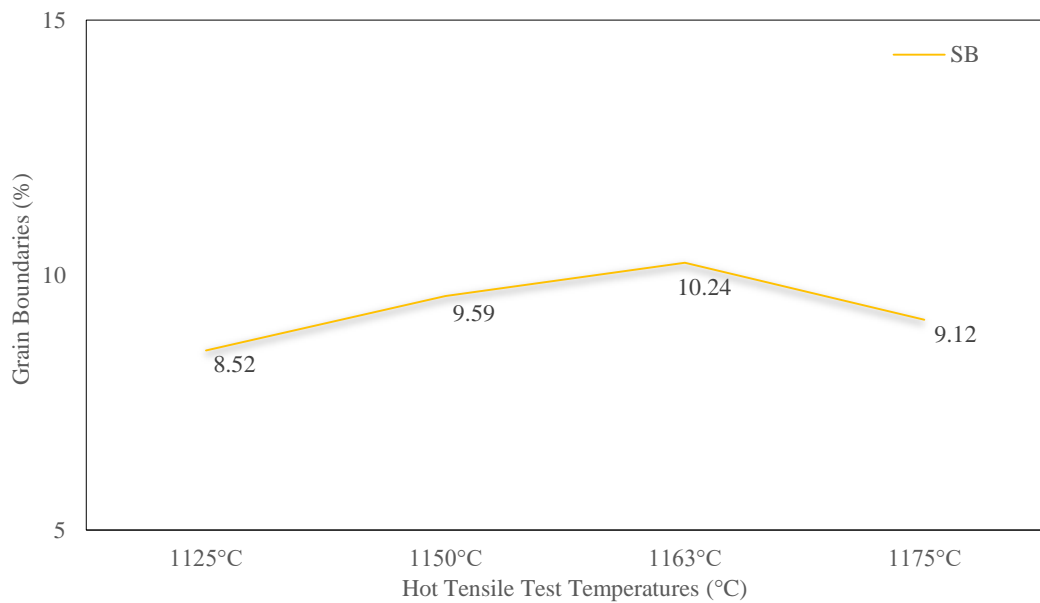


Figure 4.48. SB (%) vs hot tensile test temperatures (°C)

The findings indicate that dislocation substructures develop more extensively as the temperature increases from 1125°C to 1163°C, suggesting that higher temperatures promote the formation of these substructures rather than the formation of DRXed grains. This is because, despite the strain being significantly greater than the critical strain, the deformation process occurred very quickly at the high strain rate ( $10 \text{ s}^{-1}$ ), leading to microstructural inhomogeneity [102]. As a result, the original grains may not have recrystallized at 1150°C and higher temperatures for these conditions.

#### **4.2.2.2 Subsurface Average Grain Size Measurement Using Optical Microscope**

To determine the average grain size, the linear intercept method was applied according to ASTM E112-10 “Standard Test Methods for Determining Average Grain Size” [103]. Initially, to evaluate whether there was any variation in grain distribution across the cross-section, 10 micrographs were taken from samples tested at 7 different tensile test temperatures under an optical microscope. Since no significant difference in grain distribution was observed across the cross-section, 4 micrographs were then taken at equal intervals and distances from the surface inward.

4 micrographs, taken at equal intervals for each sample with an optical microscope, were analyzed in the ImageJ software by drawing 5 intercepts (horizontal straight lines), and the grain boundary intersection counts were calculated. Small grains, believed to have formed recently at grain boundaries, were excluded from the calculation when using the grain boundary intersection count method in ImageJ, as their inclusion would reduce the average grain size.

Average grain size measurements from the subsurfaces of fractured surfaces were calculated as shown in Figure 4.49.

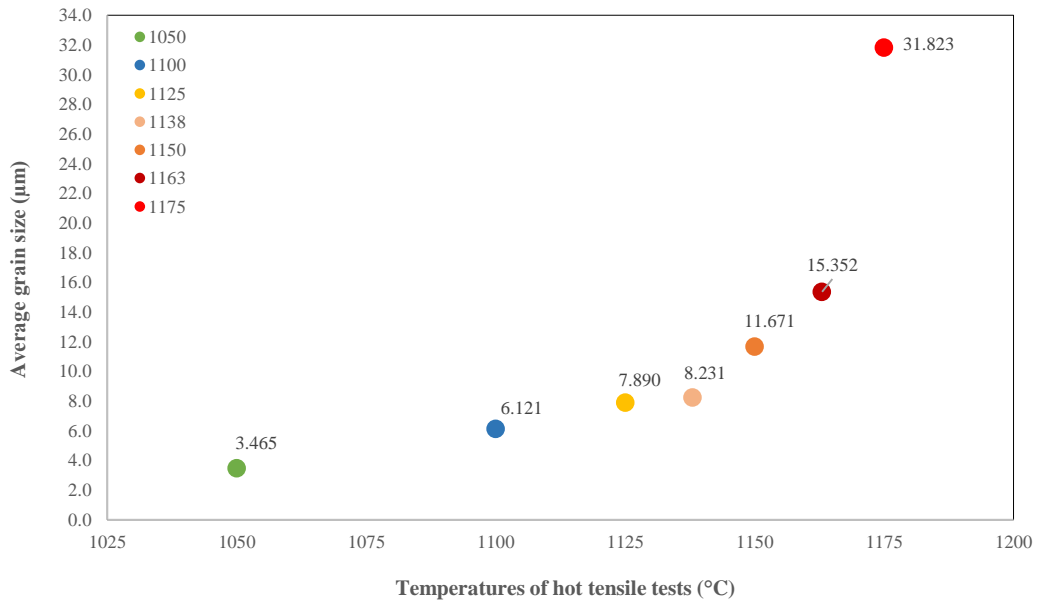


Figure 4.49. Average grain size ( $\mu\text{m}$ ) vs hot tensile test temperatures ( $^{\circ}\text{C}$ )

#### 4.2.2.3 Subsurface Microhardness Measurement

The microhardness test was performed using a KB Prüftechnik GmbH Vickers microhardness tester (KB 30 S model) with a load of 1 kg applied to mechanically ground and polished subsurfaces. The average microhardness value was determined from five indentations made on both the core and outer surfaces of the samples, with subsurface examination of the fractured surface. The averages of five microhardness measurements taken from the surface and core regions of the test samples after hot tensile tests are presented in Table 4.13 and plotted in Figure 4.50 below.

Table 4.12 Microhardness Measurements from Hot Tensile Tests Samples

Hot Tensile Test Temperature(°C)	Surface Hardness HV(1)	Core Hardness HV(1)	Total HV(1)
1050	892.75	859.5	876.12
1100	860.5	835	847.75
1125	831.5	816	823.75
1138	828.5	795.5	812
1150	822	796	809
1163	814	799	806.5
1175	799	757.5	778.25

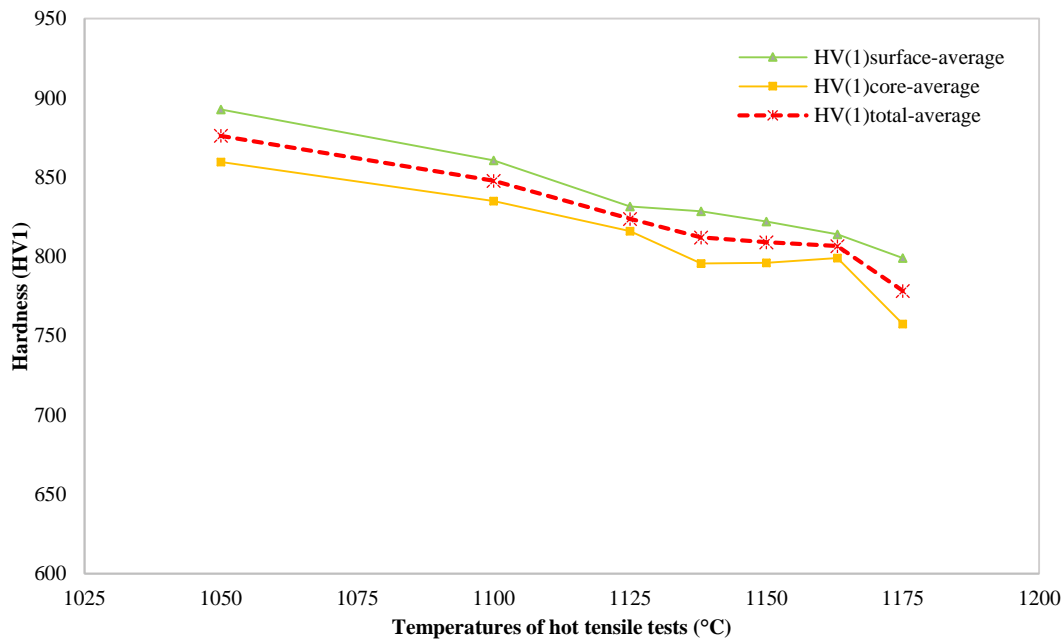


Figure 4.50. Hardness measurement (HV1) from subsurfaces

When Figure 4.50 is examined, it can be seen that the core of the tensile test sample exhibits lower hardness than the surface. This is likely due to thermal gradients during hot tensile testing, which cause the surface to cool more rapidly than the core,

promoting the formation of harder microstructures at the surface. Additionally, fine grains have higher microhardness compared to coarse grains. Thus, the microhardness results correlate with the average grain size measurements shown in Figure 4.49 after hot tensile tests.

The hardness of the as-received M50 steel bar was measured around 200 HV1. As the temperature increased up to 1150°C (from 1050°C to 1150°C), the hardness decreased. At 1150°C and 1163°C, the microhardness remained approximately the same. Finally, at 1175°C, the lowest hardness value was recorded due to the disappearance of grain boundaries.

#### 4.2.2.4 Subsurface Retained Austenite (%) Measurement

The retained austenite content of the samples after the hot tensile tests was measured using the Seifert X-Ray Diffractometer (XRD) 3003 PTS. The corresponding XRD system is illustrated in Figure 4.51.

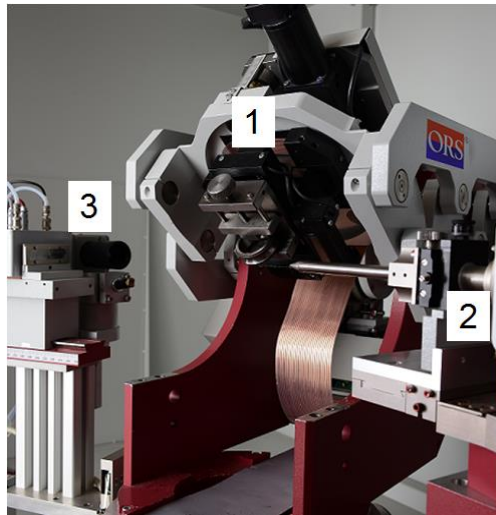


Figure 4.51. X-Ray Diffractometer (XRD) (1) goniometer, (2) x-ray generator tube and (3) position sensitive detector

As shown in Figure 4.51, the X-ray generator tube, X-ray detector, and 7-axis goniometer are the primary components of this system. The X-rays, generated by the

Cr tube, are directed to the specimens through a collimator. Additionally, a Position Sensitive Detector was employed in the system to collect the diffracted X-rays from the measurement point. The measurement parameters for the XRD analysis are provided in Table 4.13.

Table 4.13 XRD Measurement Parameters

Collimator	1.5 mm
Number of Scans	4
Scan Ranges	102.00-168.00
Step Width	0.02
Time	24 min
Scan Axis	2:1 Absolute
Scan Mode	Stepscan

Cooling from the austenitization temperature results in a microstructure composed of untempered martensite, a certain amount of retained austenite, and carbides that remain undissolved [104]. As mentioned in Section 2.1.2 of this study, M50 contains both significant primary carbides and smaller carbides, comprising approximately 12 vol% of the overall material [6-7]. Since the total duration of the hot tensile tests conducted with Gleeble, from start to finish, was approximately 4 minutes, it was assumed that the carbides remained incompletely dissolved at these tests temperatures. Therefore, retained austenite measurements were conducted in accordance with the relevant standard [105], using a carbide amount of 12%.

The retained austenite measurements from the subsurfaces of fractured surfaces were calculated as given in Table 4.14.



Table 4.14 Retained Austenite (%) vs Hot Tensile Test Temperatures (°C)

<b>Hot Tensile Tests Temperatures (°C)</b>	<b>Retained Austenite (%)</b>
1050	8.0 (±2.5)
1100	7.2 (±0.8)
1125	5.9 (±0.9)
1138	8.2 (±1.6)
1150	7.5 (±1.2)
1163	5.9 (±0.6)
1175	6.4 (±0.2)

The crystal structure and lattice parameters of martensite, ferrite, and retained austenite vary, with retained austenite exhibiting distinct differences from martensite and ferrite. Moreover, martensite has a higher concentration of lattice defects, such as dislocations, than ferrite. As a result, EBSD analysis effectively and easily distinguishes these three phases [106]. In light of this study, EBSD analysis outputs were also utilized to validate the retained austenite results obtained through XRD measurements.

Upon examining the EBSD results of subsurface specimens after hot tensile tests at 1125°C, 1150°C, 1163°C, and 1175°C, retained austenite with its Face-Centered Cubic (FCC) structure is highlighted in blue, while martensite and ferrite with Body-Centered Cubic (BCC) structures are shown in red in Figure 4.52. Additionally, Table 4.15 provides the phase fractions of these phases in samples following hot tensile tests.

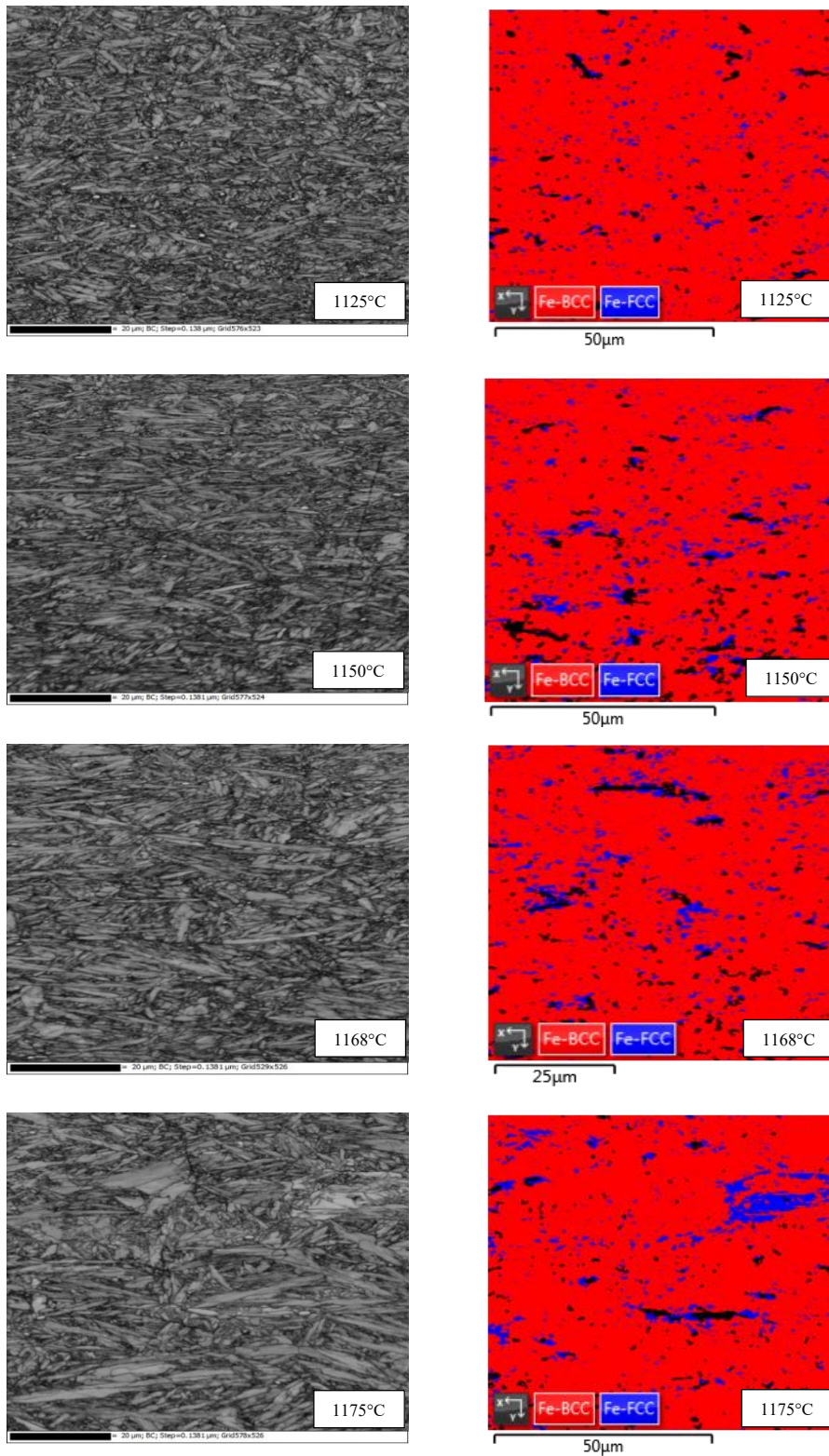


Figure 4.52. EBSD analyses of microstructures after hot tensile tests (left) BC image (right) phase map

Table 4.15 Phase Fractions (%) of the Sub-surfaces from Hot Tensile Tests

Phase Name	Phase Fraction (%)			
	1125°C	1150°C	1168°C	1175°C
<b>Fe-BCC</b>	93.67	88.55	89.48	89.90
<b>Fe-FCC</b>	3.54	5.89	6.35	7.16
<b>Zero Solutions</b>	2.79	5.56	4.17	2.94

The values provided in Table 4.15 for EBSD are also depicted together with the XRD measurement results, along with tolerance values, are shown in Figure 4.53. Based on the X-ray linear absorption model, the data obtained from the X-ray measurement penetrates sufficiently to examine the bulk phases, with minimal surface effects in the quantification analysis performed using the XRD technique. Therefore, XRD measurements are less affected by variations in surface finishing methods when determining the retained austenite amount. In contrast, because the EBSD technique is sensitive to surface characteristics, the method of sample preparation has a direct impact on the results. Indeed, EBSD analyses validate that quantification is dependent on the sample preparation approach [107].

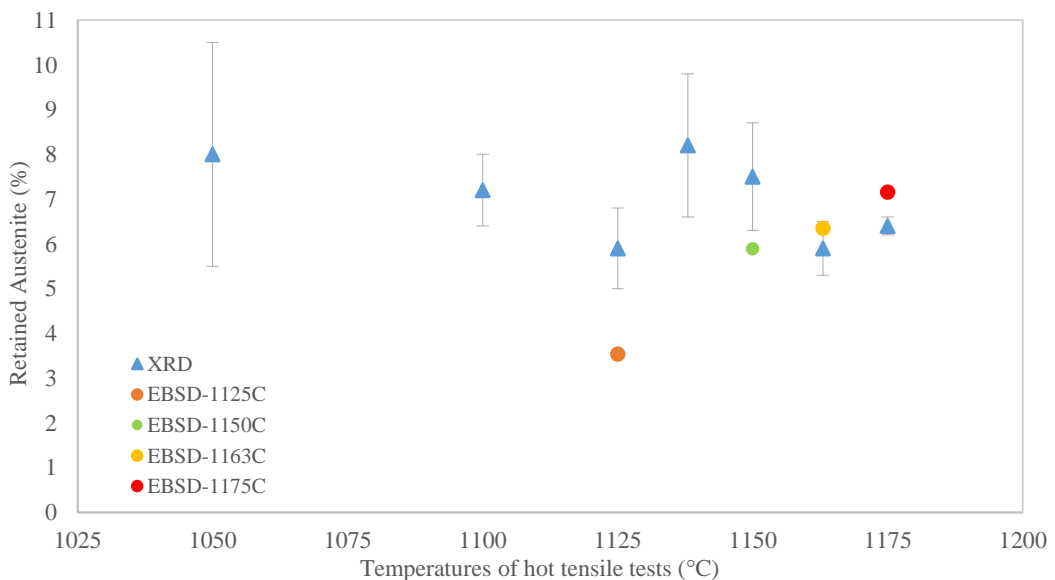


Figure 4.53. Retained austenite (%) amounts measured by XRD and EBSD

Based on the comparison shown in Figure 4.53, it can be inferred that the difference between the Fe-FCC values obtained from EBSD and the retained austenite results from XRD is likely due to differences in sample preparation.

### **4.3 Summary and Conclusion**

In this chapter, a thorough examination of the metallurgical reasons behind the temperature-dependent behaviour of the  $LC_n$  damage criterion was provided. The study analyzed both the as-received microstructures and those observed after hot tensile testing of M50 steel. These analyses were conducted using an optical microscope (OM), a stereo microscope (SM), and primarily a scanning electron microscope (SEM), along with its EDS (Energy Dispersive Spectroscopy) and EBSD (Electron Backscatter Diffraction) capabilities, to provide detailed insights into the thermal processes affecting M50 steel.

As a result of the studies, it was observed that the as-received microstructure of M50 bearing steel is remarkably homogeneous and closely matches the observations documented in the literature. Below 1150°C (at 1050°C, 1100°C, 1125°C, and 1138°C), M50 steel displayed typical characteristics of ductile fracture. Upon reaching 1150°C, a shift from ductile fracture to intergranular fracture was noted, which was linked to a decrease in ductility. In summary, a detailed analysis of fracture morphology suggests that 1150°C can be considered the equi-cohesive temperature for M50, where fractures occurring below this temperature are transgranular, and those above it are intergranular, as shown in Figure 4.54.

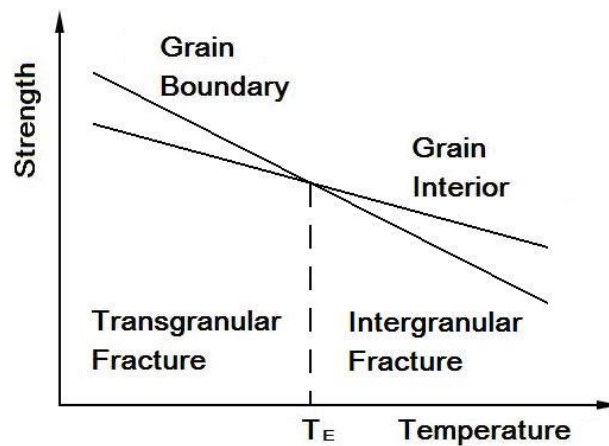


Figure 4.54. Illustration of the equi-cohesive temperature ( $T_E$ ) [95]

This observation supports the conclusion obtained at the end of Chapter 3, where it was determined that an  $LC_n$  criterion of “2” was selected for temperatures up to 1150°C, while a criterion of “1” was chosen for temperatures exceeding this threshold. Additionally, it was concluded that the reduction of area declined from around 90% to 70%, while fracture strains decreased from 70% to approximately 55% as the temperature increased to 1150°C. Consequently, it became apparent that the plasticity of M50 steel under tensile loading diminished beyond 1150°C, with the subsurface microstructure examination showing consistency with the macrostructure examination of the fracture morphology.



## CHAPTER 5

### FINITE ELEMENT ANALYSIS OF DAMAGE CHARACTERISTICS IN HOT FORGING PROCESS OF M50 BEARING RINGS

The hot forging process is crucial in bearing production. Due to significant deformation that materials experience during the hot forging process, damage evolves, affecting both the material and the process, and ultimately influencing the properties of the final product. Therefore, this chapter investigates the evolution of damage during the multi-stage hot forging of M50 steel bearing rings.

The unique properties of M50, derived from its alloying elements and carbides, impose specific constraints on the hot forging process, restricting it to a particular range. Hence, accurately representing and incorporating damage in finite element simulations is essential for designing and executing the process effectively.

#### 5.1 Simulation of Hot Forging of Bearing Rings

The multi-stage hot forging process simulation for M50 steel was performed using Forge NxT 3.2® after calculating the set value for the  $LC_n$  damage criterion in Chapter 3.

The forging process involves four stages: upsetting, closed-die forging, and two shearing stages for ring separation and scrap removal from the inner ring. In this chapter, the hot forging process for bearing rings was simulated and analyzed using a thermo-mechanical, two-dimensional axisymmetric numerical model with an implicit time integration scheme. Furthermore, software analysis of accumulated damage between the hot forging stages was conducted, considering that damage evolution correlates with void nucleation, growth, and coalescence, resulting in micro-crack formation.



### **5.1.1 Modelling and Simulation of Upsetting, Forming and Shearing Processes**

In hot forming processes, viscoplastic behaviour is predominantly utilized due to the minor influence of elasticity compared to viscoplasticity at elevated temperatures, as discussed in “3.3 Modelling Material Behaviour”. In this context, Forge NxT 3.2® simulation software utilizes rigid viscoplastic behaviour, a standard for hot-worked metals, incorporating the Hänsel-Spittel isotropic strain hardening model. It employs the Von Mises yield criterion with an associated flow rule and applies regularization to address initial flow curve inconsistencies. The  $LC_n$  damage criteria remain independent of the constitutive law until the element is removed upon reaching the threshold value [81].

In the simulation of hot forging processes, the finite element model was developed by integrating three critical components for each stage: the billet, upper die, and lower die. Initially, the M50 billet had a diameter of 45 mm. Following trials, the billet length was adjusted to 42.2 mm to ensure complete die filling at the forming station.

The hot forging process was simulated at four different temperatures; 1100°C, 1150°C, 1175°C and 1200°C with non-isothermal conditions. While the upper die was selected as a mechanical press, the lower die was set as stationary, and both forging presses were modeled as analytical rigid bodies. In order to move the upper die in the -z direction, zero displacement was applied in the x and y directions. The crank driving the upper die (mechanical press) was set at 80 rpm in terms of rotational speed for upsetting, forming, and shearing operations, as shown in Figure 5.1 for each operation.

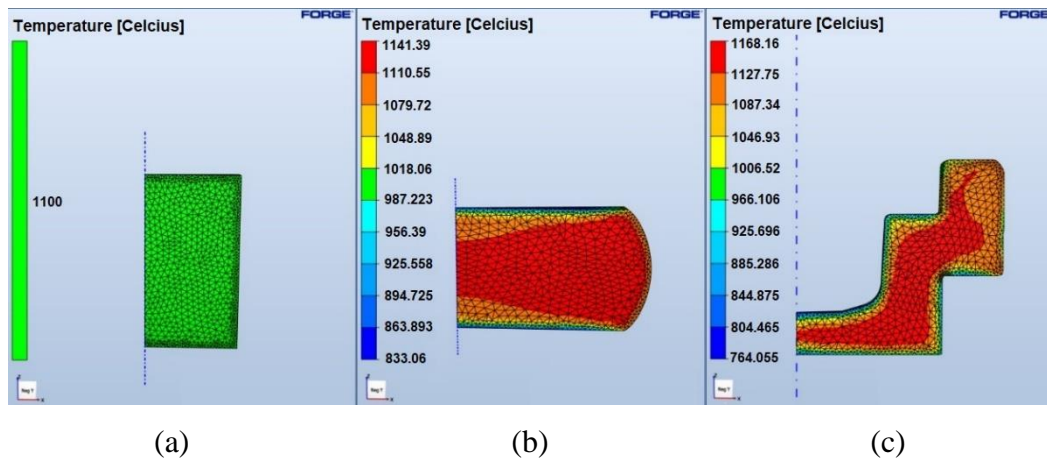


Figure 5.1. (a) Initial M50 billet at the end of (b) upsetting (c) forming processes

Variations in temperature within a physical system result from the interaction between internal heat conduction and dissipation processes, which are affected by boundary stresses. These stresses depend on factors such as heat transfer mechanisms (radiation, conduction, convection, etc.) or externally imposed temperature conditions. This is represented by the heat equation implemented in Forge NxT 3.2® software, incorporating boundary conditions that encompass parameters such as plastic strain, specific heat capacity, thermal conductivity and density. Thermomechanical coupling is achieved by adjusting the rheological parameters based on the temperature values calculated at each time step, using a strain hardening-thermal rheology model. In the context of an interface involving heat transfer, assessing the conduction phenomenon necessitates understanding both the heat transfer coefficient between the die and the material and the die's temperature [81]. In this setting, the die temperatures of both the upper and lower dies during upsetting, forming, and shearing operations were set to 150°C, corresponding to the operational temperature of the forging machine used in the experimental forging trials. The die temperature for forging on this particular machine was previously established by Arbak et al [108]. Furthermore, for thermal interactions between the billet, lower die, and upper die in hot forging simulations, the Forge software offers various options. To precisely model our forging trials, the option for “strong

interaction with steel dies” was chosen, with the heat transfer coefficient set at 20.000 W/m<sup>2</sup>K. The option for “heat transfer with air” was selected for the ambient medium, with the heat transfer coefficient set to 10 W/m<sup>2</sup>K. To guarantee precise heat transfer calculations in the hot forging simulation in Forge software, the thermal contact settings were chosen as illustrated in Figure 5.2 and Figure 5.3.

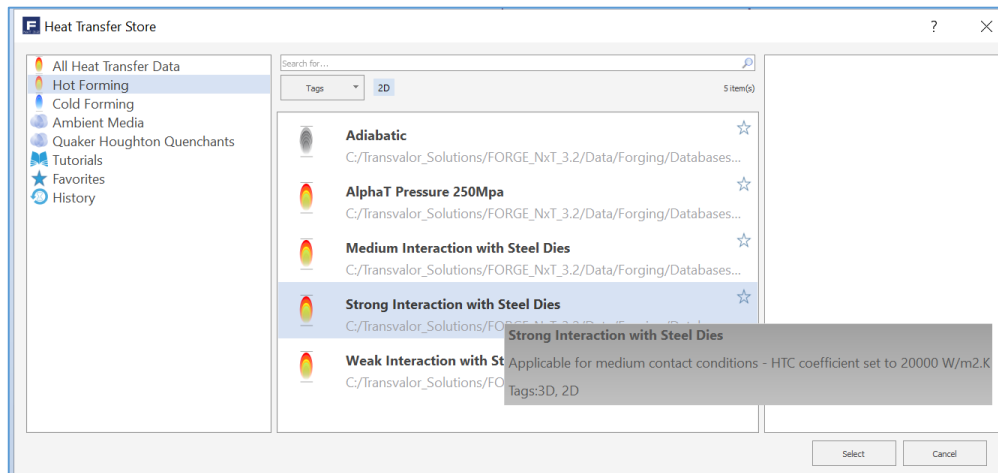


Figure 5.2. The considered thermal contact between billet with upper/lower dies

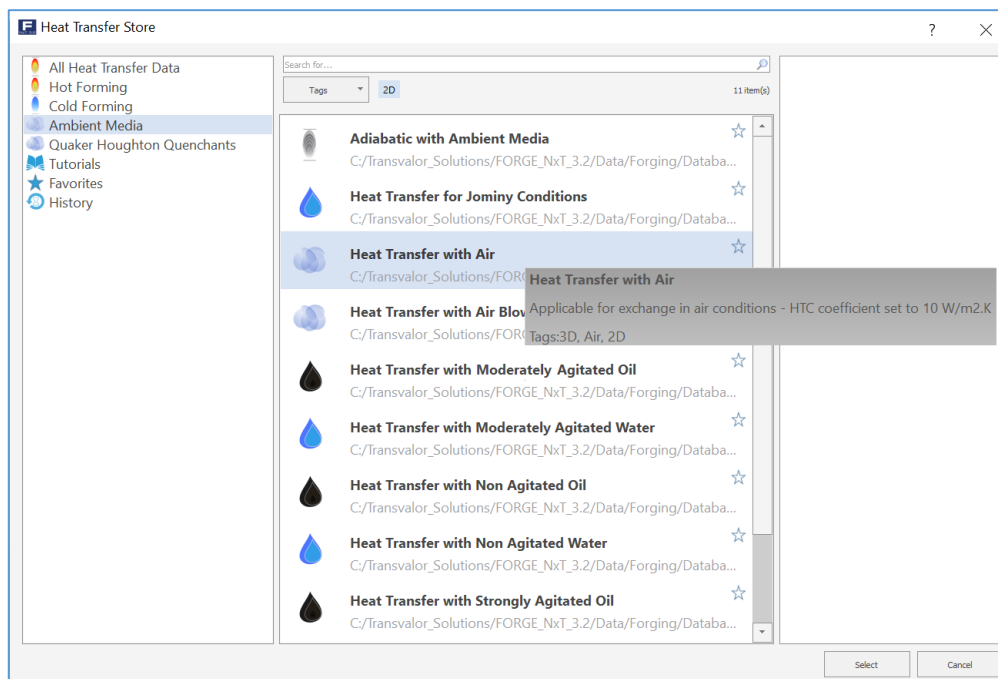


Figure 5.3. The considered thermal contact with ambient medium

Additionally, the Coulomb limited by Tresca model (with values of Coulomb friction coefficient  $\mu = 0.4$  and Tresca friction coefficient of  $m = 0.8$ ), a built-in viscoplastic shear friction model, was chosen as the friction law under no lubrication conditions in the hot forging processes simulated using Forge NxT 3.2® software [81]. The shear friction coefficient value was assigned as 0.77 to represent the no-lubrication conditions at the interface between the billet and the forging tools. A triangular mesh with 0.5 mm, 1 mm, and 2 mm element sizes was applied to the billet, and finally, the process continued with a 1 mm mesh size as it was evaluated to be the most effective in terms of analysis time and evaluation criteria.

### **5.1.2 Shearing Length Determination**

Following the upsetting and forming processes, the inner and outer rings were produced and subsequently conveyed to the shearing process. To separate the outer ring and inner ring, a shearing process was conducted after the forming process, and several experiments were carried out to simulate the shearing stage. Remeshing was used for models with large plastic deformations. Therefore, remeshing was activated for the shearing model in addition to the triangular meshing with a 1 mm element size on the billet.

Within the scope of the mesh sensitivity studies, remeshing boxes with 0.05 mm, 0.1 mm, and 0.2 mm element sizes were examined, and finally, the 0.1 mm size was determined to be effective for the shearing area, as shown in Figure 5.4.

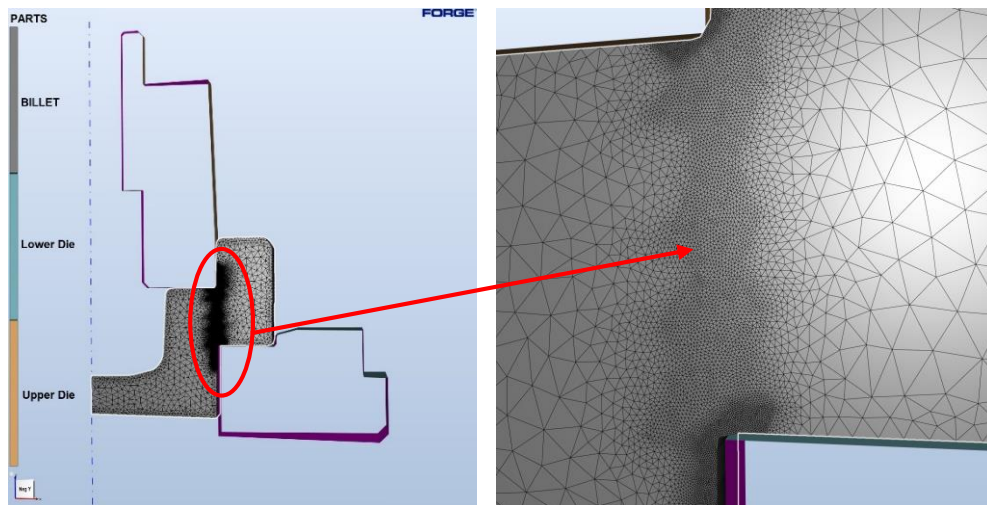


Figure 5.4. Creation of shearing area using remeshing box with 0.1 mm elements

The hot forging process was simulated at four different temperatures: 1100°C, 1150°C, 1175°C, and 1200°C under non-isothermal conditions, considering that the initial forging temperature of the part varies locally as the process progresses. Therefore, as the local temperature rises during the separation of inner and outer rings in the shearing process, it is essential to conduct a systematic assessment of the damage criterion in the cutting zone, which varies with temperature. The initial form of the billet for the shearing process in the hot forging simulation is depicted in Figure 5.5

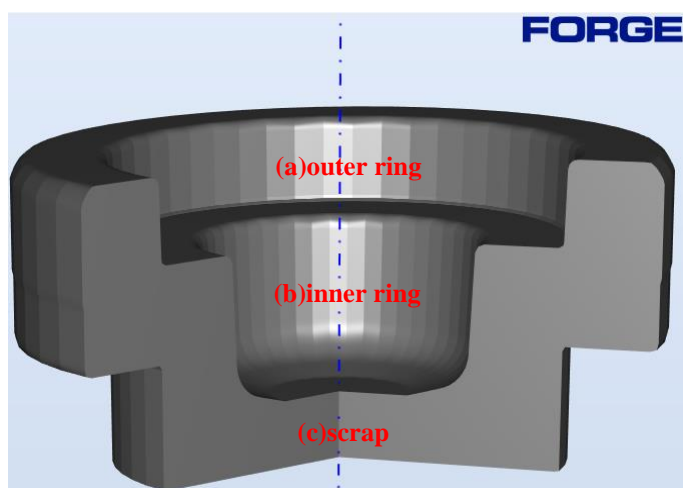
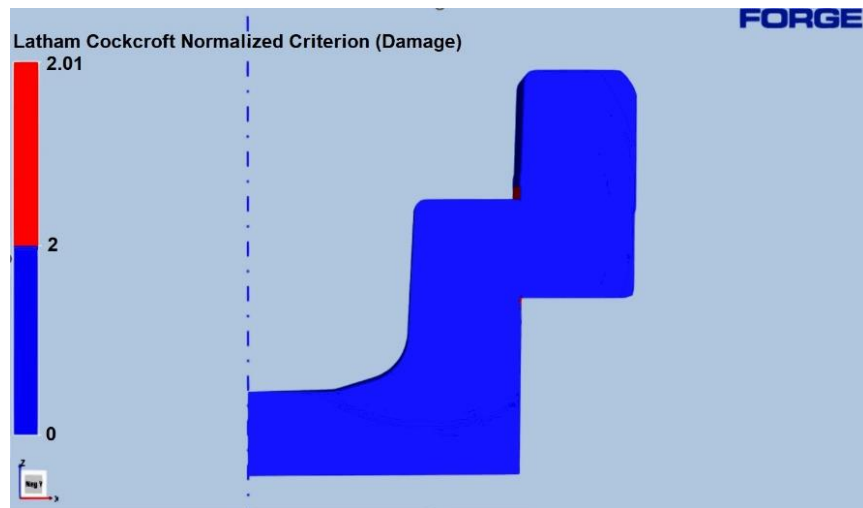
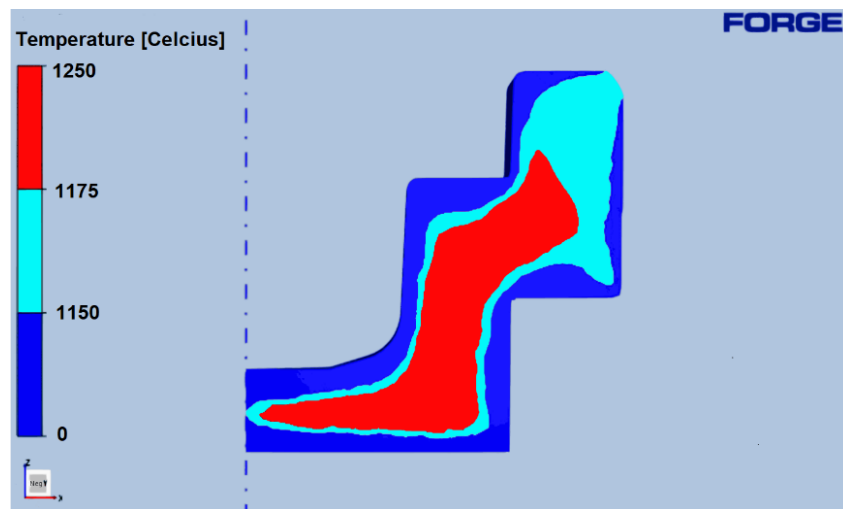


Figure 5.5. Primary billet shape for shearing process in hot forging simulation

Following the decision to use an  $LC_n$  criterion of 2 for temperatures up to 1150°C (based on the outputs obtained at the end of Chapter 3), two distinct colors were selected to facilitate the clear monitoring of both the  $LC_n$  damage criterion and temperature, illustrated in Figure 5.6.



a) Tracking with  $LC_n$



b) Tracking with temperatures

Figure 5.6. Tracking  $LC_n$  and temperature for shearing length determination

As it is given in Figure 5.6, the  $LC_n$  values ranging from “0-2” are depicted in blue, while values above “2” are shown in red. Similarly, temperatures ranging from 0°C to 1150°C are represented in blue, with temperatures above this range indicated in red. Therefore, within this context, the hot forging simulations were initially conducted with four different die clearances (0.1 mm, 0.2 mm, 0.4 mm, and 0.8 mm) and at four distinct forging start temperatures (1100°C, 1150°C, 1175°C, and 1200°C), utilizing a temperature-dependent  $LC_n$  damage criterion. Progress was measured in terms of shear length until reaching the point marked in red (above  $LC_n=2$ ).

Accordingly, the damage evaluation conducted for each forging start temperature and each die clearance is provided separately in Figure 5.7 to Figure 5.10. The critical shear limits of the billet, beyond which the die no longer performed shearing, were also marked in these tables.

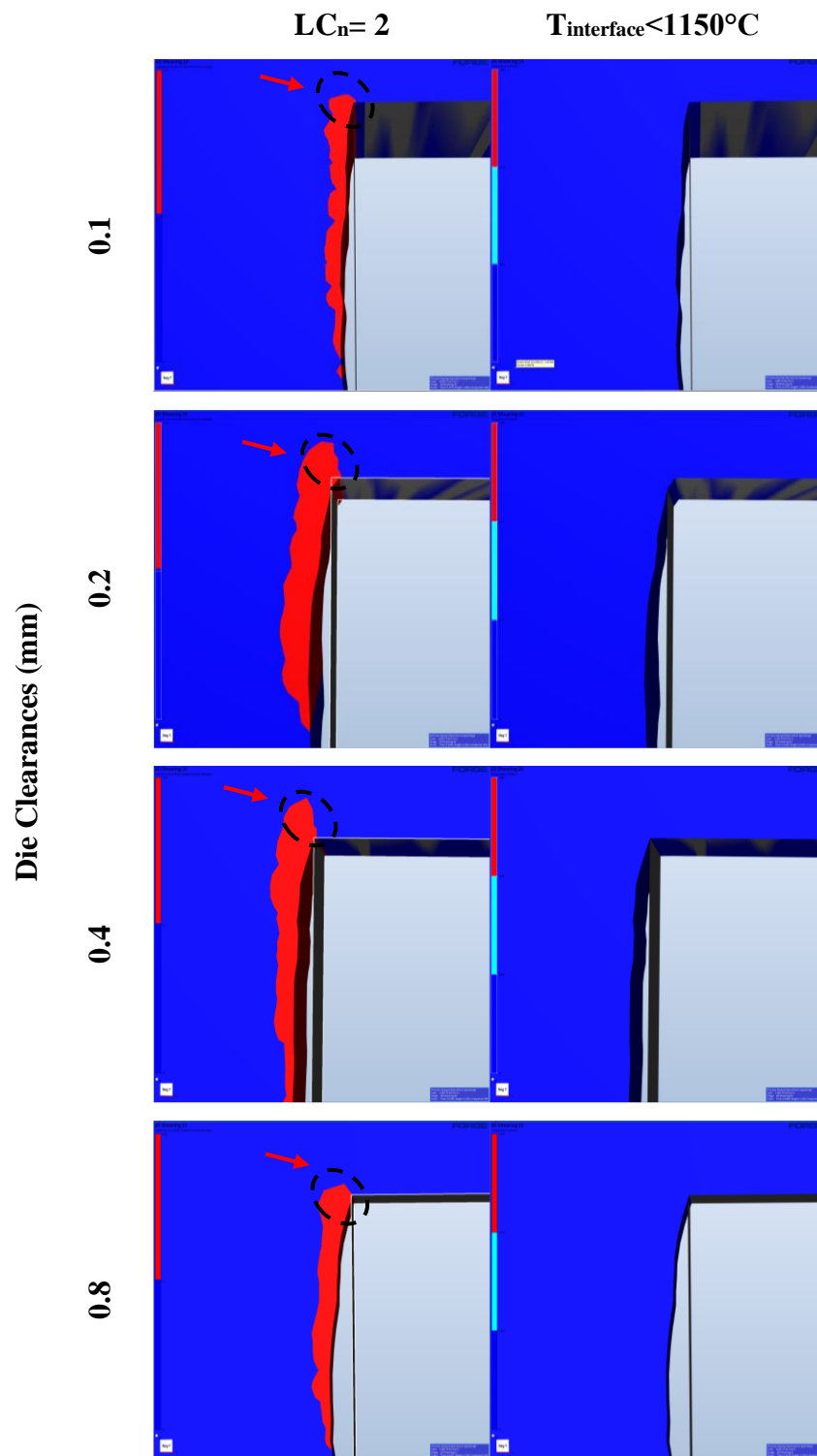


Figure 5.7. Shear Length Evaluation at  $T_{ForgingStart} = 1100^\circ C$  with  $LC_n$



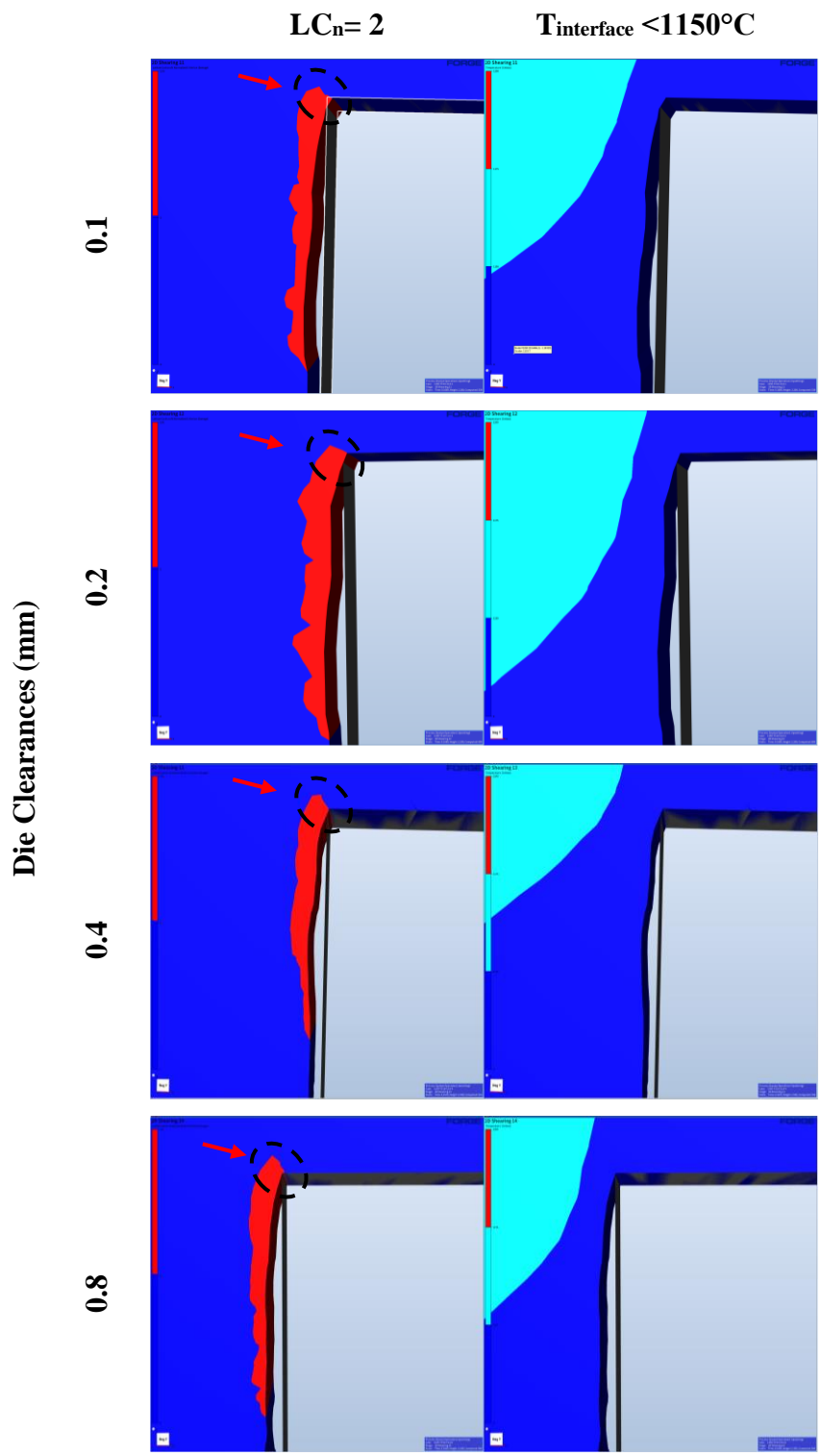


Figure 5.8. Shear Length Evaluation at  $T_{\text{ForgingStart}} = 1150^\circ\text{C}$  with  $LC_n$

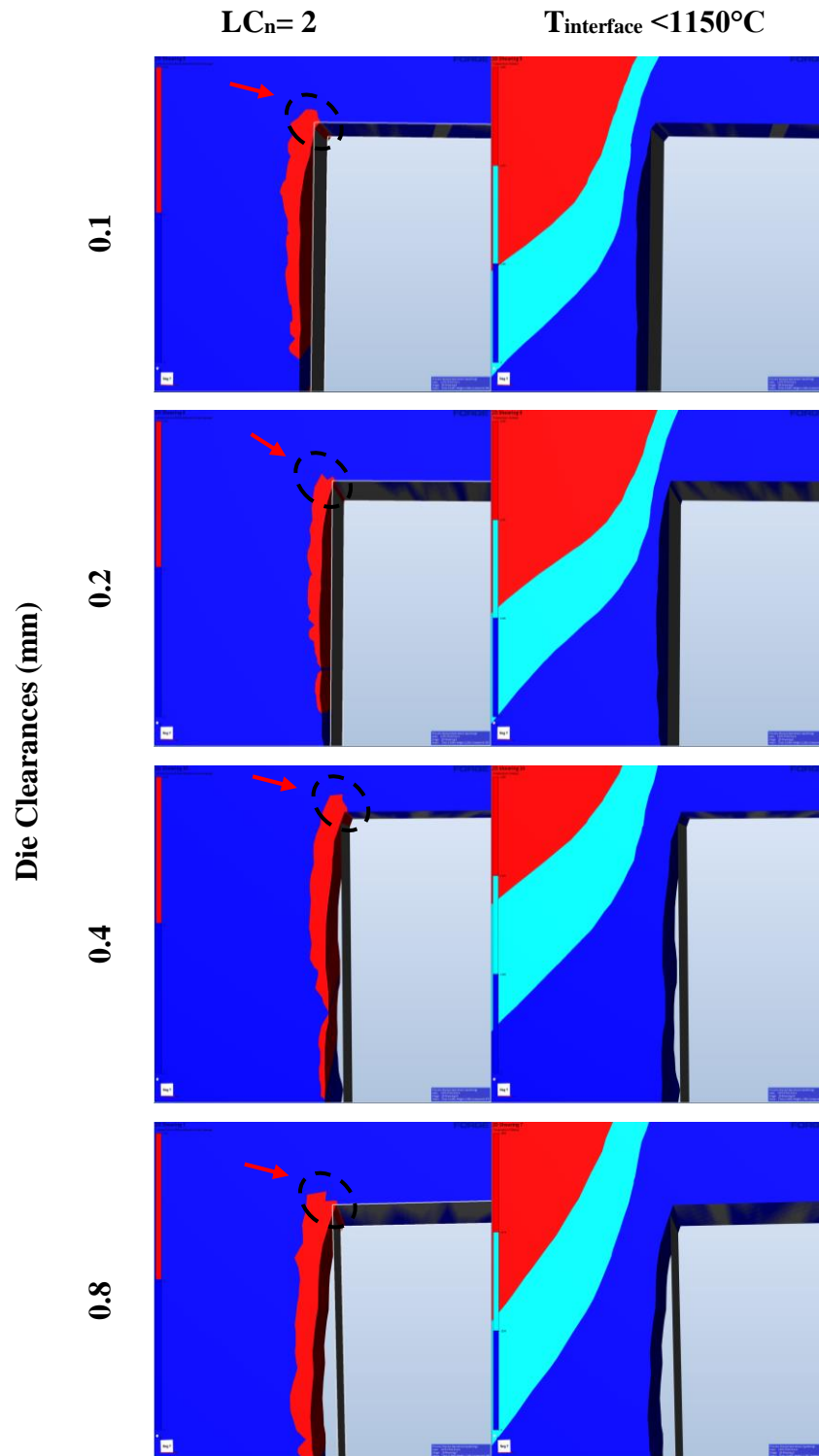


Figure 5.9. Shear Length Evaluation at  $T_{ForgingStart} = 1175^\circ C$  with  $LC_n$

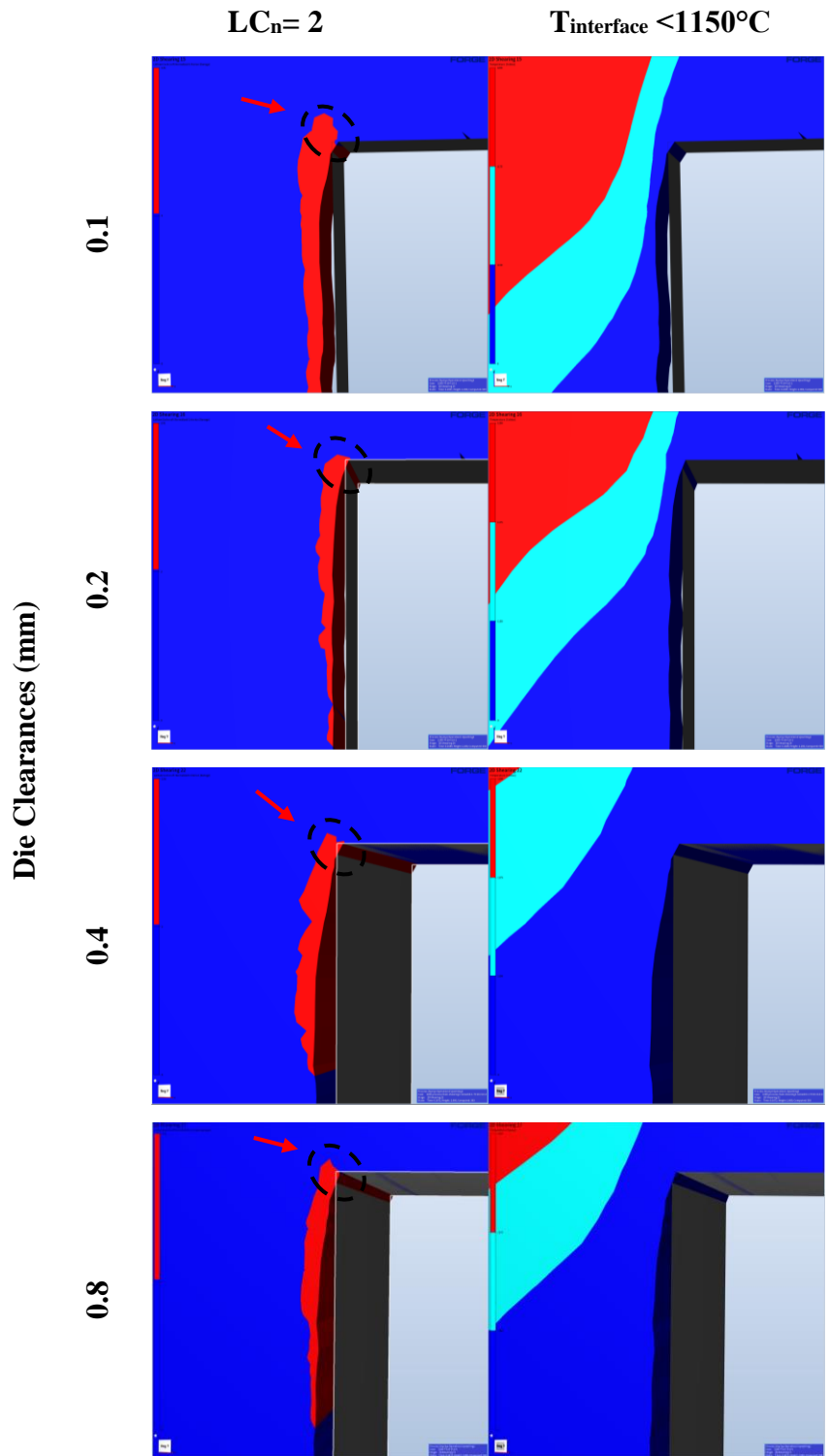


Figure 5.10. Shear Length Evaluation at  $T_{ForgingStart} = 1200^\circ C$  with  $LC_n$

It is crucial to make a decision about the shearing length at which the component can no longer be cut. For this reason, the temperature and damage criteria at the interface between the die and billet were examined in 0.1 mm increments during the shearing operation of the forging process. As the shearing process progressed, local temperature variations at the die-contacting surface were analyzed.

As seen in Figure 5.7 to Figure 5.10, across all relevant experiments, the temperature of the billet in contact with the lower die (shear zone) did not surpass 1150°C, monitored at intervals of 0.1 mm. It was noted that despite the core temperature exceeding 1150°C at each forging temperature, the temperature on the surface inspected for the shearing process remained between 1050°C and 1150°C due to contact with the die. During these intervals, the temperature consistently ranged between 1050°C and 1150°C, and  $LC_n=2$  was chosen. Consequently, the shearing length was determined by the progression within the  $LC_n$  0-2 range. Table 5.1 shows the calculated shearing length at various forging temperatures and clearances.

Table 5.1 Calculated Shearing Length at Various Forging Temperatures and Clearances

Die Clearance (mm)	Shearing Length (mm)			
	$T_{\text{Forging Start}}$			
	1100°C	1150°C	1175°C	1200°C
0.1	2.2	1.7	1.8	1.9
0.2	1.9	1.8	1.6	1.7
0.4	1.7	1.5	1.5	1.4
0.8	1.3	1.7	1.8	1.4

Table 5.1 shows that, across experiments with different clearances conducted at various forging start temperatures, the shearing length exhibited similar trends and did not increase.

Subsequently, hot forging experiments were carried out at ORS (Ortadogu Rulman Sanayi) to experimentally verify these results at temperatures of 1100°C, 1150°C, and 1200°C. These forging start temperatures, 1100°C, 1150°C, and 1200°C, were experimentally tested in the field with standard 0.4 mm die clearances. The hot forging press currently used in these experiments at ORS, which consists of four stations, is shown in Figure 5.11.

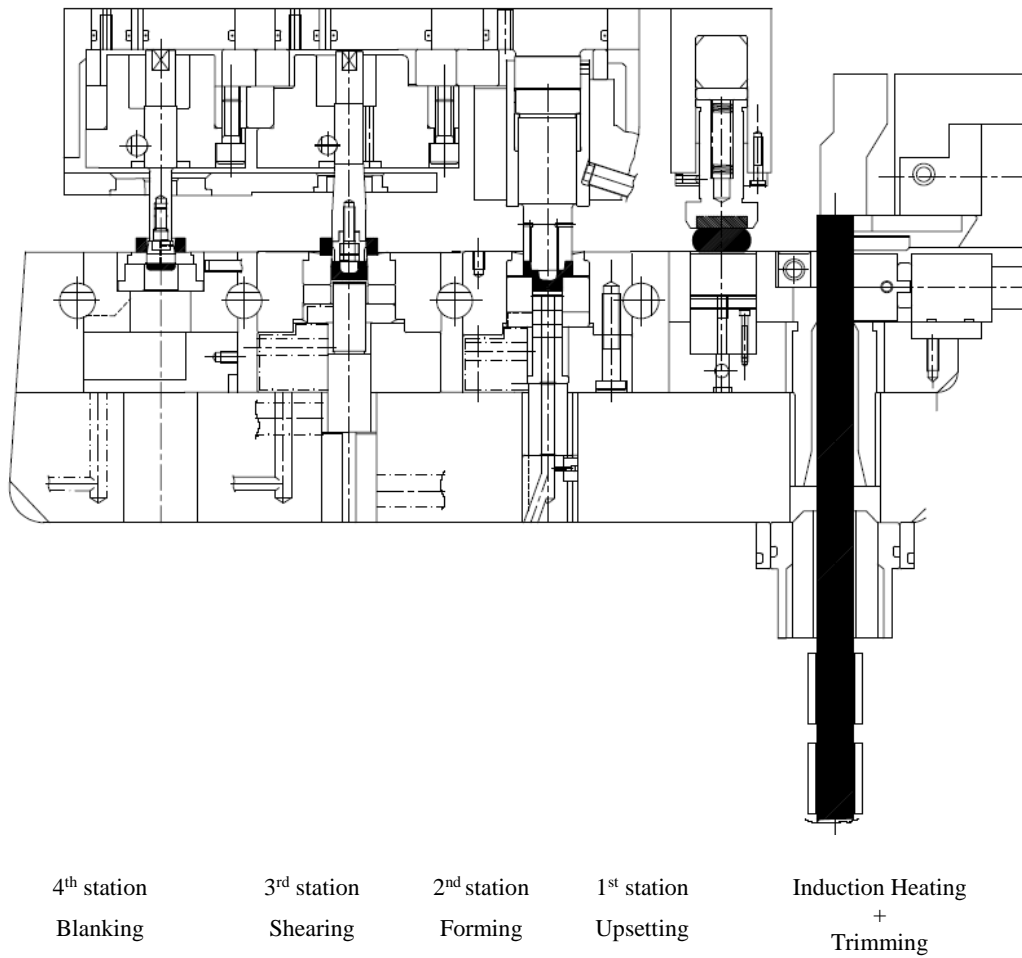


Figure 5.11. Hot forging press at ORS with 4 stations

Following the separation of the inner and outer rings as illustrated in Figure 5.12, the scrap removal (blanking) process was conducted at the 4<sup>th</sup> station of the press for each forging temperature.



Figure 5.12. Inner and outer rings after hot forging experiments at ORS with 0.4 mm die clearance

The surface characteristics observed during the hot forging experiments performed at 1100°C, 1150°C, and 1200°C, as displayed in Figure 5.12, were found to be similar. Following these experiments, the shearing process on the surfaces of the inner ring was analyzed using a stereo microscope (Carl Zeiss Stemi 2000-C Model). For reference, stereo microscope (SM) images of the inner ring surfaces from Figure 5.12 are depicted below in Figure 5.13. In Figure 5.13, the separation surface (1) and the shearing length (2) are highlighted for illustrative purposes, while Figure 5.14 and Figure 5.15 are assessed in a similar manner.

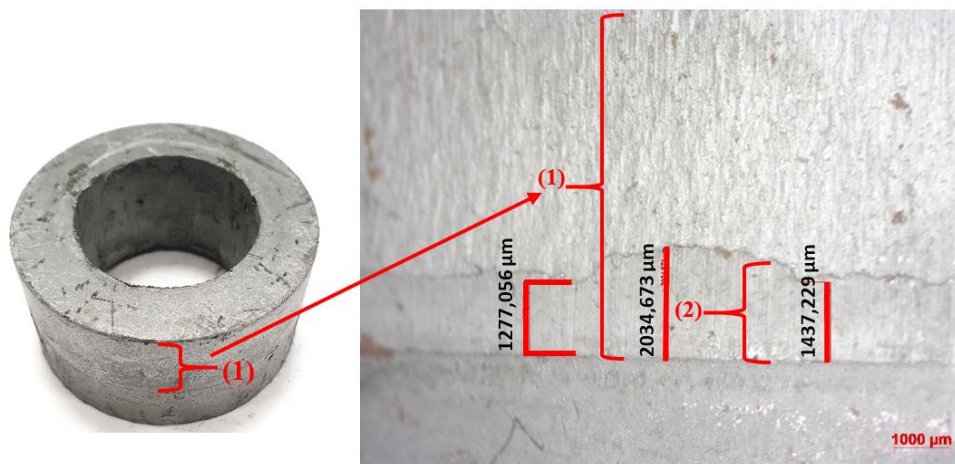


Figure 5.13. SM analysis of separation surface (1) and the shearing length (2) under SM (at 1100°C)

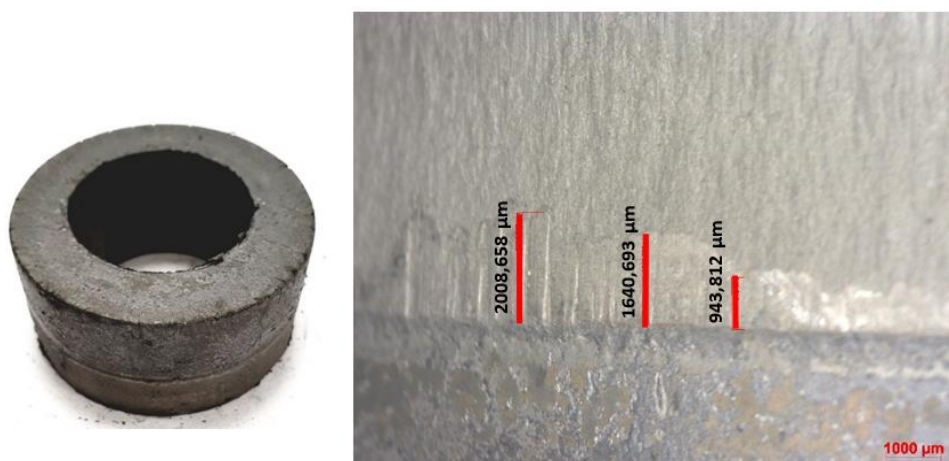


Figure 5.14. SM analysis of separation surface and the shearing length (at 1150°C)



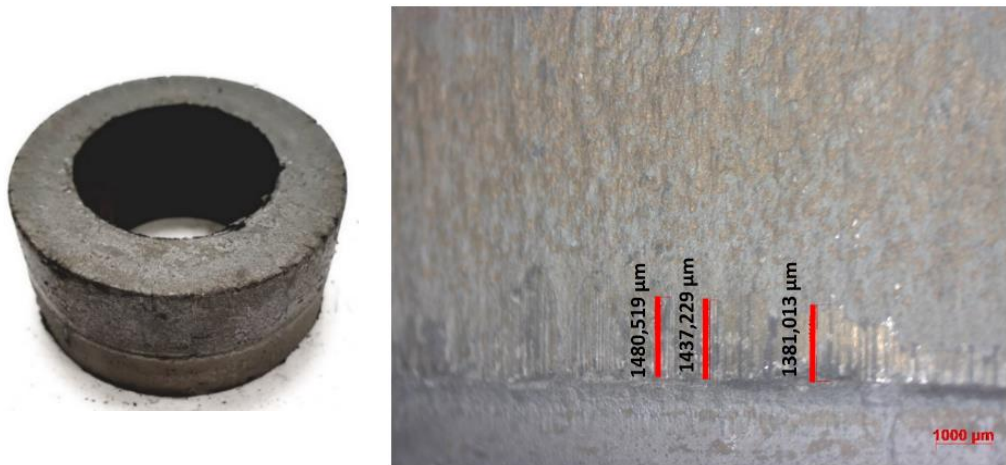
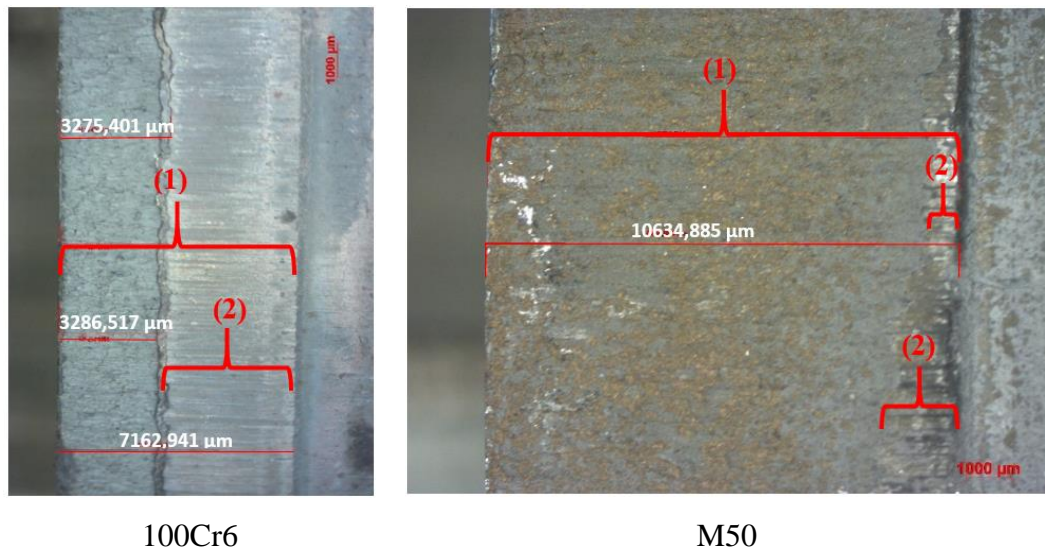


Figure 5.15. SM analysis of separation surface and the shearing length (at 1200°C)

During the shearing process, fractures appear at the points where shearing cannot proceed further. To better understand this phenomenon, the surface appearance after the shearing stage in the hot forging process of 100Cr6, a material commonly used in standard bearing manufacturing, was compared with the surface features of M50 material post-shearing, as shown in Figure 5.16.



100Cr6

M50

Figure 5.16. Examination of separation surfaces on 100Cr6 and M50 rings:

(a) separation surface on ring, (b) shearing length



In the forging experiments conducted at 1100°C, 1150°C, and 1200°C with a clearance of 0.4 mm, Figure 5.12 provides illustrative depictions of the ring specimens, while Figure 5.13 to Figure 5.15 offer a detailed analysis of the surface shear. The inner ring shearing lengths at three distinct points were measured using a stereo microscope. The average shearing length, obtained from these three locations, was subsequently compared with the simulation outcomes, which are displayed in Table 5.2.

Table 5.2 Shearing Length Comparison: Simulation vs. Experimental Results

Results	Shearing Length (mm)		
	T <sub>Forging Start</sub> 1100°C	T <sub>Forging Start</sub> 1150°C	T <sub>Forging Start</sub> 1200°C
<b>Simulation</b>	1.7	1.5	1.4
<b>Experiment</b>	≈1.6	≈1.5	≈1.4

By comparing these results, it was noted that the shear length exhibited a trend consistent with the values provided in Table 5.1. As highlighted earlier, the shearing process was progressively advanced in increments of 0.1 mm to pinpoint the onset of damage and establish the limit beyond which no further shear progression would occur in simulations. Consequently, while comparable shearing lengths were observed at 1150°C and 1200°C, the discrepancy of 0.1 mm (≈6%) at 1100°C may stem from the variation between stereo microscope measurements and the 0.1 mm increments used in the simulation analysis.

Despite achieving comparable shearing lengths with variations in temperature and die clearance, alternatives were investigated to increase the shear length. Initially, adjustments were made to the press speed of the shearing process. To assess the impact of the crank driving the upper die on cutting length in the shearing process, additional simulations were performed at 1150°C with a 0.4 mm die clearance. These included the initial experiment at 80 rpm, as well as simulations at 30 rpm, 100 rpm.

The shear lengths were compared, as illustrated in Table 5.3; however, no increase in cutting length due to changes in speed was observed.

Table 5.3 Effect of Press Speed on Shearing Length (Upper Die)

Speed (rpm)	Shearing Length (mm)
30	1.2
80	1.5
100	1.5

Subsequently, similar experiments were performed by adding radii to both the upper and lower dies. Additional simulation iterations were then performed to evaluate these alternatives. These experiments were conducted at a forging initiation temperature of 1150°C, with the results presented in Table 5.4.

Table 5.4 Effect of Die Radius Changes on Shearing Length

Speed (rpm)	Upper Die Radius	Lower Die Radius	Shearing Length (mm)
30	0.5	0.5	2.25
80	0.5	0.5	2.5

The influence of hydrostatic pressure on fracture has been comprehensively examined in the literature [109-111]. To increase hydrostatic pressure and generate circumferential stress in the shearing zone upon contact with the die corners, the upper die was shaped with various (3°, 5°, 8°) conical angles. Following this modification, shear process simulations were reinitiated. For visual illustration, Figure 5.17 shows the upper die designed with an 8° conical angle and the corresponding redesigned lower die for simulation.

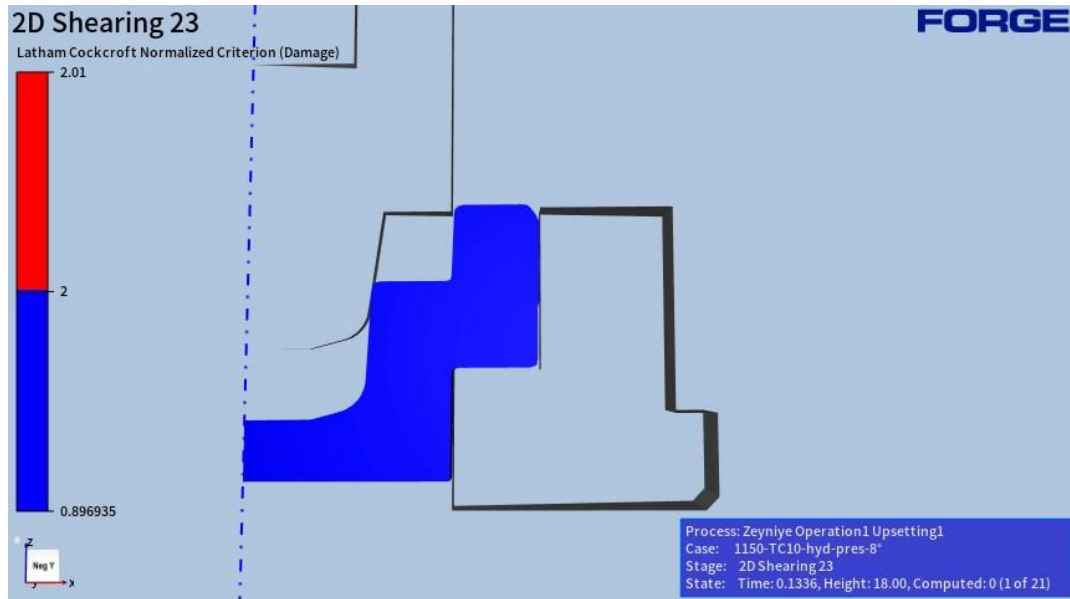


Figure 5.17. The upper die designed with an 8° conical angle

This series of experiments was performed at a forging initiation temperature of 1150°C, with the results detailed in Table 5.5.

Table 5.5 Effect of Conically Shaped Upper Die on Shearing Length

Conically Shaped Angles (°)	Shearing Length (mm)
3	1.4
5	1.2
8	1

To investigate the impact of die geometry on shearing, radii and conical shapes at various angles were applied to the tool edges in contact with the die's corners. As

shown in Table 5.5, shear lengths were compared with those in Table 5.1; however, no noticeable effects of the radii on increasing the shearing length were detected.

## **5.2 Summary and Conclusion**

This chapter of the thesis specifically focused on the shearing stage in hot forging processes, where a precise and smooth shear surface was essential. As a result of the simulation analyses conducted on the shearing process, similar trends in cutting lengths were observed and no increase in shearing length was achieved.

To experimentally validate the simulation results, forging start temperatures of 1100°C, 1150°C, and 1200°C were tested in the field using standard 0.4 mm die clearances. In this way, the experiments were conducted in real-world conditions as well, not only in a simulated environment. When analyzing the surface features of on-site trials conducted at various forging temperatures using a 0.4 mm die clearance, it was observed that they demonstrated consistent trends in cutting lengths similar to those seen in simulations conducted with the same die clearance and temperatures. This underscores the accuracy and reliability of the corresponding the hot forging simulations for M50. It is believed that the existing experiments, conducted at three forging temperatures, are sufficient to capture the phenomenon and trend and to validate the simulations.



## CHAPTER 6

### CONCLUSIONS

This study examined the damage progression during multi-stage hot forging of M50 steel bearing rings, addressing a notable gap in the literature by providing significant insights into the finite element analysis of damage characteristics in the hot forging process of M50 steel. Additionally, the microstructural evolution of the thermal deformation behaviour of M50 steel was investigated to obtain a detailed explanation of the metallurgical reasons behind this damage behaviour. The key conclusions are summarized below:

1. Hot compression tests were conducted using the Gleeble 3800 at four distinct temperatures (1000°C, 1050°C, 1100°C, and 1150°C) and three different strain rates (0.1 s<sup>-1</sup>, 1 s<sup>-1</sup>, 10 s<sup>-1</sup>). This process yielded a precise material dataset for M50 steel and established the corresponding flow curves.
2. The parameters of the Hänsel-Spittel model were calculated to study the hot deformation behaviour of M50 steel. Comparing the stress-strain curves derived from the Hänsel-Spittel equation with the experimental flow stress curves shows that the model effectively predicts the behaviour of M50 steel across different strain rates.
3. To establish the threshold value of the normalized Latham-Cockcroft criterion (LC<sub>n</sub>), experimental hot tensile tests were performed at temperatures of 1050°C, 1100°C, 1150°C, and 1200°C, with two specimens tested at each temperature. During the tensile tests at 1200°C, melting of the specimens occurred, which hindered the collection of consistent tensile stress-strain curves. Following this, the experiments were modeled numerically, and fracture strain values were analyzed based on both the hot tensile test results and the subsequent simulations. It was determined that the LC<sub>n</sub> damage criterion is a temperature-dependent material property. Therefore, an LC<sub>n</sub>

value of 2 was selected for temperatures up to 1150°C, while a value of 1 was applied for temperatures above this level.

4. The evaluation of the  $LC_n$  damage criterion as a temperature-dependent material property led to a thorough investigation into the metallurgical factors influencing the thermal behaviour of M50 steel. At temperatures below 1150°C (1050°C, 1100°C, 1125°C, 1138°C), the M50 steel exhibited typical ductile fracture characteristics. After reaching 1150°C, a transition from ductile fracture to intergranular fracture was observed, attributed to the reduction in ductility.
5. A detailed analysis of the fracture morphology indicates that 1150°C can be regarded as the equi-cohesive temperature for M50. This finding aligns with the simulation results, which determined that an  $LC_n$  damage criterion of “2” is suitable for temperatures up to 1150°C, while a criterion of “1” is applicable for temperatures exceeding this threshold.
6. The shearing stage of hot forging processes, where a precise and smooth cut surface is crucial, was also studied in detail in this thesis. The shearing length was initially determined using the temperature-dependent  $LC_n$  damage criterion in forging simulations, which were conducted at four different starting temperatures (1100°C, 1150°C, 1175°C, and 1200°C) and with four varying die clearances (0.1 mm, 0.2 mm, 0.4 mm, and 0.8 mm). The simulation results revealed similar trends in cutting lengths across different clearances and forging temperatures, with no increase in shearing length achieved.
7. To verify the simulation results experimentally, hot forging trials were carried out at temperatures of 1100°C, 1150°C, and 1200°C using a 0.4 mm die clearance, and an analysis of shearing length was conducted. The results from the experimental forging processes were found to be consistent with the simulation outcomes.
8. The simulations were initially performed using the hot forging press set at its original speed of 80 rpm to determine if the shearing process tool's

advancement speed affects shearing length. Following this, additional simulations were conducted at lower (30 rpm) and higher (100 rpm) speeds, using the 1150°C condition as a reference. The shearing lengths from these simulations were compared, but no significant effects of the different speeds on the shearing length were observed.

9. To investigate the effect of die geometry on shearing length, radii and conical shapes at various angles were incorporated into the tool edges that come into contact with the die corners for simulation. Simulation studies of the shearing stage showed similar trends in cutting lengths, revealing that the conically shaped upper die did not result in an increase in shearing length.





## REFERENCES

- [1] Bhadeshia, H.K.D.H. (2012). Steels for bearings. *Progress in Materials Science*, 57(2), 268–435
- [2] Kvryan, Armen & Faulkner, Emma & Lysne, Drew & Carter, Nicholas & Acharya, Sanjeev & Rafla, Veronica & Trivedi, Hitesh & Hurley, Michael. (2017). Electrochemical Corrosion Test Methods for Rapid Assessment of Aerospace Bearing Steel Performance. 10.1520/STP160020160150.
- [3] Parker, R. J., & Zaretsky, E. V. (1972). Rolling-Element fatigue lives of Through-Hardened bearing materials. *Journal of Lubrication Technology*, 94(2), 165–171. <https://doi.org/10.1115/1.3451669>
- [4] Allison, B.D. (2013). Evolution of mechanical properties of M50 bearing steel due to rolling contact fatigue.
- [5] Ooi, S., & Bhadeshia, H. (2012). Duplex Hardening of Steels for Aeroengine Bearings. *Isij International*, 52, 1927-1934.
- [6] Hetzner, D.W.; Van Geertruyden, W. Crystallography and metallography of carbides in high alloy steels. *Mater. Charact.* 2008, 59, 825–841.
- [7] Hetzner, D.W. Refining carbide size distributions in M1 high speed steel by processing and alloying. *Mater. Charact.* 2001, 46, 175–182.
- [8] Forster, N. H., Peters, S. M., Chin, H., Poplawski, J. V., & Homan, R. (2017). Applying finite element analysis to determine the subsurface stress and temperature gradient in highly loaded bearing contacts. In *ASTM International eBooks* (pp.151-166).
- [9] Mukhopadhyay, P., Kannaki, P., Srinivas, M., & Roy, M. (2014). Microstructural developments during abrasion of M50 bearing steel. *Wear*, 315(1–2), 31–37. <https://doi.org/10.1016/j.wear.2014.03.010>
- [10] De Micheli, P., Settefrati, A., Marie, S., Barlier, J., Lasne, P., Scholtes, B., Bernacki, M., & Bay, F. (2015, May 4). *Towards the simulation of the whole manufacturing chain processes with FORGE®*. <https://minesparis-psl.hal.science/hal-01247710>

- [11] Jiang, H., Wu, Y., Gong, X., Shan, D., & Zong, Y. (2019). Control of flow lines during the forging process of bearing outer rings with a deviated groove. *The International Journal of Advanced Manufacturing Technology*, 106(1–2), 753–764. <https://doi.org/10.1007/s00170-019-04465-9>
- [12] Afazov, S. (2013). Modelling and simulation of manufacturing process chains. *CIRP Journal of Manufacturing Science and Technology*, 6(1), 70–77. <https://doi.org/10.1016/j.cirpj.2012.10.005>
- [13] Heusinger, S., Rosso, R., Klemm, P., Newman, S. T., & Rahimifard, S. (2006). Integrating the CAx process chain for STEP-compliant NC manufacturing of asymmetric parts. *International Journal of Computer Integrated Manufacturing*, 19(6), 533-545. <https://doi.org/10.1080/09511920600622098>
- [14] Monostori, L., & Viharos, Z. J. (2001). Hybrid, AI- and simulation-supported optimisation of process chains and production plants. *CIRP Annals*, 50(1), 353–356. [https://doi.org/10.1016/s0007-8506\(07\)62138-6](https://doi.org/10.1016/s0007-8506(07)62138-6)
- [15] Hyun, S., & Lindgren, L. (2004). Simulating a chain of manufacturing processes using a geometry-based finite element code with adaptive meshing. *Finite Elements in Analysis and Design*, 40(5–6), 511–528. [https://doi.org/10.1016/s0168-874x\(03\)00075-1](https://doi.org/10.1016/s0168-874x(03)00075-1)
- [16] Pietrzyk, M., Madej, Ł., & Węglarczyk, S. (2008). Tool for optimal design of manufacturing chain based on metal forming. *CIRP Annals*, 57(1), 309–312. <https://doi.org/10.1016/j.cirp.2008.03.099>
- [17] Klein, M., & Eifler, D. (2010). Influences of the manufacturing process chain design on the near surface condition and the resulting fatigue behaviour of quenched and tempered SAE 4140. *Journal of Physics: Conference Series*, 240, 012052. <https://doi.org/10.1088/1742-6596/240/1/012052>
- [18] Åström, P. (2004). Simulation of manufacturing processes in product development. The Polhem Laboratory, Division of Computer Aided Design,

Department of Applied Physics and Mechanical Engineering, Luleå University of Technology.

- [19] Maekawa, K., Shirakashi, T., & Obikawa, T. (1996b). Recent progress of computer aided simulation of chip flow and tool damage in metal machining. *Proceedings of the Institution of Mechanical Engineers, Part B: Journal of Engineering Manufacture*, 210(3), 233–242. [https://doi.org/10.1243/pime\\_proc\\_1996\\_210\\_112\\_02](https://doi.org/10.1243/pime_proc_1996_210_112_02)
- [20] Johansson, H., Åström, P., & Orsborn, K. (2004). A system for information management in simulation of manufacturing processes. *Advances in Engineering Software*, 35(10–11), 725–733. <https://doi.org/10.1016/j.advengsoft.2004.03.019>
- [21] Özgeneci, Z. (2017). The Effect Of Retained Austenite and Carbide Distribution on the Wear Resistance of Bearing Steel, *Master of Science in Metallurgical and Materials Engineering Department*, Middle East Technical University
- [22] G. E. Dieter, H. A. Kuhn and S. L. Semiatin, “Handbook of Workability and Process Design,” American Society for Metals, Materials Park, 2003, pp. 27-29, pp. 54-60, pp. 291-321.
- [23] Lin, Y., Chen, M., & Zhong, J. (2008). Constitutive modeling for elevated temperature flow behavior of 42CrMo steel. *Computational Materials Science*, 42(3), 470–477. <https://doi.org/10.1016/j.commatsci.2007.08.011>
- [24] Lin, Y., Chen, M., & Zhong, J. (2008b). Effect of temperature and strain rate on the compressive deformation behavior of 42CrMo steel. *Journal of Materials Processing Technology*, 205(1–3), 308–315. <https://doi.org/10.1016/j.jmatprotec.2007.11.113>
- [25] Lin, Y., Li, K., Li, H., Chen, J., Chen, X., & Wen, D. (2015). New constitutive model for high-temperature deformation behavior of inconel 718 superalloy. *Materials in Engineering*, 74, 108–118. <https://doi.org/10.1016/j.matdes.2015.03.001>

- [26] Rao, K., & Hawbolt, E. B. (1992). Development of constitutive relationships using compression testing of a medium carbon steel. *Journal of Engineering Materials and Technology-transactions of the Asme*, 114(1), 116–123. <https://doi.org/10.1115/1.2904131>
- [27] Lin, Y., & Chen, X. (2011). A critical review of experimental results and constitutive descriptions for metals and alloys in hot working. *Materials in Engineering*, 32(4), 1733–1759. <https://doi.org/10.1016/j.matdes.2010.11.048>
- [28] Ben, N., Zhang, D., Liu, N., Zhao, X., Guo, Z., Zhang, Q., & Zhao, S. (2017). FE modeling of warm flanging process of large T-pipe from thick-wall cylinder. *The International Journal of Advanced Manufacturing Technology*, 93(9–12), 3189–3201. <https://doi.org/10.1007/s00170-017-0739-6>
- [29] Johnson, G.R. and Cook, W.H. (1983) A Constitutive Model and Data for Metals Subjected to Large Strains, High Strain Rates, and High Temperatures. *Proceedings 7th International Symposium on Ballistics*, The Hague, 19-21 April 1983, 541-547.
- [30] Khan, A. S., & Huang, S. (1992). Experimental and theoretical study of mechanical behavior of 1100 aluminum in the strain rate range  $10^{-5}$ – $10^4$ s $^{-1}$ . *International Journal of Plasticity*, 8(4), 397–424. [https://doi.org/10.1016/0749-6419\(92\)90057-j](https://doi.org/10.1016/0749-6419(92)90057-j)
- [31] Khan, A. S., Zhang, H., & Takács, L. (2000). Mechanical response and modeling of fully compacted nanocrystalline iron and copper. *International Journal of Plasticity*, 16(12), 1459–1476. [https://doi.org/10.1016/s0749-6419\(00\)00023-1](https://doi.org/10.1016/s0749-6419(00)00023-1)
- [32] Khan, A. S., Suh, Y. H., & Kazmi, R. (2004). Quasi-static and dynamic loading responses and constitutive modeling of titanium alloys. *International Journal of Plasticity*, 20(12), 2233–2248. <https://doi.org/10.1016/j.ijplas.2003.06.005>

- [33] Khan, A. S., Suh, Y. H., Chen, X., Takács, L., & Zhang, H. (2006). Nanocrystalline aluminum and iron: Mechanical behavior at quasi-static and high strain rates, and constitutive modeling. *International Journal of Plasticity*, 22(2), 195–209. <https://doi.org/10.1016/j.ijplas.2004.07.008>
- [34] Farrokh, B., & Khan, A. S. (2009). Grain size, strain rate, and temperature dependence of flow stress in ultra-fine grained and nanocrystalline Cu and Al: Synthesis, experiment, and constitutive modeling. *International Journal of Plasticity*, 25(5), 715–732. <https://doi.org/10.1016/j.ijplas.2008.08.001>
- [35] Fields, D.S. and Backofen, W.A. (1957) Determination of Strain Hardening Characteristics by Torsion Testing. *Proceeding of American Society for Testing and Materials*, 57, 1259-1272.
- [36] Molinari, A., & Ravichandran, G. (2005). Constitutive modeling of high-strain-rate deformation in metals based on the evolution of an effective microstructural length. *Mechanics of Materials*, 37(7), 737–752. <https://doi.org/10.1016/j.mechmat.2004.07.005>
- [37] Voce, E. (1948) The Relationship Between Stress and Strain for Homogeneous Deformation. *Journal of the Institute of Metals*, 74, 537-562.
- [38] Kocks, U.F. (1976) Laws for Work-Hardening and Low-Temperature Creep. *ASME Journal of Engineering Materials and Technology*, 98, 76-85. <http://dx.doi.org/10.1115/1.3443340>
- [39] Zener, C., & Hollomon, J. H. (1944). Effect of strain rate upon plastic flow of steel. *Journal of Applied Physics*, 15(1), 22–32. <https://doi.org/10.1063/1.1707363>
- [40] Sellars, C., & McTegart, W.J. (1966). On the mechanism of hot deformation. *Acta Metallurgica*, 14, 1136-1138.
- [41] Jonas, J. J., Sellars, C. M., & Tegart, W. J. M. (1969). Strength and structure under hot-working conditions. *Metallurgical Reviews*, 14(1), 1–24. <https://doi.org/10.1179/mtlr.1969.14.1.1>
- [42] Shi, H., McLaren, A. J., Sellars, C. M., Shahani, R., & Bolingbroke, R. (1997). Constitutive equations for high temperature flow stress of aluminium

- alloys. *Materials Science and Technology*, 13(3), 210–216. <https://doi.org/10.1179/mst.1997.13.3.210>
- [43] Lin, Y., & Ge, L. (2010). A new mathematical model for predicting flow stress of typical high-strength alloy steel at elevated high temperature. *Computational Materials Science*, 48(1), 54–58. <https://doi.org/10.1016/j.commatsci.2009.06.026>
- [44] Hänsel A, Spittel T (1978) Kraft- und Arbeitsbedarf bildsamer Formgebungsverfahren. Deutscher Verlag für Grundstoffindustrie, VEB, Leipzig
- [45] Chadha, K., Shahriari, D., & Jahazi, M. (2017). An Approach to Develop Hansel–Spittel Constitutive Equation during Ingot Breakdown Operation of Low Alloy Steels. In *Springer eBooks* (pp. 239–246). [https://doi.org/10.1007/978-981-10-4819-7\\_20](https://doi.org/10.1007/978-981-10-4819-7_20)
- [46] Mehtedi, M. E., Musharavati, F., & Spigarelli, S. (2014). Modelling of the flow behaviour of wrought aluminium alloys at elevated temperatures by a new constitutive equation. *Materials in Engineering*, 54, 869–873. <https://doi.org/10.1016/j.matdes.2013.09.013>
- [47] Rudnytskyj, A., Šimon, P., Jech, M., & Gachot, C. (2020). Constitutive modelling of the 6061 aluminium alloy under hot rolling conditions and large strain ranges. *Materials & Design*, 190, 108568. <https://doi.org/10.1016/j.matdes.2020.108568>
- [48] Wei, G., Peng, X., Hadadzadeh, A., Mahmoodkhani, Y., Xie, W., Yang, Y., & Wells, M. A. (2015). Constitutive modeling of Mg–9Li–3Al–2Sr–2Y at elevated temperatures. *Mechanics of Materials*, 89, 241–253. <https://doi.org/10.1016/j.mechmat.2015.05.006>
- [49] Godor, F., Werner, R., Lindemann, J., Clemens, H., & Mayer, S. (2015). Characterization of the high temperature deformation behavior of two intermetallic TiAl–Mo alloys. *Materials Science and Engineering: A*, 648, 208–216. <https://doi.org/10.1016/j.msea.2015.09.077>

- [50] Rebeyka, C. J., Button, S. T., Lajarin, S. F., & Marcondes, P. V. P. (2018). Mechanical behavior of HSLA350/440 and DP350/600 steels at different temperatures and strain rates. *Materials Research Express*, 5(6), 066515. <https://doi.org/10.1088/2053-1591/aac874>
- [51] Lin, Y., Wu, Q., Pang, G., Jiang, X., & He, D. (2019). Hot Tensile Deformation Mechanism and Dynamic Softening Behavior of Ti–6Al–4V Alloy with Thick Lamellar Microstructures. *Advanced Engineering Materials*, 22(3). <https://doi.org/10.1002/adem.201901193>
- [52] Wang, H., Wang, W., Zhai, R., Ma, R., Zhao, J., & Mu, Z. (2020). Constitutive equations for describing the warm and hot deformation behavior of 20CR2NI4A alloy steel. *Metals*, 10(9), 1169. <https://doi.org/10.3390/met10091169>
- [53] Qiang, L., Liu, X., Li, P., Ding, P., & Zhang, X. (2020). Development and application of High-Temperature Constitutive Model of HNI55-7-4-2 Alloy. *Metals*, 10(9), 1250. <https://doi.org/10.3390/met10091250>
- [54] Gaikwad, A., Kirwai, S., Koley, P., Balachandran, G., & Singh, R. K. (2016). Theoretical study on Cold Open Die Forging Process Optimization for Multipass Workability. *MATEC Web of Conferences*, 80, 13002. <https://doi.org/10.1051/mateconf/20168013002>
- [55] Hering, O., & Tekkaya, A. E. (2020). Damage-induced performance variations of cold forged parts. *Journal of Materials Processing Technology*, 279, 116556. <https://doi.org/10.1016/j.jmatprotec.2019.116556>
- [56] Soyarslan, C., Tekkaya, A. E., & Akyüz, U. (2008). Application of Continuum Damage Mechanics in discontinuous crack formation: Forward extrusion chevron predictions. *ZAMM - Journal of Applied Mathematics and Mechanics*, 88(6), 436–453. <https://doi.org/10.1002/zamm.200800013>
- [57] Reusch, F. (2003). Entwicklung und Anwendung eines nicht-lokalen Materialmodells zur Simulation duktiler Schädigung in metallischen Werkstoffen. doi:10.17877/DE290R-16074



- [58] Ôyane, M. (1972). Criteria of ductile fracture strain. *Bulletin of the JSME*, 15(90), 1507–1513. <https://doi.org/10.1299/jsme1958.15.1507>
- [59] Freudenthal, A.M. (1950) *The Inelastic Behavior of Engineering Materials and Structures*. John Wiley & Sons, New York
- [60] M. G. Cockcroft and D. J. Latham, “Ductility and the Workability of Metals,” *Journal Institute of Metals*, Vol. 96, 1968, pp. 33-39
- [61] B. Rozzo, P., Deluca, B. and Rendina, R., 1972, A new method for the prediction of formability limits in metal sheets, *Sheet Metal Forming and Formability: Proceedings of the 7th biennial Conference of the International Deep Drawing Research group*
- [62] Vafaenezhad, H., Seyedein, S., Aboutalebi, & Eivani, A. (2020). Using high temperature tensile testing data to analyze hot formability of Sn-5Sb alloy: instability and critical damage criteria. *Journal of Materials Research and Technology*, 9(3), 4159–4172. <https://doi.org/10.1016/j.jmrt.2020.02.043>
- [63] Schowtjak, A., Clausmeyer, T., & Tekkaya, A.E. (2017). Analysis of damage and fracture formulations in cold extrusion. *IV International Conference on Computational Plasticity, Fundamentals and Applications*
- [64] Yoshino, M., & Shirakashi, T. (1997). Flow-stress equation including effects of strain-rate and temperature history. *International Journal of Mechanical Sciences*, 39(12), 1345–1362. [https://doi.org/10.1016/s0020-7403\(97\)00020-9](https://doi.org/10.1016/s0020-7403(97)00020-9)
- [65] Hill, R. (1998a). *The Mathematical Theory of plasticity*. Oxford University Press.
- [66] Kuhn, H. A. (2009). Models for Fracture during Deformation Processing. In *ASM International eBooks* (pp. 346–361). <https://doi.org/10.31399/asm.hb.v22a.a0005461>
- [67] Gouveia, B., Rodrigues, J., & Martins, P. (2000). Ductile fracture in metalworking: experimental and theoretical research. *Journal of Materials Processing Technology*, 101(1–3), 52–63. [https://doi.org/10.1016/s0924-0136\(99\)00449-5](https://doi.org/10.1016/s0924-0136(99)00449-5)

- [68] Oh, S., Walters, J., & Wu, W. (2005). Finite element method applications in bulk forming. In *ASM International eBooks* (pp. 617–639). <https://doi.org/10.31399/asm.hb.v14a.a0004021>
- [69] Gontarz, A. and Piesiak, J. (2015) Determining the Normalized Cockcroft-Latham Criterion for Ti6Al4V in Tensile Testing at Room Temperature. *Proceedings of the World Congress on Mechanical, Chemical, and Material Engineering*, Barcelona, 20-21 July 2015, Paper No. 248.
- [70] Chen, C. C., Oh, S., & Kobayashi, S. (1979). Ductile Fracture in Axisymmetric Extrusion and Drawing—Part 1: Deformation Mechanics of Extrusion and Drawing. *Journal of Engineering for Industry*, 101(1), 36–44. <https://doi.org/10.1115/1.3439470>
- [71] Stebunov, S., Vlasov, A. B., & Biba, N. (2018). Prediction of fracture in cold forging with modified Cockcroft-Latham criterion. *Procedia Manufacturing*, 15, 519–526. <https://doi.org/10.1016/j.promfg.2018.07.264>
- [72] Lin, Y., Liu, Y., Ge, L., Chen, M., & Huang, Y. (2014). Prediction of ductile fracture behaviors for 42CRMo steel at elevated temperatures. *Journal of Materials Engineering and Performance*, 24(1), 221–228. <https://doi.org/10.1007/s11665-014-1273-4>
- [73] Gleeble User's Manual (2013), Dynamic Systems Inc.
- [74] ASTM E209-00-Standard Practice for Compression Tests of Metallic Materials at Elevated Temperatures with Conventional or Rapid Heating Rates and Strain Rates
- [75] Y.V.R.K. Prasad, K.P. Rao, S. Sasidhara, Hot Working Guide: A Compendium of Processing Maps, Second Edition, 2015, ASM International, ISBN: 978-1-62708-091-0, page 4
- [76] Measurement Good Practice Guide No:3, Measuring Flow Stress in Hot Axisymmetric Compression Tests, National Physics Laboratory, 2002, pp. 28–32, 38
- [77] Jedrasiak, P., Shercliff, H., Mishra, S., Daniel, C. S., & Da Fonseca, J. Q. (2022). Finite element modeling of hot compression testing of titanium

- alloys. *Journal of Materials Engineering and Performance*, 31(9), 7160–7175. <https://doi.org/10.1007/s11665-022-06750-3>
- [78] Wang, X., Li, H., Chandrashekhara, K., Rummel, S. A., Lekakh, S. N., Van Aken, D. C., & O'Malley, R. J. (2017). Inverse finite element modeling of the barreling effect on experimental stress-strain curve for high temperature steel compression test. *Journal of Materials Processing Technology*, 243, 465–473. <https://doi.org/10.1016/j.jmatprotec.2017.01.012>
- [79] Dieter GE (1989) Mechanical metallurgy. SI Metric Edition, McGraw-Hill, pp 539-541
- [80] Evans RW, Scharning PJ (2002) Axisymmetric compression test and hot working properties of alloys. *Materials Science and Technology*, 18, pp 1389-1399
- [81] Transvalor Forge (2011) User Manual: Transvalor Forming Solutions Documentation, Part 5: Process Data
- [82] Chen D, Chang D, Chen F, Kuo T (2018) Application of ductile fracture criterion for tensile test of zirconium alloy 702. *Scientia Iranica* 25(2), pp 824-829. doi:[10.24200/sci.2018.20174](https://doi.org/10.24200/sci.2018.20174)
- [83] M.B. Toloczko, M.L. Hamilton, G.E. Lucas, (2000) Ductility correlations between shear punch and uniaxial tensile test data, *Journal of Nuclear Materials*, Volumes 283–287, Part 2, Pages: 987–991. [https://doi.org/10.1016/S0022-3115\(00\)00198-7](https://doi.org/10.1016/S0022-3115(00)00198-7)
- [84] G.L. Hankin, M.B. Toloczko, M.L. Hamilton, R.G. Faulkner, *J. Nucl. Mater.* 258–263 (1998) 1651–1656
- [85] M.B. Toloczko, R.J. Kurtz, A. Hasegawa, K. Abe, *J. Nucl. Mater.* 307–311 (2002) 1619–1623
- [86] M.L. Hamilton, M.B. Toloczko, *J. Nucl. Mater.* 283–287 (2000) 488–491.
- [87] Guduru RK, Darling KA, Kishore R, Scattergood RO, Koch CC, Murty KL (2005) Evaluation of mechanical properties using shear-punch testing, *Materials Science and Engineering: A*, volume 395, issues 1–2, pp 307-314, ISSN 0921-5093. <https://doi.org/10.1016/j.msea.2004.12.048>

- [88] Dennis W. Hetzner, William Van Geertruyden, Crystallography and metallography of carbides in high alloy steels, *Materials Characterization*, Volume 59, Issue 7, 2008, Pages 825-841, ISSN 1044-5803, <https://doi.org/10.1016/j.matchar.2007.07.005>
- [89] J. E. Bridge, G. N. Maniar, and T. V. Philip. Carbides in M50 high-speed steel. *Metallurgical Transactions*, 2:2209–2214, 1971
- [90] Ziheng Shao, Yankun Zhu, Peng Zhang, Yanfei Cao, Bin Wang, Zikuan Xu, Hanzhong Liu, Xuezhong Gu, Hongwei Liu, Dianzhong Li, Zhefeng Zhang, Effect of primary carbides on rolling contact fatigue behaviors of M50 bearing steel, *International Journal of Fatigue*, Volume 179, 2024, 108054, ISSN 0142-1123, <https://doi.org/10.1016/j.ijfatigue.2023.108054>.
- [91] Ningyu Du, Hanghang Liu, Yanfei Cao, Paixian Fu, Chen Sun, Hongwei Liu, Dianzhong Li, Formation mechanism of MC and M<sub>2</sub>C primary carbides in as-cast M50 bearing steel, *Materials Characterization*, Volume 174, 2021, 111011, ISSN 1044-5803, <https://doi.org/10.1016/j.matchar.2021.111011>.
- [92] Pearson, P. K., Dickinson, T. W., The role of carbides in Performance of high-alloy bearing steels, *Effect of Steel Manufacturing Processes on the Quality of Bearing Steels*, ASTM STP 987, J. J. C. Hoo, Ed., American Society for Testing and Materials, Philadelphia, 1988, pp. 113-131
- [93] Campbell J. Incipient grain boundary melting. *Materials Science and Technology*. 2009;25(1):125-126. doi:[10.1179/174328408X311080](https://doi.org/10.1179/174328408X311080)
- [94] Shewmon, Paul G., Grain boundary cracking, *Metallurgical and Materials Transactions: Process Metallurgy and Materials Processing Science, B*; New York Vol. 29B, Iss. 3, (Jun 1998): 509
- [95] G. D. Bengough, *J. Inst. Metals* 7 (1912) 123-174.
- [96] M. Xu, W. Yang, J. Liang, Y. Meng, L. Zheng, Experimental Study on the Correlation between Intermediate Temperature Embrittlement and Equi-Cohesive Temperature, 2014, doi: <http://dx.doi.org/10.1016/j.jallcom.2014.05.037> ]

- [97] Z.C. Peng, J.W. Zou, Y. Wang, L. Zhou, Y. Tang, Effects of solution temperatures on creep resistance in a powder metallurgy nickel-based superalloy, *Mater. Today Commun.* 28 (2021) 102573, <https://doi.org/10.1016/j.mtcomm.2021.102573>.
- [98] X.F. Yu, D.Y. Zheng, X.F. Yang, S.Y. Wang, M. An, G.B. Yan, Y.Z. Xia, F. Xing, Effect of carbide precipitation behavior at high temperatures on microstructure and mechanical properties of M50 steel, *Journal of Materials Research and Technology*, Volume 18, 2022, Pages 1155-1165, ISSN 2238-7854, <https://doi.org/10.1016/j.jmrt.2022.03.021>.
- [99] S.M.C. van Bohemen, H.K.D.H. Bhadeshia, *Ductile Fracture*, 2008; Available from: <https://www.phase-trans.msm.cam.ac.uk/2008/weld/weld.html#:~:text=When%20a%20ductile-fracture%20surface,the%20depth%20of%20the%20dimple>.
- [100] Xue Yang, Zhimin Zhang, Mu Meng, Jingjing Jia, Honglei Zhang, Genxing Lei, Jianmin Yu, Hot tensile deformation behaviors and a fracture damage model of the Mg-Gd-Y-Zn-Zr alloy, *Journal of Materials Research and Technology*, Volume 18, 2022, Pages 255-267, ISSN 2238-7854, <https://doi.org/10.1016/j.jmrt.2022.02.104>.
- [101] Li B, Teng B, Wang E. Effects of accumulative rolling reduction on the microstructure characteristic and mechanical properties of Mg-Gd-Y-Zn-Zr sheets processed by hot rolling. *Mater Sci Eng* 2019;765. <https://doi.org/10.1016/j.msea.2019.138317>.
- [102] Chen, G.; Lu, X.; Yan, J.; Liu, H.; Sang, B. High-Temperature Deformation Behavior of M50 Steel. *Metals* 2022, 12,541. <https://doi.org/10.3390/met12040541>
- [103] ASTM Designation: E112 – 13 (Reapproved 2021) Standard Test Methods for Determining Average Grain Size

- [104] P. Mason and P. Prev y, "Iterative Taguchi Analysis: Optimizing the Austenite Content and Hardness In 52100 Steel," *Journal of Materials Engineering and Performance*, vol. 10, no. 1, pp. 14-21, 2001
- [105] ASTM E975-13, Standard Practice for X-Ray Determination of Retained Austenite in Steel with Near Random Crystallographic Orientation, West Conshohocken, PA: ASTM International, 2013
- [106] Fei Gao, Zilong Gao, Qiyong Zhu, Fuxiao Yu, Zhenyu Liu, Deformation behavior of retained austenite and its effect on plasticity based on in-situ EBSD analysis for transformable ferritic stainless steel, *Journal of Materials Research and Technology*, Volume 20, 2022, Pages 1976-1992, ISSN 2238-7854. <https://doi.org/10.1016/j.jmrt.2022.07.160>.
- [107] Pinto, L.A. & Perez Escobar, Diana & Santos, Olivia & Lopes, Natalia & Carneiro, J.R.G. & de Andrade, Rodrigo. (2020). Influence of surface preparation method on retained austenite quantification. *Materials Today Communications*. 24. 101226. [10.1016/j.mtcomm.2020.101226](https://doi.org/10.1016/j.mtcomm.2020.101226).
- [108] Arbak M, Tekkaya AE,  zhan F (2005) Comparison of various preforms for hot forging of bearing rings. *Journal of Materials Processing Technology*, volume 169, issue 1, pp:72-82, <https://doi.org/10.1016/j.jmatprotec.2004.11.020>
- [109] Allen, P, Wilson, C. Hydrostatic Stress Effect on the Yield Behavior of Inconel 100. *Journal of the Mechanical Behavior of Materials*. 2004;15(1-2): 27-48. <https://doi.org/10.1515/JMBM.2004.15.1-2.27>
- [110] P. W. Bridgman; The Effect of Hydrostatic Pressure on the Fracture of Brittle Substances. *J. Appl. Phys.* 1 February 1947; 18 (2): 246–258. <https://doi.org/10.1063/1.1697610>
- [111] O. Richmond, W.A. Spitzig, Pressure Dependence and Dilatancy of Plastic Flow, *International Union of Theoretical and Applied Mechanics Conference Proceedings*, pages 377–386, 1980



## CURRICULUM VITAE

Surname, Name: Özgeneci, Zeren

### EDUCATION

<b>Degree</b>	<b>Institution</b>	<b>Year of Graduation</b>
MS	METU Metallurgical and Materials Engineering	2017
BS	ESOGU Metallurgical and Materials Engineering	2011
High School	Ankara Anadolu High School, Ankara	2006

### FOREIGN LANGUAGES

Advanced English, Basic French

### PUBLICATIONS

1. Ozgeneci Z., Music O., Simsir C., "Finite element analysis of damage in hot forging of bearing rings", The International Journal of Advanced Manufacturing Technology, January 2025
2. Ozgeneci, Z., Ogel, B., "The effect of retained austenite and carbide distribution on the wear resistance of the bearing raceway", International Bearing Conference, Kaiserslautern, Germany, March 2018

### HOBBIES

Sports (fitness, pilates, cardio), Traveling, Fashion